ISSN 1349-1113
JAXA-RR-04-027E

JAXA Research and Development Report

Marangoni Convection Modeling Research, 2003 – 2004

March 2005

Japan Aerospace Exploration Agency

CONTENTS

OVERVIEW

Shinichi Yoda

NASDA has so far conducted many microgravity experiments by means of sounding rockets and Space shuttle. After the microgravity experiment planning processes for those experiments, we concluded that in order to fully utilize the microgravity environment of space we need to have a better knowledge base on subjects such as thermophysical properties of the samples, fluid behaviors in the experiments, and so on. Needless to say, fluid physics should play a central role in microgravity science, since microgravity affects mainly the state of fluid and vapor. To obtain accurate information from an experiment, we should know various thermophysical properties such as temperature dependence of viscosity, surface tension, density, and so on, determined by the specific experiment purposes. We also should know about related material science such as crystal growth and so on, if the experiment deals with material processing under microgravity. In order to optimize the experimental parameters to accomplish its experiment objectives, we must develop experimental technology such as design of specimen container, measurement of temperature, etc. A successful microgravity experiment requires much prior knowledge, as mentioned above, therefore we should accumulate sufficient knowledge base to accomplish the experiment objectives, which can be done by the so-called team research method consisting of many knowledgeable researchers.

For that reason the Space Utilization Research Program (SURP) was established in order to do team research in collaboration with researchers from outside NASDA. The role of SURP in microgravity science is defined to perform systematic research for demonstrating the potential of microgravity utilization by producing SHOWCASE and to promote microgravity utilization as the frontier in Microgravity Science Research.

Much effort has been made to try to understand the effectiveness of microgravity utilization so far, but only limited systematic results have been derived from microgravity experiments. NASDA has sought appropriate microgravity research themes related to the above and selected the following subjects; thermocapillary flow in fluid physics, high quality semiconductor production in materials science, and diffusion behavior modeling in fundamental physics. The present report is written for the thermocapillary flow project.

Convective motion induced by local variations of surface tension along a liquid free surface is called Marangoni convection. Although such variations can be caused by differences in temperature or composition, our main interest here is temperature-induced convection, often called thermocapillary convection. In a terrestrial environment, Marangoni convection is usually overshadowed by buoyancy-driven flow. In the reduced gravity environment of space, however, buoyancy is greatly reduced and Marangoni convection could become very important. In such applications as crystal growth from melts and two-phase flow with heat transfer, Marangoni flow is known to play an important role. For that reason much attention has been given in recent years to Marangoni convection. Since the floating-zone crystal growth process is considered to be a promising method of obtaining high quality crystals in microgravity, Marangoni convection in floating-zone melts is an important subject.

Much work has been done on Marangoni convection in the past, both experimentally and theoretically. Most of the experimental investigations were conducted in normal gravity but some results from microgravity experiments are now available, as summarized in Table 1. High Prandtl number (Pr) fluids have been used in most experiments. Although Pr of crystal melts is generally smaller than unity, much less experimental information is available for low Pr fluids due to some experimental difficulties. The transport phenomena in the floating-zone melt have been simulated by many investigators in the so-called liquid bridge configuration, in which a liquid column is suspended vertically between two differentially heated rods.

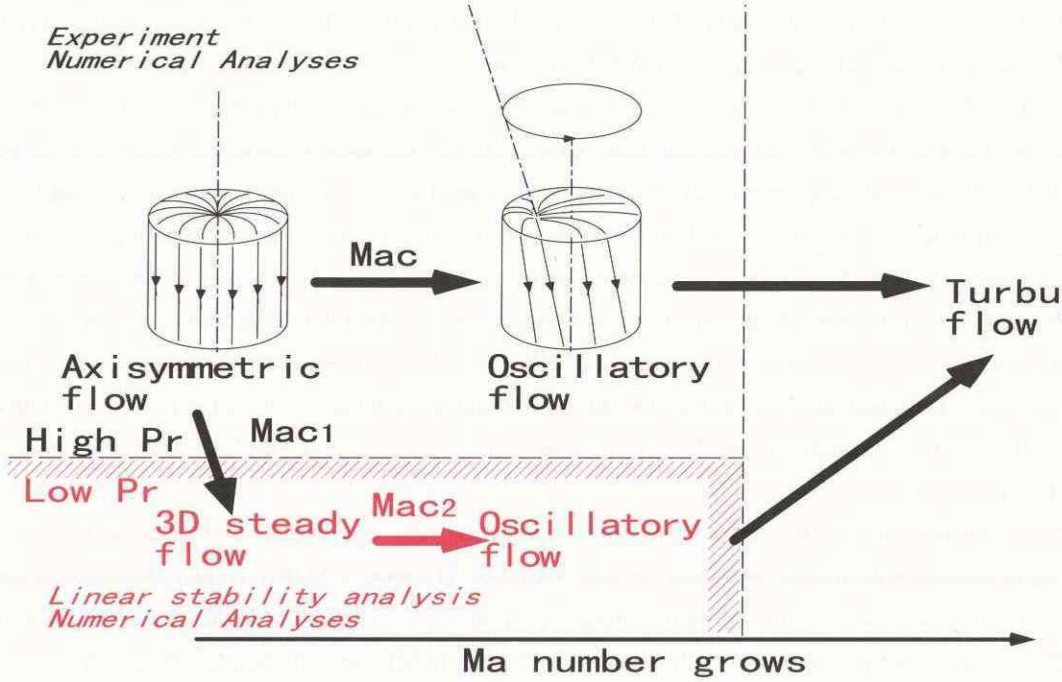

Figure 1. Transition Phenomena of Thermocapillary Flow

One important feature of Marangoni convection in the liquid bridge configuration is a transition from steady to oscillatory flow, as illustrated in Figure 1. Since oscillations have significant implications to crystal growth, it is important to understand how and when the transition occurs. Despite the fact that much research has been conducted on the oscillation phenomenon in the past twenty years, the cause of oscillations is not yet fully understood. For example, recent experiments under microgravity conditions showed that the Marangoni number corresponding to the onset of oscillations is dependent on the size of the liquid bridge as seen in Figure 2, suggesting that the Marangoni number alone cannot determine the conditions of the transition. The subject is obviously very complex and requires extensive experimental, numerical, and theoretical efforts to solve it. That is the main motivation behind the present Marangoni Convection Modeling Research. The major objectives of the project are: (1) to investigate oscillatory Marangoni convection in the liquid bridge configuration experimentally, numerically, as well as theoretically, and (2) to determine the cause of oscillations and construct a physical model to delineate it.

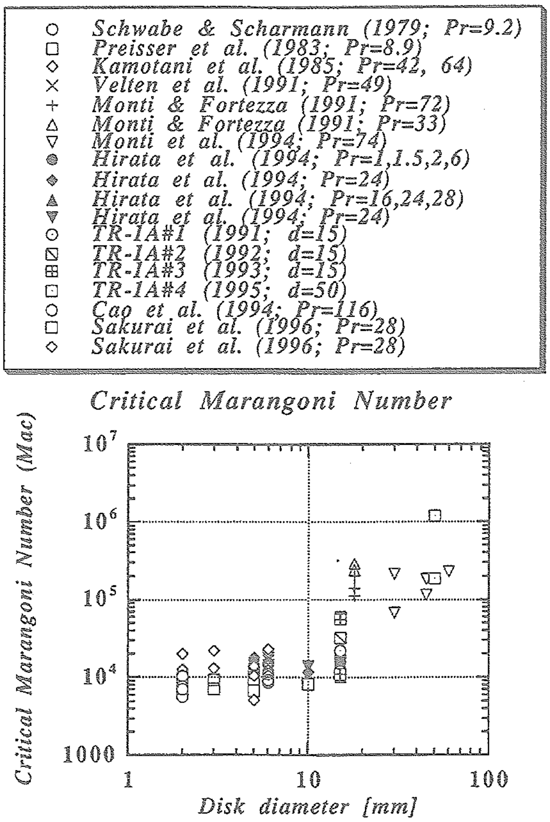

Figure 2. Dependence of Critical Marangoni Number on the size of the liquid bridge

The present project deals with low, medium, and high Prandtl number fluids. Each Pr range has unique features. In the high Pr range (Pr larger than about 10), although many experimental data can be found in literature, no accurate stability analyses nor numerical simulations of the oscillation phenomenon are currently available. One important aspect is that dynamic free surface deformation, albeit small, may play an important role in the oscillation mechanism. Therefore, more experiments and analyses are necessary to understand the oscillation phenomenon in this Pr range. The phase relationship between the dynamic free surface deformation and surface temperature oscillations in the hot corner has been successfully determined by the simultaneous measurements of both in this year, so our understanding of a role of dynamic free surface deformation in the oscillation mechanism has increased appreciably. Some important features of oscillatory flows are also being investigated experimentally and numerically. In the low Pr range (Pr less than about 0.1), the flow is known to become at first three-dimensional due to a hydrodynamic instability and then becomes oscillatory (see Figure 1), according to theoretical and numerical analyses. The result needs to be proven experimentally. We have successfully overcome a difficult problem of oxidation at the free surface of low Pr fluid, molten tin, thus enabling us to obtain reliable experimental data. The experimental apparatus has unique features for obtaining and sustaining a clean free surface of the fluid and for detecting surface temperature oscillations. Numerical simulations of oscillations in low Pr fluid have given us important information and the predictions will be compared with the experimental results. In the medium Pr range (Pr about unity), it is known theoretically that the flow becomes oscillatory, which needs to be confirmed experimentally. We have been able to reduce evaporation from the free surface of medium Pr fluids near room temperature, but its effect is still important.

However, meaningful results have been obtained concerning oscillatory thermocapillary flow in conjunction with linear stability analysis of medium Pr fluid including evaporation.

A Marangoni Convection Modeling Research group has been formed under the sponsorship of NASDA to study the various aspects of Marangoni convection described above. As reported in this document, the group has made significant progresses in the past year. Based on the results from these investigations, we decided to conduct microgravity experiments to further our research. The planned microgravity experiment is to verify the physical model, which was proposed by our lead scientist, Prof. Kamotani, to describe the onset of oscillatory thermocapillary flow. To apply the Microgravity Science Research International Announcement of Opportunity (IAO) 2000, a proposal was prepared as a result of deep discussions and hard efforts with all of the members, and was submitted. The proposal document was attached in previous report. We hope that this proposal could be one of references as a guide when researchers desire to apply to microgravity announcement of opportunities. This proposed experiment was selected as a preliminary theme for ISS utilization on Jan. 2002. Therefore, we proceed to the definition phase, and the research plans are going to refined toward the space experiment. The results from the present project will be very important to provide scientific knowledge whether or not the experiment were conducted in space or on the ground.

In October 2003, three Japanese space/aviation research and development organizations were merged into new space agency, Japan Aerospace Exploration Agency (JAXA). The accumulated knowledge, technology and experience in each field will be combined and JAXA prepares a system to perform consistently as a core organization, from basic research through to development and utilization in space. Although JAXA was born, Japanese activities on microgravity science and contributions for the International Space Station (ISS) never change form those of NASDA's period. JAXA's activities on the ISS are as follows; development of Japanese Experiment Module (JEM), development of H-IIA transfer vehicle, development of Centrifuge, operation of JEM, research and promotion of space utilization, development of experimental apparatus (payloads), space experiment, astronaut training, crew health care, safety and product assurance and others.

After October 2003, two offices associated with the ISS Project; Office of Space Flight and Operations (OSFO) and Institute of Space Astronautical Science (ISAS) in JAXA, are re-established and in charge of above-mentioned broad aspect of the ISS Program. The ISS Science Project Office (ISS-pro) is specially established in ISAS office.

Table 1 (1/3). Summary of Experimental studies with a Liquid Bridge (Sounding Rocket and Shuttle Mission)

Experiment Theme	Principal Investigator	Sample Materials	Results	Equipment	Mission	Launch Year
Critical Marangoni Number--Temperature Oscillations in Float Zones	Schwabe, D.; Scharmann, A.	$NaNO_3$	The experiment chamber housed a single, 6-mm diameter, 3.4-mm long $NaNO_3$ sample. Temperature oscillations with the same higher frequency under 1g and 10^{-4} g and with a more complex spectrum occur. The average temperature under 10^{-4} g (343-344 C) is smaller than under 1g (345 C).	TEM 06-2	TEXUS-03b	1981
Marangoni Convection in Float Zones	Chun, Ch.-H.; Wuest, W.	10 cSt Silicone Oil with Ti and TiO_2 tracer particles	A 10 mm long, 10 mm diameter, silicone oil liquid bridge was formed between two co-axial copper discs, subjecting the column to a constant two temperature difference of 7.82 K and 18.9 K. An axisymmetric steady Marangoni flow pattern was observed.	TEM 06-4	TEXUS-03b	1981
Critical Marangoni Number--Temperature Oscillations in Float Zones	Schwabe, D.; Scharmann, A.	$NaNO_3$	The objective of this experiment was to determine critical Marangoni number. Analysis of the thermal data resulting from both the rocket and terrestrial experiments indicated that the onset of temperature oscillations occurred at a temperature difference of 23 K. The corresponding critical Marangoni number for the flight was 9.6×10^3, which was identical to the critical Marangoni number in the 1-g reference experiment.	TEM 06-2	TEXUS-05	1982
Oscillatory Marangoni Convection in Float Zones	Chun, Ch.-H.; Wuest, W.	Methanol with titanium metal powder	The objectives of this experiment were to examine liquid bridges whose corresponding Marangoni numbers were far beyond the critical values, to observe the oscillatory convection and determine if the oscillatory state progresses to a turbulent state, and to study the role of the liquid column aspect ratio. An oscillating flow was demonstrated by the up-and downwards oscillating Marangoni vortex near the free surface.	TEM 06-4	TEXUS-07	1983
Free Convection in Low Gravity	Napolitano, L. G.; Monti, R.	100 & 5 cSt Silicone Oil	The objectives of SL-1 experiments were to establish a stable float zones of 10 cm height, to create Marangoni flow in the zone, and to investigate these Marangoni flows under a number of parameters to determine the local and global properties of the system. Liquid bridges of 7 to 8 cm in length with aspect ratios on the order of one were established. Most importantly, it was reported that the established Marangoni flows were of the boundary layer type.	FPM	SL-1	1983

Table 1 (2/3). Summary of Experimental studies with a Liquid Bridge (Sounding Rocket and Shuttle Mission)

Experiment Theme	Principal Investigator	Sample Materials	Results	Equipment	Mission	Launch Year
Thermal Marangoni Convection in a Floating Zone	Monti, R.	5 cSt Silicone Oil	The specific objectives of the investigation were to study the unsteady thermal conditions in the liquid bridge and characterize the different thermal and flow regimes at relatively high Marangoni numbers. The upper disk was heated to 90 C at a rate of 1 K/s. During the low-gravity phase of the experiment, three different flow regimes were established and examined: laminar (Stokes and boundary layer), oscillatory, and (3) non-periodic.	TEM 06-4	TEXUS-09	1984
Marangoni Flows-A study of surface-driven convection phenomena in very low gravity	Napolitano, L. G.	5 cSt Silicone Oil	The objectives were (1) quantitatively examine thermal Marangoni flows in a single-liquid system, (2) examine the thermal and/or solutal Marangoni flows in a two-liquid system, and (3) analyze the effects of certain parameters.	FPM	SL-D1	1985
Thermal Marangoni Convection in a Floating Zone	Monti, R.	5 cSt Silicone Oil	The specific objective of the experiment was to investigate the onset of Marangoni oscillations under different thermal conditions. The experiment was fully controlled from Italy, using Telescience approach.	TEM 06-4	TEXUS-14b	1986
Critical Marangoni Flow	Monti, R.	2 cSt Silicone Oil	The onset of oscillation regime depends on several parameters. Four oscillation onsets were obtained at different temperature ramps. The experimental results are discussed and compared with numerical simulation.	TEM 06-4	TEXUS-23	1989
Observation of Marangoni Convection	Azuma, H.	10 cSt Silicone Oil	This experiment observed Marangoni convection in steady state and the surface tension waves. The experimental results are in roughly agreement with the result of analytical data.	FTX	TR-IA-1	1991
Marangoni Induced Convection in Materials Processing under Microgravity	Enya, S.	Paraffin	The liquid bridge was formed in microgravity, but any flow could not be observed.	MCU	FMPT	1992
Generation and Control of Marangoni Convection	Hirata, A.	6 cSt Silicone Oil	This experiment investigated micro- mechanism of Marangoni convection. The transition process from laminar flow to oscillatory flow behavior was observed by in-situ observation. The amplitude of Marangoni oscillating flow was very small at initial and increased with time.	FTX	TR-IA-2	1992

Table 1 (3/3). Summary of Experimental studies with a Liquid Bridge (Sounding Rocket and Shuttle Mission)

Experiment Theme	Principal Investigator	Sample Materials	Results	Equipment	Mission	Launch Year
Higher Modes and Their Instabilities of Oscillating Marangoni Convection in a Large Cylindrical Liquid Column	Chun, Ch. -H.	5 cSt Silicone Oil	This experiment investigated transitions from steady thermal Marangoni convection to non-periodic states and of higher oscillating modes in liquid columns as a function of column characteristics.	AFPM	SL-D2	1993
Onset of Oscillatory Marangoni Flows	Monti, R.	Silicone Oil	This experiment investigated the transition from steady to oscillatory thermal Marangoni convection in liquid columns as a function of column aspect ratio, Prandtl number, and thermal profile.	AFPM	SL-D2	1993
Experiment on Generation of Marangoni Convection flow and controlling method	Kuwahara, K	6 cSt Silicone Oil	The experiment verified that electric convection is generated in Silicone oil when DC voltage is applied. Laminar Maranogoni convection flow is generated at the temperature difference of 10K between disks. The flow could be accelerated or restricted controlling the flow caused by electricity.	FTX	TR-IA-3	1993
3D Velocity Measurement of Marangoni Convection in Liquid Column	Kawamura, H.	2 cSt Silicone Oil	The measurement of the three-dimensional velocity profile of the Marangoni convection in a liquid bridge was done by the use of four CCD cameras. A liquid bridge was formed between two 50mm diameter coaxial disks with separation of 33mm. In the first stage with the temperature difference of 10K, the axisymmetric Marangoni convection was observed. As the temperature difference become 50K, the convection had enhanced and a non-axisymetric flow profile, oscillatory Marangoni convection, was observed.	FTX-II	TR-IA-4	1995
Simultaneous Observation of 3D Fluid Flow and Liquid-Bridge Surface Temperature of Unsteady Marangoni Convection	Nishino, K.	Silicone Oil	The Liquid bridge was not formed because a portion of Silicone oil leaked into the outside support disked.	FTX-II	TR-IA-6	1997

TEAM MEMBERS AND RESEARCH ARCHITECTURE

For a systematic approach for studying Marangoni convection and constructing a transition model, the research team was organized as followings:

Leader: **Shinichi YODA** (JAXA)
Lead Scientist: **Yasuhiro KAMOTANI** (Case Western Reserve University/JAXA)

(1) Experimental Effort

High Pr Number Fluids:	**Y. Kamotani** and A. Wang (Case Western Reserve University) **K. Nishino,** and E. A. Matida (Yokohama National University)
Intermediate Pr Number Fluids:	**M. Kawaji**, R.Q. Liang, M. and N.-Esfahany (University of Toronto)
Low Pr Number Fluids:	**S. Yoda**, S. Matsumoto, H. Hayashida, A. Komiya (JAXA), and H. Natsui (AES Co., Ltd)

(2) Numerical Analysis

High and Intermediate Pr Number Fluids:	**H. Kawamura**, I. Ueno (Tokyo University of Science)
Low Pr Number Fluids:	**N. Imaishi**, and S. Yasuhiro (Kyushu University)

(3) Linear Stability Analysis:	**H. C. Kuhlmann**, and Ch. Nienhüser (ZARM - University of Bremen)
(4) Design and Development of Experimental Apparatus:	**K. Kawasaki** (IHI Aerospace Co., Ltd)
(5) Construction of the Model:	**All members**
(6) Secretariat:	**T. Hanyu** (Mitsubishi Research Institute, Inc.)

Part A. Investigations for High Prandtl Fluid

Investiagtion of Free Surface Heat Transfer Effect and Oscillation Mechanisms for Thermocapillary Flow of High Prandtl Number Fluid

By
Y. Kamotani[1], A. Wang[1], and S. Yoda[2]

Abstract: The effect of free surface heat transfer on oscillatory thermocapillary flow in liquid bridges of high Prandtl number (Pr) fluids is investigated experimentally as well as numerically. It has been found that the critical condition is very sensitive to the free surface heat transfer under certain conditions but relatively insensitive under other conditions. In this work it is shown that this sensitivity difference may be related to the difference in the oscillation mechanism. Several oscillation mechanisms have been proposed in the past for oscillatory thermocapillary flows in liquid bridges of high Prandtl fluids, mainly hydrothermal wave type instability and a non-linear mechanism involving dynamic free surface deformation. It is discussed here that the range of Marangoni number, where the flow is found to become oscillatory in many experiments for high Pr fluids, is too low for the flow to become unstable by the hydrothermal wave instability mechanism, or any linear instability mechanism. Instead, we need non-linear mechanisms where the driving force is altered continuously by some means. In order to get this conclusion, our past work is summarized and some new results are presented herein.

1. INTRODUCTION

Thermocapillary flows in liquid bridges are known to become oscillatory for a wide range of Prandtl number. Despite the fact that much work has been done in the past, the transition mechanism for high Pr fluid is not yet well understood. The present work is motivated to clarify the oscillation mechanism. In the process of obtaining more experimental data on the subject, we have found that the heat transfer at the free surface has an appreciable effect on the transition in room temperature tests. Generally, heat is lost from the liquid free surface to the surroundings in room temperature tests. The surrounding air motion caused by the heating-cooling arrangement of the experiment is mainly responsible for the heat transfer, so the heat transfer rate is small compared to the total heat transferred through the liquid. We have shown that the critical Marangoni number (Ma_{cr}) changes by several factors by simply changing this heat transfer condition. This sensitivity is found only when the free surface loses heat.

Recently we have obtained more data under heat gain conditions. For this, we increased the surrounding air temperature by placing the experimental setup in an oven. It is found that under the heat gain condition the free surface heat transfer has no appreciable effect on Ma_{cr}. It is not possible to explain the observed large difference in the sensitivity to the free surface heat transfer between the loss and gain cases by one oscillation mechanism.

It is known that Ma_{cr} depends strongly on the shape of the liquid bridge. Thermocapillary flows in nearly straight liquid bridges and those in concave bridges seem to behave differently under the heat loss condition. We have shown that the aforementioned sensitivity to the free surface heat transfer is true for nearly straight bridges, but the critical conditions for concave liquid bridges are much less sensitive to it. In fact, the critical condition for

---

[1] Case Western Reserve University, Cleveland, Ohio 44106, USA
[2] Japan Aerospace Exploration Agency, 2-1-1 Sengen, Tsukuba, 305-8505, Japan

concave bridges is not sensitive to either heat loss or gain. Again, it seems difficult to explain this difference in the nearly flat and concave bridge behaviors unless we assume that something is fundamentally different in these two situations.

As in our past work, numerical simulations are performed in order to study the surrounding air motion and compute the resultant heat transfer rate at the free surface. All of our past data and more recent data are put together in order to discuss the relation between the oscillation mechanism and the sensitivity to the free surface heat transfer.

2. EXPERIMENT

The experimental apparatus is described in our previous work [1,2], so it is not repeated herein. It is a standard arrangement in which liquid is suspended between a heated top cylindrical rod and a cooled bottom rod. The liquid bridge diameters are D = 2 and 3 mm. Silicone oils with 2 and 5 centistokes kinematic viscosity are used as the test fluids. The static free surface shape is varied from flat to concave. Most of the tests are conducted in an oven. In a typical test, we fix the cold wall temperature (T_C) and air temperature (T_R) at specified values and increase the hot wall temperature until the flow becomes oscillatory.

3. NUMERICAL SIMULATION OF AIR MOTION

In the simulation study the airflow and the liquid flow are solved simultaneously because they are coupled through the boundary conditions at the free surface. The computational domain for the airflow analysis is consistent with the experimental conditions [3-5]. We mainly analyze the airflow for the experimentally found critical conditions in order do relate the critical conditions to the free surface heat transfer. The local heat flux (q) is non-dimensionalized as $qR/(k\Delta T)$, which is called the local Biot number ($Bi_{,loc}$), where k is the liquid thermal conductivity and R is the liquid bridge radius. The total free surface heat transfer rate (Q) is non-dimensionalized as $Q/(2\pi Lk\Delta T)$, which is called the average Biot number (Bi). Conventionally, Biot number represents heat transfer coefficient so that the net heat transfer depends on the Bi and the temperature difference between the liquid surface and the surrounding air. Instead of specifying both, the current Bi represents, by itself, the net heat transfer from the free surface.

4. IMPORTANT DIMENSIONLSS PARAMETERS

The important dimensionless parameters for the thermocapillary flow in the liquid bridge configuration in the absence of gravity are: Marangoni number $Ma = \sigma_T \Delta TL/\mu\alpha$, Prandtl number $Pr = \nu/\alpha$, and aspect ratio $Ar = L/D$, where σ_T is the temperature coefficient of surface tension, μ is the dynamic viscosity of the liquid, ν is the liquid kinematic viscosity, and α is the liquid thermal diffusivity. L is the liquid column length and D is the liquid column diameter. Additionally, Kamotani and Ostrach [2] introduced the aforementioned S-parameter. The S-parameter represents the effect of dynamic free surface deformation on the oscillation phenomenon, and is expressed, for the present configuration, as $S = (\sigma_T \ \Delta T/\sigma)/PrMa^{3/14}$, where σ is the surface tension at the free surface. In order to describe the shape of the liquid bridge, diameter ratio, Dr, is used, which is defined as $Dr = D_{min}/D$, where D_{min} is the diameter of the liquid at the neck (Dr = 1 for straight bridge). The thermal effect of the surrounding airflow is represented by the local and average Biot numbers as explained above. The following parametric ranges are covered in the present work: $Ma < 5.0 \times 10^4$, $24 < Pr < 50$, $Ar = 0.65\text{-}0.7$, and $0.4 = Dr = 1.0$. For Ma and Pr, the fluid properties are evaluated at the fluid mean temperature, $\frac{1}{2}(T_H + T_C)$.

5. RESULTS AND DISCUSSION

5.1 Nearly Straight Liquid Bridge with Free Surface Heat Loss

In a typical room temperature experiment, T_H (at the critical condition) is higher than T_R, so heat is lost from the free surface. The results with nearly straight liquid bridges have already been reported [3-6]. In summary, the critical condition is very sensitive to the heat transfer and, contrary to what some theoretical studies have shown, the flow is destabilized with increasing heat loss. After computing the Biot number for each critical condition, Ma_{cr} is plotted against Bi for fixed Pr and Ar, which is reproduced in Fig. 1. The figure shows that the critical condition cannot be described by Ma_{cr} and Bi alone. The figure also shows that Ma_{cr} changes substantially over a relatively narrow range of Bi, or even when the basic flow is not substantially altered. It seems that the heat loss effect cannot be explained by a linear stability concept.

For this reason the critical results are in the form of S vs. Bi (or modified Biot number $Bi/Pr^{0.5}$), as shown Fig. 2. It shows that the critical conditions for all of our tests can be correlated reasonably well by S and $Bi/Pr^{0.5}$. The reason why Bi is modified as $Bi/Pr^{0.5}$ is discussed in [6]. We have also conducted the heat loss experiment under the condition in which forced airflow removes heat from the free surface. It was shown that the data from the forced cooling tests also agree well with the trend of Fig. 2 [5].

As shown by Kamotani and Ostrach [2], the flow is viscous dominated even when the Reynolds number ($Re = Ma/Pr$) is as large as 1000 in the case of high Pr fluids. The flow is viscous dominated because the main driving force exists in a relatively small region near the hot wall called the hot corner. The hot corner shrinks as Ma (or Re) increases, which tends to keep the flow viscous dominated. The S-parameter model is based on the viscous flow. If Re becomes larger than about 1000, the inertia forces will become important, so the situation will be different. As Fig. 1 shows, Ma_{cr} can be as large as $(3 - 5) \times 10^4$ (or Re is about 1000) when the heat loss is minimized, which is about the limit of the S-parameter model. It is interesting that with decreasing heat loss the S-parameter increases up to the limit of its validity.

The value of Ma_{cr} when the heat loss is minimized (around 4×10^4) is near the critical values predicted numerically for $Pr \sim 25$ in the past without dynamic free surface deformation. For example, Savino and Monti [7] predict $Ma_{cr} = 4.2 \times 10^4$ for $Pr = 30$ and $Ar = 1$. In the current JAXA project, Kawamura et al. are conducting extensive numerical simulations for high Pr fluids with and without dynamic free surface deformation. Their prediction of Ma_{cr} is 3.25×10^4 for $Pr = 28.1$ and $Ar = 0.5$ [8]. We are also conducting 3-D numerical simulations with undeformable free surface to investigate the free surface heat transfer effects (to be reported in the future). Ma_{cr} in our work is also near these predicted values ($Ma_{cr} = 4.2 \times 10^4$ for $Ar = 0.7$ with insulated free surface). One important feature of the computed instability is that the inertia forces play an important role since Re is large. In fact, in our numerical simulations the flow will not oscillate if we do not include the inertia terms in the equations. Recently, Sim and Zebib [9] analyzed oscillatory thermocapillary flow of $Pr = 27$ numerically. They tried to simulate the experiments by Masud et al. [1], including concave bridges. The predicted $Ma_{cr} = 5{,}700$ for insulted free surface by Sim and Zebib seems too low (the inertia forces and convection are too weak to cause any instability). In any case, their results show that Ma_{cr} is sensitive to the free surface heat transfer and Ma_{cr} is shown to increase with increasing heat loss. In contrast, our simulations show that the heat loss decreases Ma_{cr} up to about $Bi = 0.5$ and then increases Ma_{cr} with further increase in Bi. The reduction of Ma_{cr} is due to the fact that the overall liquid velocity increases with increasing heat loss. However, the effect is not strong: Ma_{cr} changes from 4.2×10^4 to 3.0×10^4 when Bi is changed from 0 to 0.5. Then, when Bi is increased further, the heat loss shrinks the hot corner so that the inertia forces in the bulk region decreases, resulting in Ma_{cr} increase. Therefore, it is not possible to predict oscillations around experimentally found $Ma_{cr} = 1.5 \times 10^4$ in room temperature tests (heat loss tests) in which Bi = 0.5. Ma_{cr} becomes as low as 7,000 in the large heat loss tests (Bi ˜ 1, see Fig. 1). All in all, the instability shown numerically for high Pr fluids does not seem to be the same phenomenon as the one we observe experimentally.

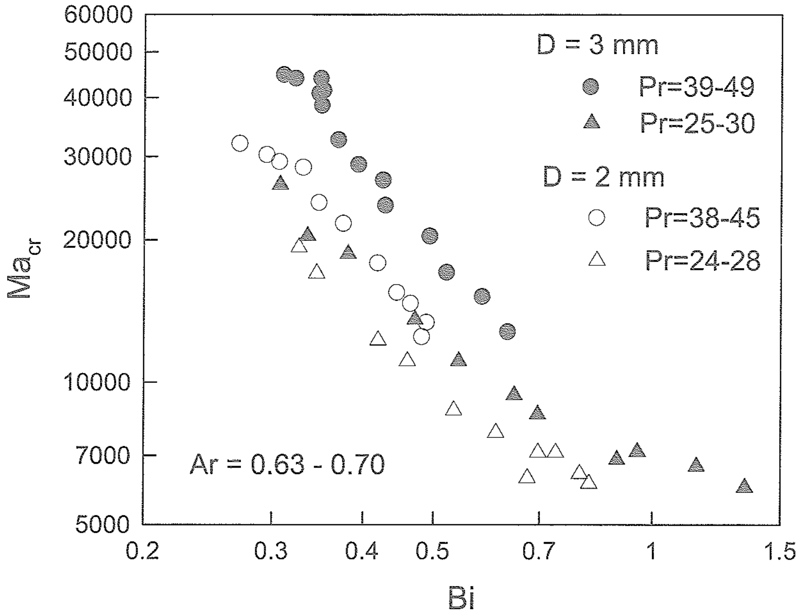

Fig. 1 Correlation of critical Marangoni number with average Biot number

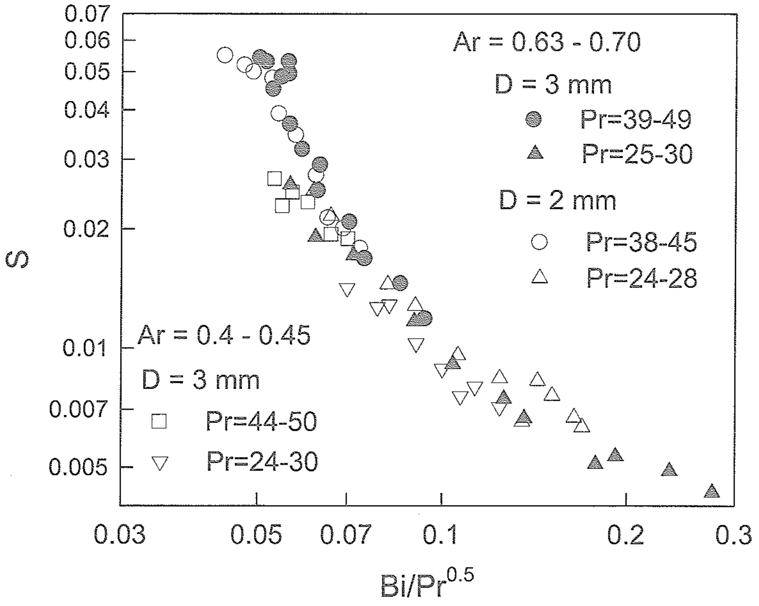

Fig. 2 Correlation of S-parameter at critical condition with modified Biot number

Typical streamlines and isotherms with free surface heat loss are presented in Fig. 3. Since the flow is driven in the hot corner, the center of the recirculating flow is situated near the hot wall. As a result, the recirculating flow pattern generates a relatively large region where the flow moves radially inward. This radial convection tends to make the bulk fluid temperature distribution rather uniform near the free surface. As will be discussed later, uniform radial temperature distribution in the surface flow region is not conducive to the hydrothermal wave instability.

From these observations, our conclusion is that it is not possible to make the flow unstable around Ma = 10^4 by the hydrothermal wave instability mechanism. It seems that the only way to make the flow time-dependent near this low Ma is to change the driving force in the hot corner by non-linear means. Based on the S-parameter correlation of Fig. 2, the dynamic free surface deformation in the hot corner is indeed changing the driving force during oscillations.

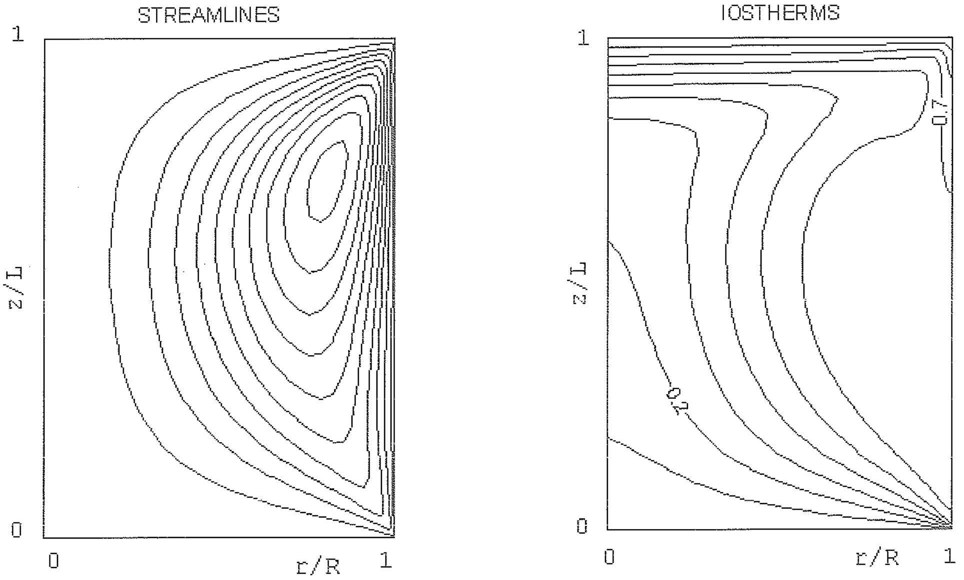

Fig. 3 Computed streamlines and isotherms of liquid flow
(Ma=1.2×10^4, Pr=28, D=3 mm, Ar=0.7, Dr=1.0, Bi=0.38)

5.2 Nearly Straight Liquid Bridge with Free Surface Heat Gain

As we increase T_R in the oven, T_R becomes eventually greater than T_H at the critical condition. In this situation the liquid bridge gains heat form the environment. Fig. 4 shows how ΔT_{cr} changes with increasing T_R (or, more appropriately, T_R-T_C) for nearly flat free surface shape. For the reason to be discussed later, we cannot take data for Dr = 1 with heat gain, so the data in Fig. 4 for the heat gain case are for Dr slightly less than unity. As the figure shows, ΔT_{cr} increases up to a certain T_R-T_C but drops suddenly beyond this T_R-T_C. It appears that there are two different branches in Fig. 4. The changeover temperature difference depends on the liquid diameter. The same data are plotted in terms of the computed Bi and presented in Fig. 5. Bi is positive for net heat loss and negative for net heat gain. Figure 5 shows that the sudden change in Ma_{cr} occurs when the free surface heat transfer changes from net loss to gain. Once we get into the heat gain situation, Ma_{cr} becomes relatively insensitive to Bi ($\mathrm{Ma}_{cr} \sim 1.4 \times 10^4$) . Also, Ma_{cr} does not depend on the diameter. Therefore, it seems that Ma_{cr} is the proper parameter to specify the critical condition in the case of heat gain. Apparently, the oscillation mechanism changes suddenly once we get into the heat gain range.

Before we discuss the oscillation mechanism, it is important to know how the liquid flow is affected by the net heat gain. Typical streamlines and isotherms with heat gain are shown in Fig. 6. With heat gain, the bulk fluid temperature increases so that the temperature gradient in the hot corner decreases. On the other hand, the surface temperature gradient in the cold corner increases. Consequently, the hot corner becomes less active and the cold corner becomes more active with the free surface heat gain, which makes much of the surface flow originating from the hot corner go into the cold corner (see Fig. 6). However, the main driving force is still in the hot corner in the range of Bi investigated herein. Therefore, the oscillations still originate from the hot corner. One visible feature of the oscillatory flow with heat gain is an increased activity in the cold corner. Apparently, the cold corner is assisting the oscillation mechanism in some way. Our numerical simulations for Dr = 1 show that the flow is stable around Ma = 1.4 ×10^4 even when the heat gain is large (Bi = -1). Therefore, the oscillation mechanism for the observed oscillations with heat gain must also include the free surface curvature.

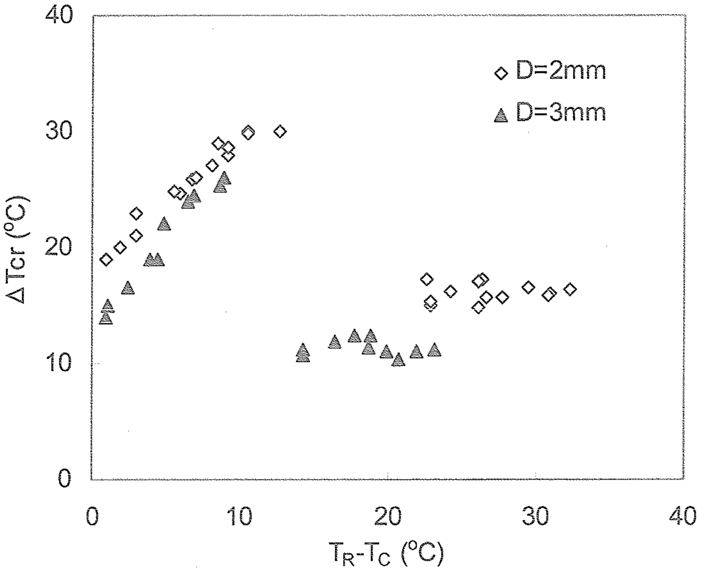

Fig. 4 Critical ΔT for nearly straight liquid bridge with heat gain and loss

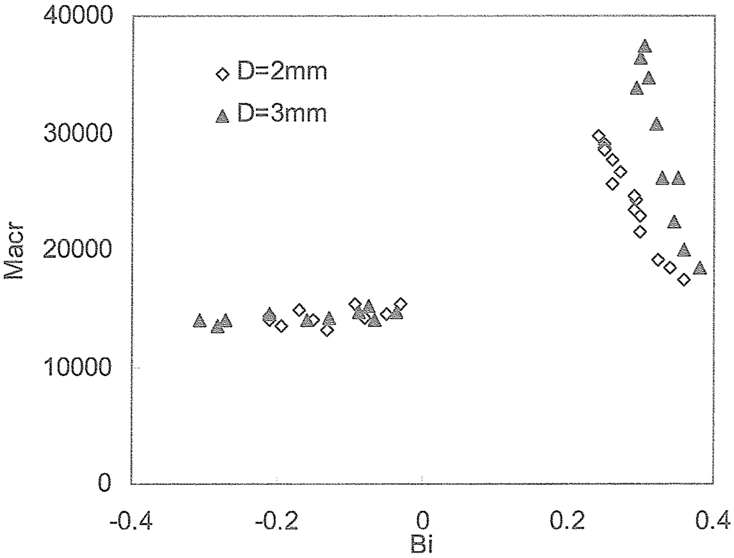

Fig. 5 Critical Ma vs. Bi for nearly straight liquid bridge with heat gain and loss

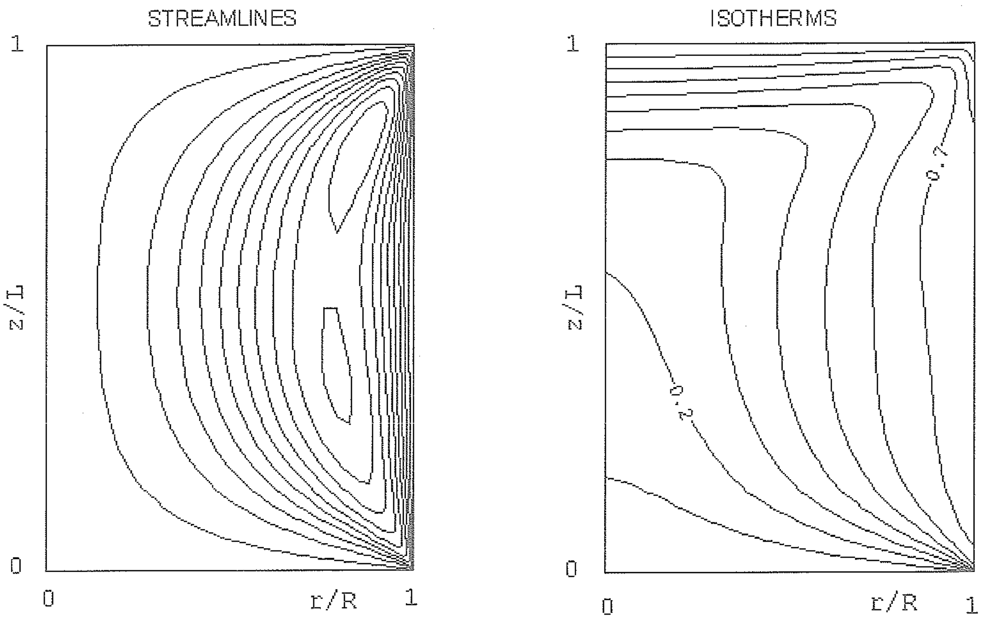

Fig. 6 Computed streamlines and isotherms of liquid flow
($Ma=1.2\times10^4$, $Pr=28$, $D=3$ mm, $Ar=0.7$, $Dr=1.0$, $Bi=-0.38$)

5.3 Concave Liquid Bridge with Free Surface Heat Loss or Gain

Tests with concave free surfaces are commonly done near room temperature. Typical results of room temperature tests for concave free bridges are shown in Fig. 7. It is well known that the Ma_{cr}-Dr curve has two branches: one for nearly flat surface (called the fat branch) where Ma_{cr} increases with decreasing Dr, and the other branch for concave surface (the slender branch) where Ma_{cr} is relatively unaffected by Dr. The changeover occurs suddenly across a certain Dr (Dr of about 0.8 for Ar=0.7 as seen in Fig. 7). This sudden change is similar to that found for the case of nearly flat free surface when the net heat transfer changes from loss to gain. As will be discussed later, this changeover for the concave free surface case is also due to a change in the oscillation mechanism. Although the so-called shape effect is usually shown in a graph similar to Fig. 7, it does not give a complete picture because it does not contain free surface heat transfer information except that the tests are done under the heat loss conditions.

Some results from the heat loss tests (room temperature tests with variable T_C) are presented in Fig. 8. As discussed above, Ma_{cr} increases with decreasing heat loss (decreasing Bi) for nearly flat free surface. Figure 8 shows that this trend holds for the fat branch ($Dr > 0.8$). Ma_{cr} for D r= 0.9 is larger than that for Dr = 1.0 until they become nearly equal beyond Bi of about 0.5. However, Ma_{cr} is not affected appreciably by the heat transfer in the case of concave free surface (slender branch). This trend for the slender branch remains the same even when the heat transfer changes to net gain, as shown in Fig. 9.

The only important effect of free surface heat transfer is that the slender branch extends to larger value of Dr as the surface heat transfer changes to net gain, as shown in Fig. 10. It is not possible to perform heat gain tests in the fat branch because T_R becomes too large. The vapor of the test liquid tends to condense on the cold wall when T_R-T_C becomes large, which can destroy the bridge if the condensation is too much. Our data indicate that the transition to the fat branch occurs around Dr = 1 in the heat gain tests. This is the reason we do not have heat gain data for exactly Dr = 1 in Figs. 4 and 5.

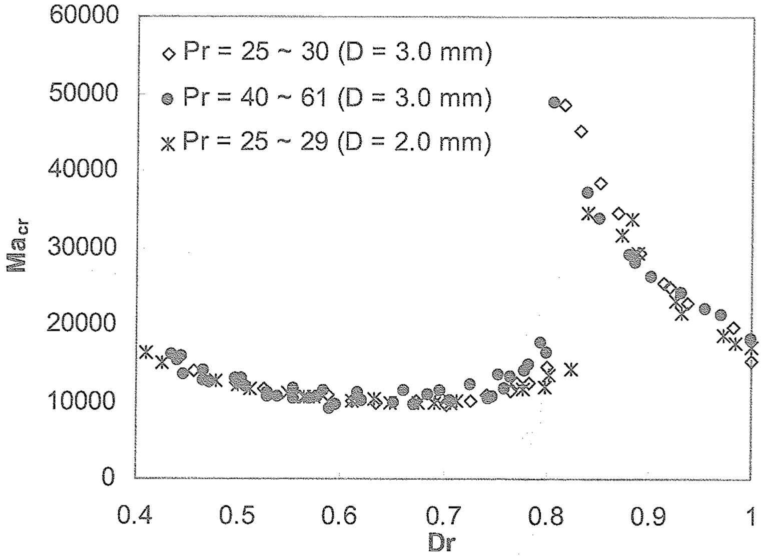

Fig. 7 Ma_{cr} vs. Dr (Ar ~ 0.7) for heat loss tests

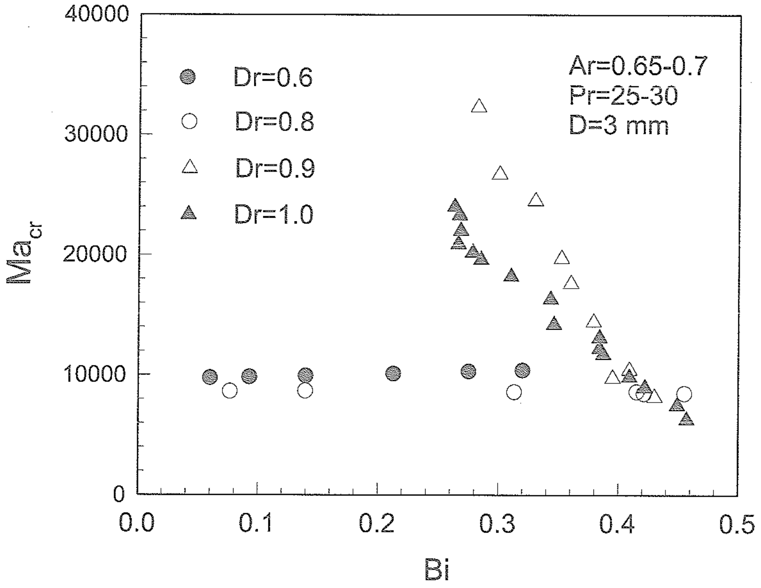

Fig. 8 Ma_{cr} vs. Bi for heat loss tests with various Dr (D=3 mm, Ar=0.67, T_R=23°C))

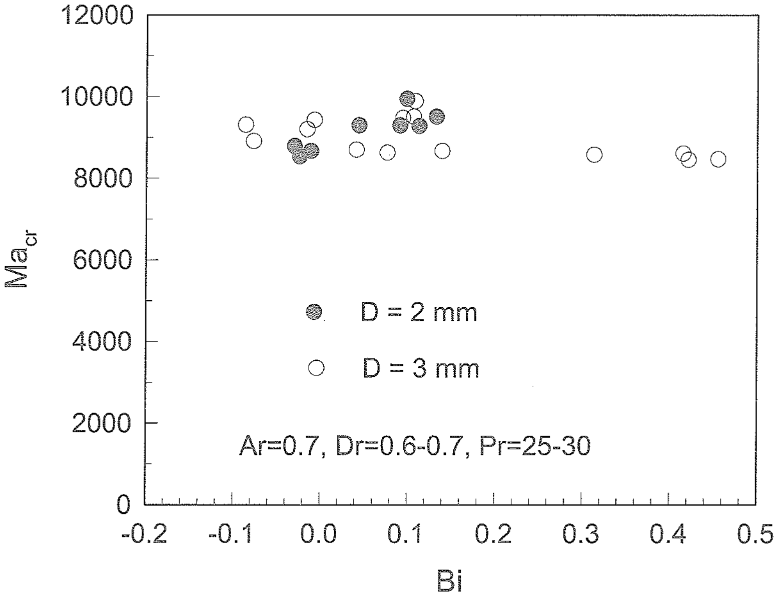

Fig. 9 Ma_{cr} vs. Bi for concave liquid bridge with heat gain and loss

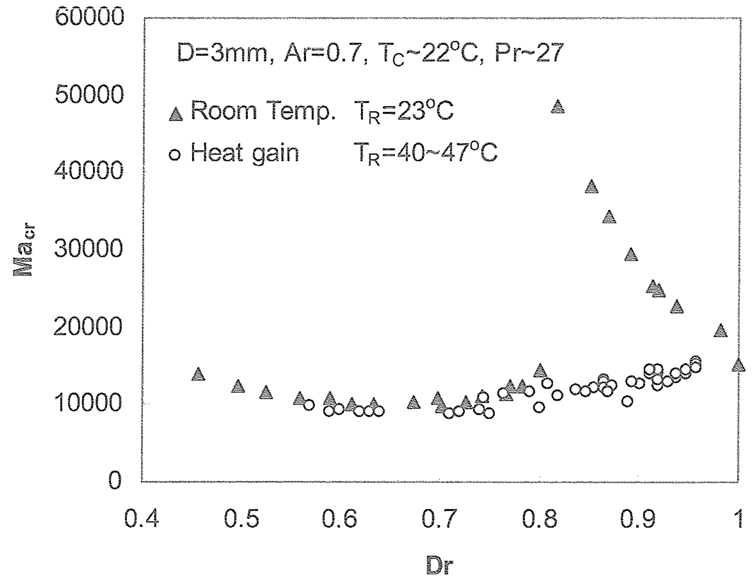

Fig. 10 Ma_{cr} vs. Dr with heat loss and gain

In order to see how the liquid flow structure changes with the shape, the computed streamlines are shown in Fig. 11 for the insulated free surface case. As the surface becomes more concave, the hot and cold corners become increasing narrow zones. Consequently, the flows in the corners are increasingly suppressed. The free surface velocity distributions for the conditions of Fig. 11 are given in Fig. 12, which shows this trend. In order to show this trend from a different angle, the ratio of the free surface temperature gradient (along the free surface direction) at the mid-height, $(dT/ds)_{L/2}$), to that at the location where the surface velocity becomes a maximum near the hot wal, $(dT/ds)_{hot}$), is computed for various Dr. The former location represents the bulk region and the latter location represents the hot corner. The ratio is given in Fig. 13. As the figure shows, the ratio increases, meaning that the driving force in the bulk region becomes more important, as Dr is decreased. Knowing that the bulk region has more surface area than the hot corner, the main driving force region clearly shifts from the hot corner to the bulk region below a certain Dr. Figure 13 shows that the ratio begins to increase sharply below about Dr of 0.8. As discussed above (Fig. 7), Ma_{cr} changes appreciably across the value of D ~ 0.8 for Ar = 0.7. Apparently, this change coincides with the shift of the main driving force from the hot corner to the bulk region. This suggests that there is a shift from the S-parameter mechanism to a different mechanism below Dr of 0.8. With decreasing Dr, the flow is squeezed in the neck region, so the overall flow slows. When the surface is highly concave, the return flow from the cold region (region below the neck) to the hot region is partially blocked by the neck. As a result, a secondary cell appears in the cold region, as seen Fig. 11.

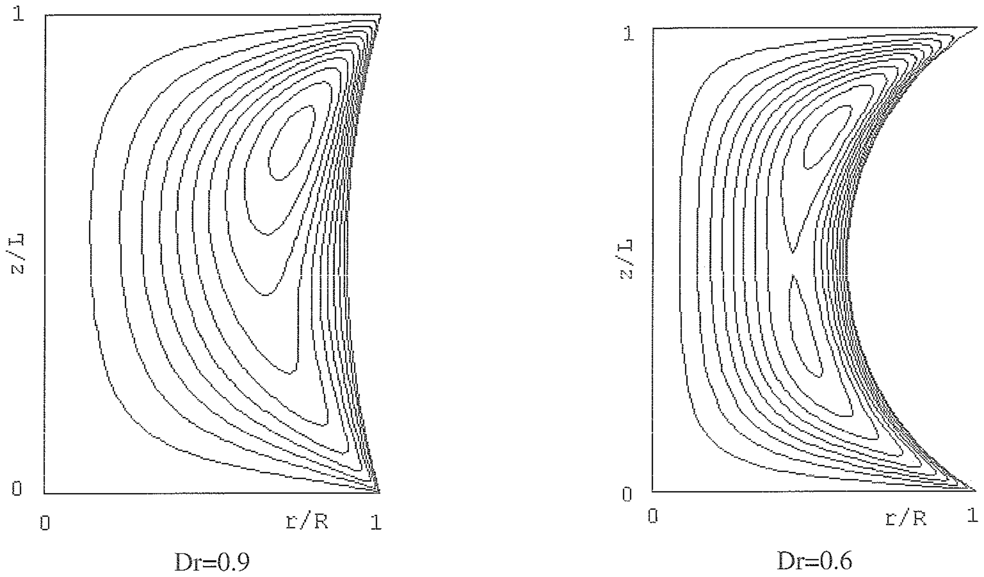

Dr=0.9 Dr=0.6

Fig. 11 Computed streamlines of liquid flow with insulated free surface ($Ma=1.0\times10^4$, Pr=28, D=3 mm, Ar=0.7)

As in the heat gain case for nearly flat free surface, Ma_{cr} is rather low, less than 10^4, so that the hydrothermal waves cannot occur with highly concave surface. The S-parameter mechanism is not important either since the flow is not driven in the hot corner. The only known other mechanism is the one we investigated earlier based on two-dimensional simulations [10]. Since the flow is squeezed at the neck, the return flow below the neck has difficulty to pass the neck region together. This slowing of the flow in the neck region increases the surface temperature gradient in the region. This situation is unstable against three-dimensional disturbances. Eventually, when Ma becomes large enough, the return flow begins to take turn to pass the region in a three-dimensional manner. For example, in the case of oscillation pattern of mode number one, half of the return flow passes through the neck and the remaining half is blocked from the passage. After the passage, the surface temperature gradient decreases as the hot and cold regions mix, but the gradient increases in the region where the return flow is blocked. Eventually, the flow pattern is reversed, resulting in oscillations with rotating temperature and velocity patterns.

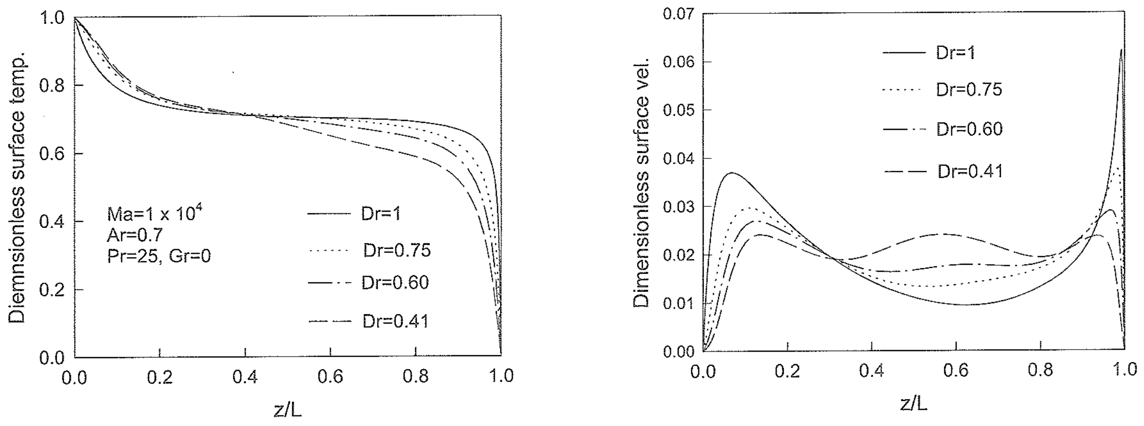

Fig. 12 Surface temperature and velocity variations with diameter ratio for Bi=0

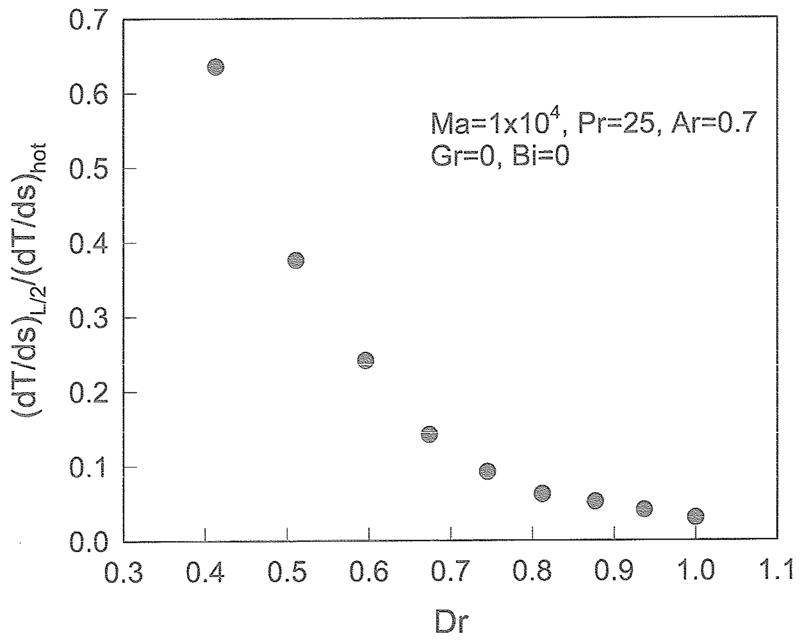

Fig. 13 Surface temperature gradient ratio as a function of Dr

The above oscillation mechanism depends on the existence of the neck region, so it does not apply to fat bridges. However, the data in Fig. 10 show that the trend of Ma_{cr} for concave bridges continues smoothly to that for slightly concave bridges with heat gain. Actually, a close examination of the data show that Ma_{cr} begins to increase slightly with increasing Dr beyond about Dr = 0.8. Therefore, the oscillation mechanism for concave bridges is somewhat modified but still applicable even to a slightly concave bridge in the presence of heat gain. The heat gain activates the cold corner in the case of nearly flat bridge, as discussed above. This situation is similar to the activation of the flow in the cold region due to the neck in the case concave bridge. Although more work is needed, this similarity may explain the trend of Ma_{cr} for slightly concave bridge with heat gain.

5.4. Discussion of Oscillation Mechanisms

Much has been discussed in the past concerning the mechanism of thermocapillary oscillation phenomenon in liquid bridges. The mechanism for low Prandtl number fluids ($Pr \sim 0.01$) is well understood; a result of hydrodynamic instability as the Reynolds number (or inertia forces) becomes sufficiently large. On the other hand, the oscillation mechanism for high Pr fluids ($Pr > 15$) is still being debated. Two models have been proposed in the past for high Pr fluids. One is the S-parameter model by Kamotani and Ostrach [2] and the other is a linear stability model. In the S-parameter model, the fact that the flow is mainly driven in the hot corner is taken into account and the dynamic free surface deformation in the hot corner plays an important role. In contrast, no dynamic free surface deformation is considered in the linear stability model, which predicts the appearance of hydrothermal waves.

Since the hydrothermal wave instability is often cited as the only cause of the various oscillatory thermocapillary flows of high Pr fluids, it is important to know under what conditions the hydrothermal wave-type instability occurs. Based on the linear stability analyses by Smith and Davis for thin liquid layers [11] and Wanschura et al. for liquid bridges [12], the following conditions are important for the appearance of hydrothermal waves in high Prandtl number liquids.

(i) The basic flow is driven by the axial temperature gradients along the free surface. The Marangoni number of the flow is sufficiently large so that convection heat transfer is important.

(ii) Temperature gradients also exist in the radial direction (or in the direction normal to the free surface). These radial temperature gradients are produced by the main axial convection. In particular, the radial temperature gradients near the free surface are due to the convection by the main free surface flow.

(iii) The axial dimension of the hydrothermal waves predicted for liquid bridges scales with the bridge length. Also, the disturbance flow in the axial direction is relatively small.

The observed oscillation phenomenon in room temperature experiments has some features that are different from the above features of the hydrothermal waves.

(i) The disturbance flow in the axial flow direction is quite prominent.

(ii) Since the radial convection by the disturbance flow must be uniformly important over the bridge length and since the end wall tends to generate axial disturbance flow in the corner region, the only region where such waves could be generated is the bulk region, not the hot corner.

(iii) When heat is lost at the free surface, the radial temperature gradient in the surface flow region is reduced (see Fig. 3). Such a condition is not conducive to the hydrothermal wave instability.

(iv) As discussed earlier, numerical simulations show that it is not possible to have hydrothermal wave type instability at a Ma as low as about 10^4.

(v) The work by Wanschura et al. [12] is up to Pr of about 4, and no accurate linear stability work exists for the Prandtl number range of current interest, namely $Pr > 15$.

Therefore, the observed oscillatory flows of high Pr fluids are not due to the hydrothermal wave instability. From our earlier studies together with the present investigation of free surface heat transfer effects, we have identified two oscillation mechanisms that are not based on linear stability theory. Our S-parameter model holds if (i) the free surface is nearly flat, and (ii) the free surface is thermally insulated or it loses heat to the environment. Note that many experiments performed in the past belong to this case. The correlation of the critical conditions shows that the oscillation mechanism represented by the S-parameter is responsible for the transition. The oscillations are a result of dynamic free surface deformation altering the main driving force in the hot corner periodically. The condition for the onset of oscillations is very sensitive to the free surface heat loss in the S-parameter range, because it is coupled with very small free surface deformation.

In the case of curved free surface, the driving force in the bulk region becomes increasingly important as the shape becomes more concave. As a result, the oscillation mechanism shifts from the S-parameter to an oscillation mechanism associated with the bulk region, as Dr is decreased. The oscillations are a result of the flow passing through the neck region in a three-dimensional and time-dependent manner. Since no small quantities are involved in this case, such as the dynamic free surface deformation, the critical condition is not very sensitive to the free surface heat transfer. With heat gain, a similar mechanism holds even for slightly concave bridge.

6. CONCLUSIONS

The effects of free surface heat loss and gain on the conditions for the onset of oscillatory thermocapillary flow are investigated experimentally in liquid bridges of high Prandtl fluids. Both straight and concave liquid bridges are investigated. The free surface heat transfer rate is computed numerically. Nearly straight liquid bridges are very sensitive to the free surface heat loss, the flow being destabilized with increasing heat loss. However, they are not sensitive to free surface heat gain. Concave liquid bridges are not sensitive to gain or loss. It is discussed that for nearly straight bridges with heat loss (including insulated free surface), the onset of oscillations is specified by the S-parameter. On the other hand, for concave bridges with heat gain or loss and for nearly straight bridges with heat gain, the oscillation mechanism is associated with the convection in the bulk region so that Ma_{cr} can specify the critical condition.

REFERENCES

[1] Masud, J., Kamotani, Y., and Ostrach, S., "Oscillatory Thermocapillary Flow in Cylindrical Columns of High Prandtl Number Fluids," Journal of Thermophysics and Heat Transfer, Vol. 11 (1997), pp. 105-111.

[2] Kamotani, Y. and Ostrach, S., "Theoretical Analysis of Thermocapillary Flow in Cylindrical Columns of High Prandtl Number Fluids," Journal of Heat Transfer, Vol. 120 (1998), pp. 758-764.

[3] Kamotani, Y., Wang, Li, Hatta, S., Bhunia, P., and Yoda, S., "Study of Oscillatory Thermocapillary Flow of High Prandtl Number Fluid," Annual Report (April 2000 – March 2001), Marangoni Convection Modeling Research, NASDA-TMR-010015E, December 2001, pp. 25-42.

[4] Kamotani, Y., Wang, Li, Hatta, S., and Yoda, S., "Investigation of Free Surface Heat Transfer Effect on Oscillatory Thermocapillary Flow of High Prandtl Number Fluid," Annual Report (April 2001 – March 2002), Marangoni Convection Modeling Research, NASDA-TMR-020026E, December 2002, pp. 25-41.

[5] Kamotani, Y., Wang, A. and Yoda, S., "Investigation of Free Surface Heat Transfer Effect on Oscillatory Thermocapillary Flow of High Prandtl Number Fluid," Annual Report (April 2002 – March 2003), Marangoni Convection Modeling Research, NASDA-TMR-030004E, August 2003, pp. 21-41.

[6] Kamotani, Y., Wang, Li, Hatta, S., Wang, A., and Yoda, S., "Free Surface Heat Loss Effect on Oscillatory Thermocapillary Flow in Liquid Bridges of High Prandtl Number Fluids," International Journal of Heat and Mass Transfer, **46**, 2003, pp. 3211-3220.

[7] Savino, R. and Monti, R., "Oscillatory Marangoni Convection in Cylindrical Liquid Bridges," Physics of Fluids, Vol. 8 (1996) pp. 2906-2922.

[8] Hashimoto, T., Ueno, I., Kawamura, H., and Yoda, S., "Numerical Simulation of Marangoni Convection in Consideration of Free Surface Displacement (Part 6)," Annual Report (April 2002 – March 2003), Marangoni Convection Modeling Research, NASDA-TMR-030004E, August 2003, pp. 67-98.

[9] Sim, B.-C. and Zebib, A., "Thermocapillary Convection in Cylindrical Liquid Bridges and Annuli," Comptes Rendus Mecanique, Vol. 332 (2004), pp. 473-486.

[10] Gupta, S., Kamotani, Y., Masud, J., and Yoda, S., 'A Numerical Simulation of Thermocapullary Convection in Two-Dimensional Liquid Bridges," AIAA Paper, AIAA-2000-0794, 2000.

[11] Smith, M. K. and Davis, S., "Instabilities of Dynamic Thermocapillary Liquid Layers. Part I: Convective Instabilities," J. Fluid Mech., **132**, 1983, pp. 145-162.

[12] Wanschura, M., Shevtsova, V. M., Kuhlmann, H. C., and Rath, H. J., "Convective Instability of Thermocapillary Convection in Cylindrical Liquid Bridges," Physics of Fluids, **7**, 1996, pp. 912-915.

Dynamic Surface Deformation of Cylindrical Bridge of High Prandtl Number Fluid in Oscillatory Thermocapillary Convection
— Tspi Measuremet and G-jitter Effect —

By
K. Nishino[1], X. Li[1], Y. Kanashima[1] and S. Yoda[2]

Abstract: This report describes experimental studies conducted at Yokohama National University during 2003 JFY as a part of the Project Research on Marangoni Convection of National Space Development Agency of Japan (NASDA)[#]. The work consists of (1) the development of a new measuring method for dynamic surface deformation (DSD, hereafter) of cylindrical bridge of high Prandtl number fluid and (2) the study of g-jitter effect on DSD in a simulated g-jitter environment.

In the first work, a technique based on temporal speckle pattern interferometry (TSPI) is developed to make two-dimensional measurement of DSD in oscillatory thermocaplillary convection. The technique is designed to have a resolution of better than 0.1μm and be applicable to a curved liquid surface. Its performance is verified through a series of measurements targeting a flat mirror, a glass rod and a liquid bridge, all of which show dynamical surface displacement or deformation. The success of the measurement is due to the special phase-unwrapping algorithm devised for the measurement of oscillatory surface displacement or deformation.

In the second work, effects of g-jitter on the measurement of DSD caused by the oscillatory thermocapillary convection in a liquid bridge is studied experimentally. A vibration table driven by a piezoelectric actuator is constructed to generate g-jitters of realistic amplitude and frequency spectra. A micro-imaging displacement meter is used to measure DSD in the presence of g-jitter. It is shown that the natural DSD in the oscillatory state of thermocapillary convection is well separated in the frequency domain from that caused by harmonic and non-harmonic g-jitters. It is concluded that the DSD measurement in the future ISS experiment is feasible even in the presence of g-jitter there.

1. Development of DSD Measuring Technique Based on TSPI

1.1 Introduction

Electronic speckle pattern interferometry (ESPI) offers a versatile technique for measuring, with sub-micron accuracy, out-of-plane and in-pane displacements, vibrations, slopes and curvatures of optically rough surfaces, as summarized by Jones and Wykes (1983) and Rastogi et al. (2001). ESPI's advantages over other classical interferometric techniques lie in its relaxed requirement for reference surface, readiness of digital recording and so on. These features will also provide advantages for the measurement of specular and deformable surfaces such as liquid free surfaces. Unfortunately, ESPI has rarely been applied to such surfaces because they do not generate speckled wave fronts when illuminated by coherent light. This issue is, however, resolved by some methods. One idea is to let reference and/or object wave fronts impinge onto a rough surface placed in front of the camera.

---

[1] Yokohama National University, 79-5 Tokiwadai, Hodogaya-ku, Yokohama 240-8501, Japan
[2] Japan Aerospace Exploration Agency (JAXA), Sengen 2-1-1, Tsukuba-shi, 305-8505, Japan
[#] NASDA is now reorganized into Japan Aerospace Exploration Agency (JAXA).

Verga et al. (1998) used a ground glass to generate speckled wave fronts for measurement of liquid surface deformation. Another idea is to illuminate liquid surface with speckled light as proposed by Roussev et al. (1999). They measured the shape of a thin liquid layer on a flat plate whose backside is roughened to generate speckled light. Speckle images generated by these methods can be analyzed with the same procedures as those developed for ESPI measurement of rough surfaces.

The present study aims at developing a technique based on ESPI that can be used for the measurement of micron-order motion of a deformable liquid free surface. Our specific target is a quasi-cylindrical surface of a small liquid bridge, 2-5mm in diameter and 2-5mm in length, which is formed between two coaxial disks heated differentially for generating thermocapillary convection. Figures 1(a) and 1(b) show respectively the disk apparatus and the side-view photo of the liquid bridge targeted in the present study. This particular fluid geometry has been studied extensively (e.g., Kamotani and Ostrach 1998) from a viewpoint of flow instability due to thermocapillarity. The instability occurs when the temperature difference between the disks exceeds a certain critical value, causing the onset of micron-order motion of the liquid free surface. The fact that the magnitude of surface displacement can be less than 1mm requires quite a sensitive measuring technique to be developed. We have chosen ESPI for this purpose not only because of its advantageous features mentioned above but also because of the presence of large surface curvature that would make application of other conventional interferometric techniques very complicated. This latter advantage is exploited by van der Auweraer et al. (2002) in their measurements of surface shapes of complex three-dimensional models. Verga et al. (1998) also developed an ESPI system for measuring deformation of comparatively flat liquid surface.

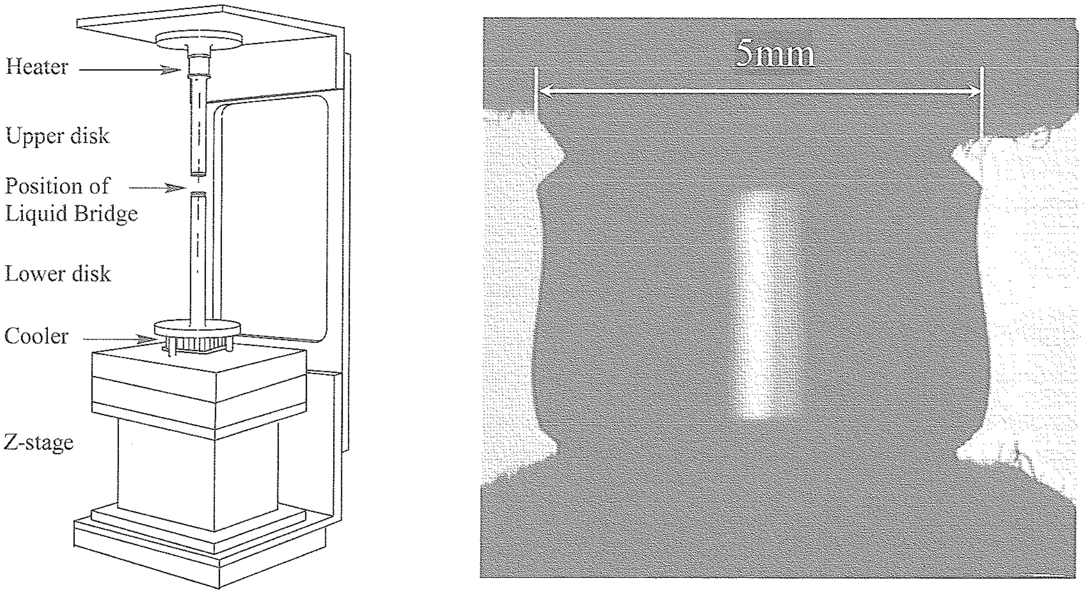

(a) (b)

Fig. 1 Apparatus and photo of liquid bridge: (a) the disk apparatus for sustaining liquid bridge; (b) photo of liquid bridge's outline.

Phase extraction and phase unwrapping are the central issues in the development of ESPI as summarized in detail by Huntley (2001). It is in general impossible to make distinction between positive and negative displacements from a single pair of specklegrams, the problem inherent to any interferometric techniques. A remedy is the use of phase shifting, with which a series of predetermined phase shifts, either in temporal domain or in spatial domain, are added to the speckle field to be measured. A variety of techniques based either on temporal phase shifting (e.g., Nakadate and Saito 1985, Creath 1985) or on spatial phase shifting (e.g., Takeda 1990) have been proposed to date. As the phase extraction from such phase-shifted interferograms is usually made modulo 2π, the analysis should be followed by phase unwrapping, which is to resolve 2π ambiguity, to recover complete phase information. Obviously, a drawback of the phase-shifting techniques is their need for special hardware calibrated to give certain phase shifts, such as piezoelectric translators or diffraction gratings, to provide predetermined phase shifts to the speckle field to be measured. Another drawback in temporal phase shifting is that the target to be measured must be quasi-stationary during phase shifts being added, the requirement hardly accepted in the measurement of dynamic phenomena.

For measurement of dynamic displacement (or deformation), a new technique called temporal speckle pattern interferometry (TSPI) is proposed recently. This technique is based on the analysis of time-varying intensity of each speckle caused by continuous displacement of the surface. The intensity of speckle at an imaging sensor, $I\ (x,\ y,\ t)$, can be expressed as (e.g., Jones and Wykes 1983)

$$I(x,y,t) = I_b(x,y) + I_m(x,y)\cos\varphi(x,y,t) \tag{1}$$

where $I_b\ (x,\ y)$ and $I_m\ (x,\ y)$ are respectively the background and modulation intensities of specklegram at a position of $(x,\ y)$ on the imaging sensor, and $\varphi\ (x,\ y,\ t)$ is the phase of intensity variation at an instant of t. It is assumed here that both I_b and I_m vary with time very slowly and thus they are regarded constant within the duration considered. When the displacement is unidirectional one (i.e., only either in positive or in negative direction), the intensity variation appears as a sinusoidal curve whose frequency is related to the rate of displacement. Joenathan et al. (1998) used a temporal Fourier analysis to extract phase information from such sinusoidally varying intensities to measure large deformations of more than 100μm. Hilbert transform can also be applied for phase analysis of such dynamic ESPI signal as Madjarova et al. (2003) presented. Li et al. (2001) proposed a new method, called time sequence phase method (TSPM), which analyzes time-varying speckle intensities to retrieve unwrapped phase information directly. They demonstrated that the proposed method was applicable to a continuous, unidirectional displacement of the test surface. Li and Tao (2002) extended this technique in order to measure surface vibrations. The extension is based on the detection of recurvature points (RPs), which appear in the time-varying speckle intensity at instants when the vibrating surface changes its direction of displacement. For the validation of their technique, Li and Tao chose an edge-clamped circular plate vibrating in a sinusoidal waveform at 0.1838Hz in frequency. As mentioned in their paper, this simplicity of vibration presented little difficulty in the detection of RPs in the validation measurement. Furthermore, Li et al. (2002) applied their TSPM successfully to the measurement of large deflection of thin films, demonstrating that the measurement of deflection of about 1400μm was possible with sensitivity of $\lambda/2$ or $\lambda/4$, where λ is the wavelength of the illumination beam used.

In this report, we report a TSPI technique for measuring micron-order dynamic displacement of deformable liquid free surface in quasi-cylindrical form as shown above. We have chosen an optical setup similar to that proposed by Verga et al. (1998) to make measurement of liquid surfaces. As shown later, a ground glass is placed at the image plane of an object lens. While Verga et al. used a fringe analysis for phase extraction, we have adopted TSPM proposed originally by Li et al. (2001) because it has a potential of providing more spatially resolved information of displacement than the fringe analysis. Since dynamic displacements of liquid free surface should exhibit much more complicated features, such as those due to multiple modes, frequency harmonics, phase variations and so on, than the vibrating circular plate targeted by Li and Tao (2002), we have developed an automated and robust algorithm for detecting RPs from a set of consecutively acquired specklegrams. The algorithm is verified through a series of computer simulations using artificially generated specklegrams. The developed system and procedures are tested through a serial of measurements of dynamic surface displacement of both a flat mirror and a cylindrical glass rod, the latter providing a simplified model of the liquid bridge. Comparison data are taken with the laser focusing displacement meter (LFDM), which is commercially available for displacement measurement at a single point on the surface of little deformation. It is shown that time-varying displacements of those test surfaces measured with the developed TSPI system are in good agreement with those measured with the LFDM. The capability of the present technique is demonstrated by some experimental results taken from dynamic surface displacement of a liquid bridge of silicone oil.

1.2 Principle

This section gives a description of the principle of the present TSPI technique. Since the principle of ESPI is well documented in some previous literature (e.g., Jones and Wykes 1983 and Rastogi et al. 2001), it will not be repeated here.

Figure 2 shows a schematic of the present optical setup. The coherent laser beam is divided into reference and object beams by the polarizing beam splitter (PBS). It has about 95% reflectance for s-polarized component and 92% transmittance for p-polarized component. It is designed here that the s-polarized component serves as an object beam. The role of the λ/2 plate placed before the PBS is to rotate the polarization plane of the laser beam impinging on the PBS, thus to change the intensity ratio between s- and p-polarized components. The polarization direction of the object beam is rotated by π/2 when passing twice through the λ/4 plate inserted between the PBS and the object surface. This rotation results in 92% transmittance through the PBS when the object beam is in propagation toward the object lens, thus enabling the maximum use of laser beam intensity. This is important when the reflectance of the object surface is quite low as in the case of liquid surface. Both object and reference beams are recombined at the PBS and then imaged, by the object lens, onto the smooth-side surface of the ground glass. The rough-side surface of the ground glass is viewed by a CCD element through the camera lens. A polarizing filter is placed in front of the camera lens in order to accept only object and reference beams with the same polarization. As documented by Kihm (1997) and Ko et al. (2001), the use of ground glass is common in speckle photography for measurement of refractive index gradients. Joenathan and Torroba (1991) used a ground glass in their ESPI system to make displacement measurements insensitive to the angle of reference beam.

In the present setup, the complex amplitudes of the object and reference beams incident on a CCD array at (x, y) are given as,

$$A_\mathrm{O}(x,y) = a_\mathrm{O}(x,y)\exp\left\{i\left[\varphi_\mathrm{O}(x,y)+\varphi_\mathrm{GO}(x,y)\right]\right\}, \tag{2}$$

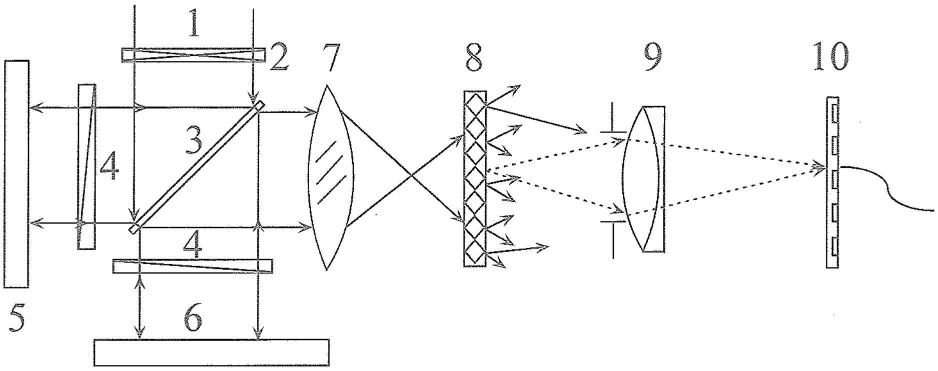

Fig. 2 Schematic of the present optical setup: 1, coherent laser beam; 2, λ/2 plate; 3, polarizing beam splitter; 4, λ/4 plate; 5, object surface; 6, reference surface; 7, object lens; 8, ground glass; 9, polarizing filter; 10, CCD camera's lens; 11, CCD element.

$$A_{\mathrm{R}}(x,y) = a_{\mathrm{R}}(x,y)\exp\left\{i\left[\varphi_{\mathrm{R}}(x,y) + \varphi_{\mathrm{GR}}(x,y)\right]\right\}, \tag{3}$$

where a_{O} and a_{R} are the amplitudes, φ_{O} and φ_{R} are the phases due to surface shapes, and φ_{GO} and are φ_{GR} the random phases introduced by the ground glass. Here subscripts O and R denote object and reference, respectively. The irradiance as a result of interference between the object and the reference beams is given by:

$$I_{\mathrm{F}} = |a_{\mathrm{O}}|^2 + |a_{\mathrm{R}}|^2 + 2|a_{\mathrm{O}}|\cdot|a_{\mathrm{R}}|\cos[\varphi_{\mathrm{F}}], \tag{4}$$

where $\varphi_{\mathrm{F}} = \varphi_{\mathrm{O}} - \varphi_{\mathrm{R}} + \varphi_{\mathrm{GO}} - \varphi_{\mathrm{GR}}$ with (x, y) omitted for simplicity. This irradiance will generate speckles due to random phase modulation from $\varphi_{\mathrm{GO}} - \varphi_{\mathrm{GR}}$.

Any displacement of the object surface will result in the change of path length in the object beam. It is postulated here that the amount of displacement is so small that the object surface after displacement is relayed to the same position, within the resolution of each CCD array, on the ground glass. The change of path length is, therefore, determined by the change in the path between the object surface and the ground glass as follows:

$$A'_{\mathrm{O}}(x,y) = a_{\mathrm{O}}(x,y)\exp\left\{i\left[\varphi_{\mathrm{O}}(x,y) - \Delta\varphi(x,y,t) + \varphi_{\mathrm{GO}}(x,y)\right]\right\}, \tag{5}$$

where $\Delta\varphi\ (x, y, t)$ is the time-dependent phase change induced by the dynamic displacement of the object surface. Note that positive $\Delta\varphi$ corresponds to the displacement toward the CCD camera. The irradiance after the displacement then becomes

$$I'_{\mathrm{F}} = |a_{\mathrm{O}}|^2 + |a_{\mathrm{R}}|^2 + 2|a_{\mathrm{O}}|\cdot|a_{\mathrm{R}}|\cos[\varphi_{\mathrm{F}} - \Delta\varphi]. \tag{6}$$

Equations. (1), (4) and (6) lead to the following relations:

$$I_{\mathrm{b}}\left(x,y\right)=\left|a_{\mathrm{O}}\left(x,y\right)\right|^{2}+\left|a_{\mathrm{R}}\left(x,y\right)\right|^{2}, \tag{7a}$$

$$I_{\mathrm{m}}\left(x,y\right)=2\left|a_{\mathrm{O}}\left(x,y\right)\right|\cdot\left|a_{\mathrm{R}}\left(x,y\right)\right|,\ \text{and} \tag{7b}$$

$$\varphi\left(x,y,t\right)=\varphi_{\mathrm{F}}\left(x,y\right)-\Delta\varphi\left(x,y,t\right). \tag{7c}$$

According to Wykes (1982), the phase change is related to the displacement of the object surface as follows:

$$\Delta\varphi=\frac{2\pi}{\lambda}\left(\overrightarrow{n_{\mathrm{O}}}-\overrightarrow{n_{\mathrm{S}}}\right)\cdot\vec{d}, \tag{8}$$

where $\overrightarrow{n_{\mathrm{O}}}$ and $\overrightarrow{n_{\mathrm{S}}}$ are respectively the direction cosines of the object beam and the reflected beam, $\vec{d}$ the displacement vector and λ the wavelength of the object beam. If the object surface is flat and illuminated normally by a planar wave front as in the present setup, Eq. (8) is simplified to

$$\Delta\varphi=\frac{4\pi}{\lambda}\left|\vec{d}\right|. \tag{9}$$

It should be noted that the angle between $\overrightarrow{n_{\mathrm{O}}}-\overrightarrow{n_{\mathrm{S}}}$ and $\vec{d}$ could vary if there is surface curvature as in liquid bridges. Such angle variation should be taken into account for accurate displacement measurement of curved surfaces.

Figure 3 shows an example of specklegram of a moving flat mirror surface taken at an instant, $t=t_0$. The

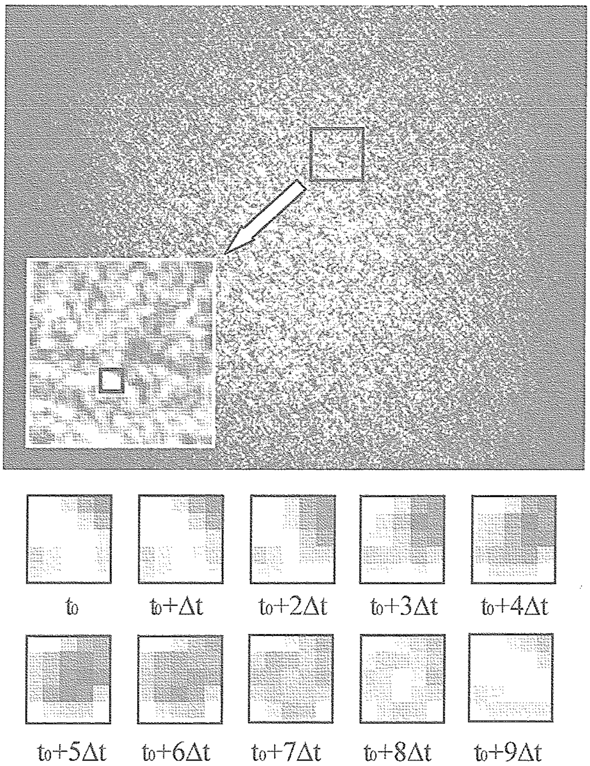

Fig. 3 An example of specklegram (only an area of 100×120 pixels shown) and time-varying intensity in a box marked (time interval Δt=1/60s).

details of image acquisition are described later in this paper. The local speckle intensities in the box marked vary with time as a result of dynamic surface displacement. Such a variation of speckle intensity (or gray level) at a pixel is illustrated in Fig. 4, where the displacement here is unidirectional one. The gray level varies periodically with time (or frame number) in accordance with Eqs.(6) and (7), thus generating a wrapped signal varying between $I_{\min}$ and $I_{\max}$.

1.3 Phase extraction

1.3.1 Time sequence phase method

The time sequence phase method (TSPM) proposed by Li et al. (2001) consists of evaluation of wrapped phase and subsequent phase unwrapping.

The method for phase evaluation in TSPM is basically the same as those used in other scanning phase methods (e.g., Vikhagen 1990, Wang and Grant 1995, Saldner et al. 1996, Carlsson and Wei 2000). From Eq. (1), the wrapped phase is evaluated modulo π as follows:

$$\varphi(x,y,t)=\cos^{-1}\left\{\frac{2I(x,y,t)-I_{\max}(x,y)-I_{\min}(x,y)}{I_{\max}(x,y)-I_{\min}(x,y)}\right\} \tag{10}$$

where $I_{\max}(x, y) = I_b(x, y) + I_m(x, y)$ and $I_{\min}(x, y) = I_b(x, y) + I_m(x, y)$. It is assumed that sequential specklegrams for a sufficiently long duration are available so as to permit evaluation of $I_{\max}$ and $I_{\min}$ from time-varying intensity at each (x, y).

As the value of φ determined from Eq. (10) is in the range of $[0, \pi]$, it must be unwrapped by considering appropriate integer multiple of π. The time-sequence analysis proposed by Li et al. (2001) carries out this unwrapping directly by examining three consecutive speckle intensities, $I(x, y, t_i - \Delta t)$, $I(x, y, t_i)$ and $I(x, y, t_i - \Delta t)$, acquired at a constant time interval, Δt. As shown in Fig. 4, those three consecutive speckle intensities are used to judge whether the intensity of interest, $I(x, y, t_i)$, lies on a downward branch or on an upward branch of the intensity variation. The phase is unwrapped as $\varphi_{uwp} = 2n\pi + \varphi(t_i)$ if the intensity is on the downward branch and as $\varphi_{uwp} = 2(n+1)\pi - \varphi(t_i)$ if it is on the upward branch, where n is the total number of cycles counted from the

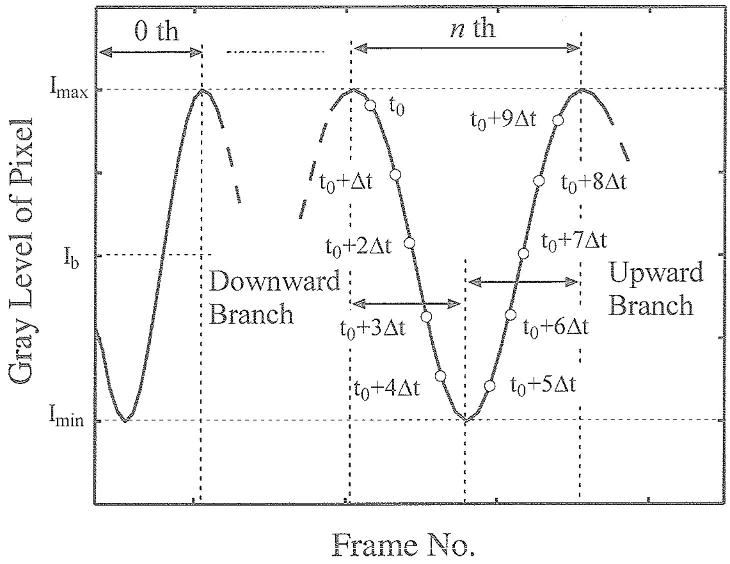

Fig. 4 Wrapped signal of speckle intensity corresponding to unidirectional displacement.

start of the measurement. The analysis relies on the condition that the recording speed is high enough to resolve at least five-six specklegrams in one cycle of intensity variation. Low-pass filtering is applied to remove intensity noises.

1.3.2 Detection of recurvature points

The time sequence analysis mentioned in the previous section is unable to distinguish positive displacement from negative displacement. Li and Tao (2002) improved this limitation in order to make measurement of surface vibrations with periodic change of displacement direction. Their improvement is based on the detection of RPs that appear in the intensity signal at instants when the surface displacement changes its direction. Li and Tao verified the proposed technique by measuring a circular plate vibrating with a single mode at a single frequency. However, their choice of such a simple vibrating displacement requires no elaborated algorithm for RP detection, and in fact they did not present any particular algorithms. However, in the measurement of dynamic displacement of liquid surface, an automated and reliable detection of RPs is needed because liquid free surfaces may exhibit complex modes of dynamic displacement.

In principle, RPs can be detected as local extrema in the intensity variation observed at each (x, y) as illustrated in Figs. 5(a) and 5(b), where the phase value of a simple oscillatory displacement is depicted in Fig. 5(a) and the corresponding gray-level variation is shown in Fig. 5(b). Two RPs appear in Fig. 5(b) at each instant when the dynamic deformation changes its direction. These RPs can be detected by means of numerical differentiation of the intensity variations. However, if their intensities are close to $I_{\max}$ or $I_{\min}$ as in the first RP in Fig. 5(b), they are not distinguishable from other local extrema corresponding to $I_{\max}$ or $I_{\min}$. To deal with this problem, a new algorithm for RP detection is developed here. It is based on the assumption that the deformation

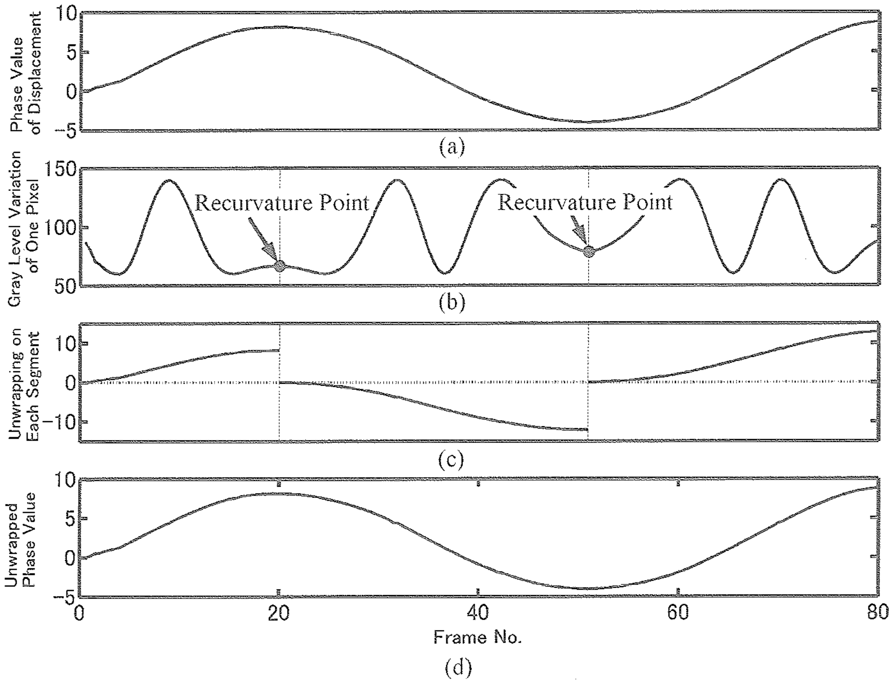

Fig. 5 Illustration of unwrapping procedures dealing with recurvature points: (a) time-varying phase value of displacement at a pixel; (b) corresponding gray-level variation showing two recurvature points; (c) segments of unwrapped phase value; (d) recovered phase value of deformation.

of liquid surface has a wavelength much longer than the average space between speckles. This assumption is reasonable in many cases of liquid surface deformation and allows us to expect simultaneous occurrence of RPs in neighboring speckles. This assumption is exploited as follows. Firstly, all extrema are detected from intensity variations of all effective pixels in the sequential specklegrams, where 'effective pixels' refer to those having modulation intensity higher than a prescribed threshold value denoted by I_{thresh}. Our experience shows that an average modulation intensity calculated from all pixels in the specklegrams can be used as I_{thresh}. To remove noises in the signals of intensity variation, the zero-phase digital filtering (Gustafsson 1996) is used. Secondly, a spatial window of $N_s \times N_s$ pixels in size is defined around an effective pixel of interest. Also a temporal window of $\pm \mathrm{N}_f$ in frame number is defined around the instant considered to detect the extremum in the intensity variation of the pixel considered. This temporal window is to deal with possible phase jitter due to the noise present in the intensity signal. These spatial and temporal windows constitute a domain for the check of simultaneous detection of RPs in neighboring pixels. Lastly, the number of all extrema existing in this domain is counted. The number of extrema is denoted by N_e and the number of effective pixels in this spatial window is denoted by N_p. If $N_e / N_p \geq \alpha$, the extremum is registered as RP and otherwise as non-RP. Here, α is called the threshold for number ratio in this paper. The effect of the values of α, N_s and N_f on the detection of RPs will be discussed by means of numerical simulation in the next section.

Once all RPs are detected successfully, the change of direction of dynamic surface deformation is determined. That information is used for piece-wise phase unwrapping with the method described in the previous section as illustrated in Fig. 5(c). Finally, an overall phase unwrapping is completed by connecting the segments into a single curve as in Fig. 5(d). It should be mentioned that we still have no information about the initial direction of phase change, which must be determined separately. Carlsson and Wei (2000) proposed a method for determining the initial direction of phase change, which is based on the knowledge of the phase of neighboring pixels.

1.3.3 Computer simulations

The proposed algorithm for PR detection is verified through a series of computer simulations using artificially generated specklegrams. Subjective speckle fields are generated by using the method described by Kolenovic et al. (1999) in a simple configuration consisting of a rough surface, an imaging lens and a CCD element. A laser beam 532nm in wavelength illuminates the rough surface, where the mean roughness height of 10μm is assumed. The size of the illuminated area is $1.5 \times 1.5\mathrm{mm}^2$. The distance between the rough surface and the lens is 166.7mm. The lens has a focal length of 100mm and an aperture radius of 2.5mm. All these parameters are comparable to those of the present measurement system. The effect of reference beam is taken into account as a constant phase term added to the subjective speckle fields calculated. Random noises with root-mean-square intensity of 5 are added to the specklegrams generated, where each specklegram has an intensity ranging from 0 to 255 (8bits).

A series of three hundred specklegrams are generated from a rough surface with an assumed dynamic displacement as depicted in Fig. 6. The displacement ranges from 0 to 1.69μm, having a change of direction at 175 in frame number. The figure includes the generated specklegrams at some representative frame numbers. In the present computer simulation, the parameters in the algorithm, α, N_s and N_f are varied systematically to see their effect on the performance of the detection of RPs.

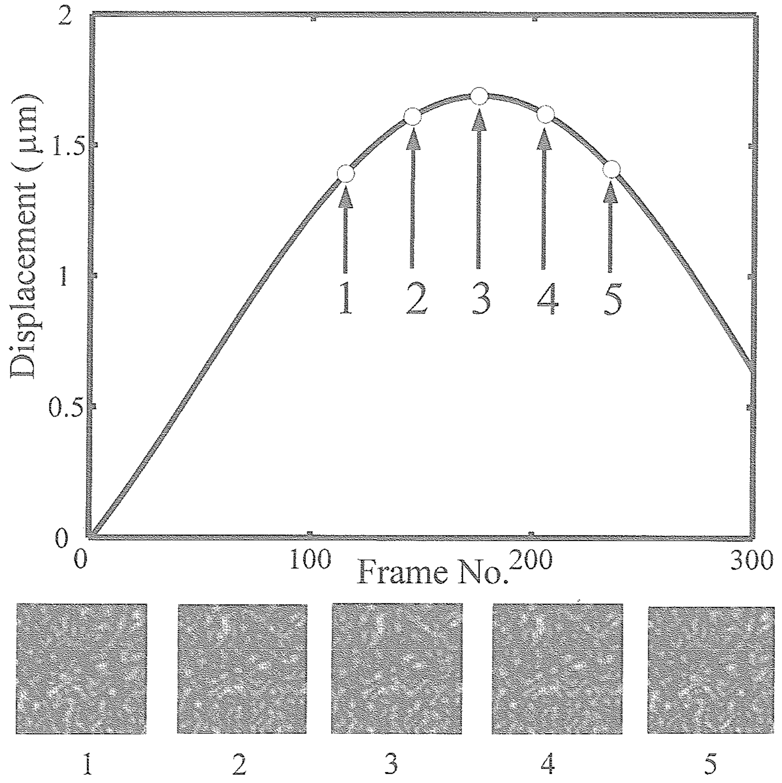

Fig. 6 Simulated displacement with a single change of displacement direction and artificially generated specklegrams at instants marked in the figure.

Figure 7(a) shows the success ratio of RP detection as function of α for different values of N_s and N_f, where the success ratio is defined as a ratio of the number of effective pixels with RP detected successfully to the total

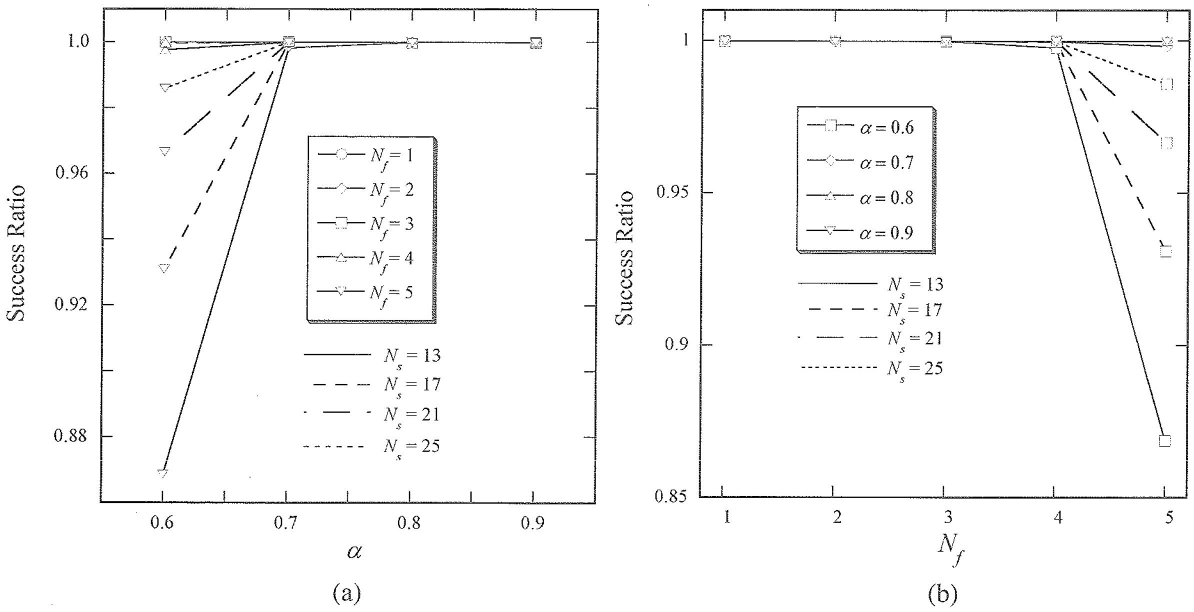

Fig. 7 Results of computer simulation: (a) effect of the threshold for number ratio, α, on the success ratio in the detection of recurvature points, (b) effect of the width of temporal window, N_f, on the success ratio in the detection of recurvature points.

number of effective pixels. Note that every effective pixel has a single RP in this simulation. The success ratio is satisfactorily high for α>0.7. Actually, it is 0.998 for α=0.8-0.9 regardless of the values of N_s and N_f. When α becomes smaller than 0.7, the success ratio starts to decrease, particularly for $N_f = 5$, with showing lower values for smaller N_s. Figure 7(b) plots the success ratio as function of N_f, showing considerable deteriorations at $N_f = 5$ and α=0.6. When N_f is large and N_s is small, the number of speckles observed in the spatial window can be small and consequently the local extrema corresponding to I_{max} or I_{min} within the domain (i.e., within the spatial and temporal windows) can happen to be in phase with each other. This will result in a spurious detection of RPs in the present algorithm. The results presented here suggest that (1) α should be larger than 0.6, (2) N_s should be as large as possible within requirement for the spatial resolution of the measurement, and (3) N_f should not exceed 5, particularly if smaller value of α is used (say, α=0.6-0.7).

1.4 Verification experiments

1.4.1 Experimental setup

Figure 8 shows the layout of the present experimental system. A liquid bridge is formed in the gap between the upper and lower disks, both 5mm in diameter. In verification experiment, a glass rod of the same diameter is placed at the same position. A flat mirror provides the reference surface. The illumination is given by a diode pumped solid state laser that delivers a coherent TEM_{00} beam with an output power of 60mW and with wavelength of 532nm. The CW beam is divided into the reference beam and the object beam by the polarizing beam splitter after going through a $\lambda/2$ plate and a beam shaping lens. The beam shaping lens is an achromat lens with a focal length of 140mm and has a function of adjusting the angle of incidence on the object surface. The object lens placed between the object surface and the $\lambda/4$ plate is an aspherical lens with a focal length of 39mm and a diameter of 60mm. The selection of such an object lens with short focal length and large diameter is to maximize the size of measurement area by illuminating the cylindrical surface with an object beam of large

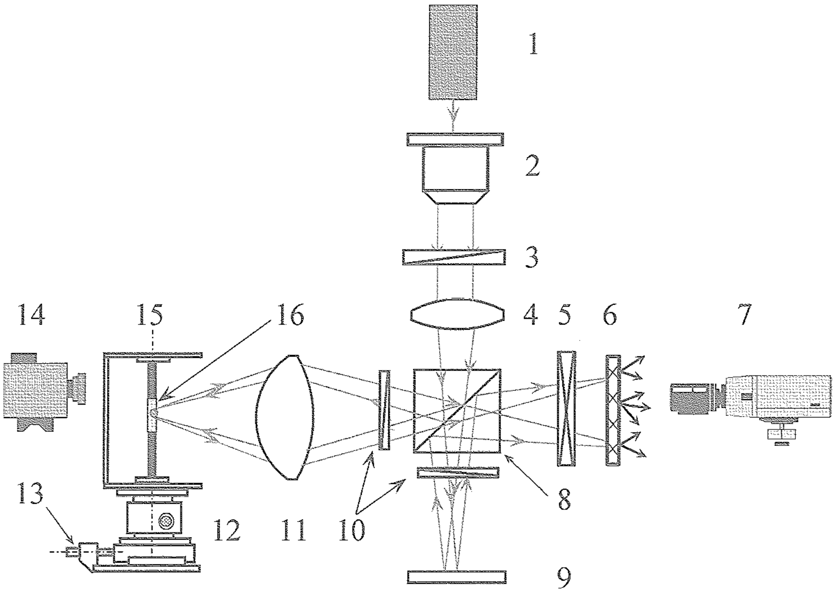

Fig. 8 Layout of the present experimental system: 1, laser; 2, beam expander; 3, $\lambda/2$ plate; 4, beam shaping lens; 5, polarizing filter; 6, ground glass; 7, CCD camera; 8, polarizing beam splitter ; 9, reference surface (flat mirror); 10, $\lambda/4$ plate; 11, object lens; 12, supporting stage; 13, PZT; 14, laser-focusing displacement meter; 15, main frame of liquid bridge; 16, cylindrical object surface (of glass rod or liquid bridge).

converging angle. In fact, if the illuminating beam were nearly collimated as in typical ESPI, the light reflected by the cylindrical liquid surface would become diverging and thus weakened, resulting in a very limited size of the measurement area. The measurement area achieved in the present setup is $0.7\times0.6\mathrm{mm}^2$ of 5mm diameter cylindrical surface, which is quite satisfactory for the study of dynamic surface behaviors due to unsteady thermocapillary convection in the liquid bridge. The distance from the object lens to the object surface is adjusted to have a magnified image on the smooth-side surface of the ground glass.

A high speed B&W CCD camera with 512×480 pixels is used to image speckles generated at the rough-side surface of the ground glass. The camera is equipped with a telecentric lens having focal length of 55mm. A frame grabber with 512MB memory is used to capture specklegrams at 250fps for about 8 seconds consecutively.

In the present experiment, a piezoelectric translator (PZT) is installed in the liquid bridge apparatus to generate dynamic surface displacement in the out-of-plane direction. Its amplitude and frequency are controlled with a signal generator interfaced with a PZT driver. Since the amplitude and the frequency of the dynamic surface behaviors induced by the unsteady thermocapillary convection of interest are typically 1μm and 1Hz, respectively, they are set to 0.4-1.5μm in amplitude and 1-2Hz in frequency here.

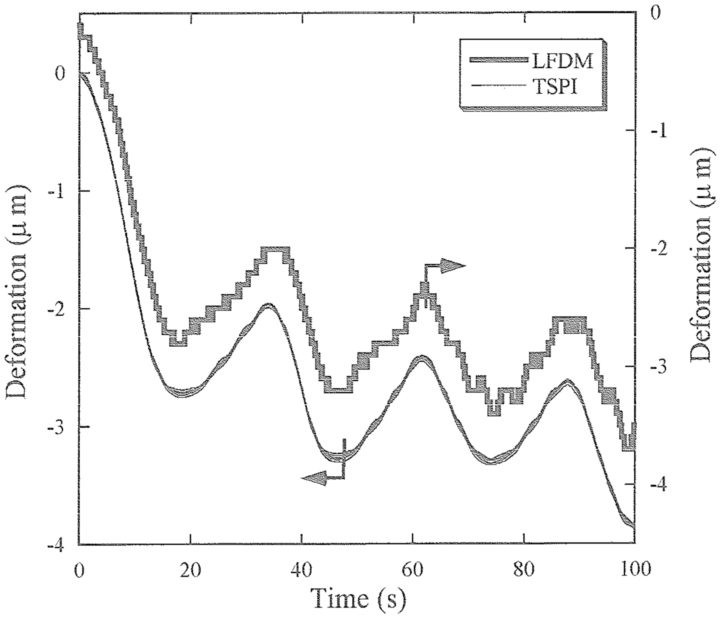

Fig. 9 Comparison of dynamic displacement of a flat mirror measured with the present TSPI and the LFDM.

The intensity ratio between the reference and object beams must be adjusted carefully to make the modulation intensity, I_m, as high as possible. The adjustment can be done efficiently by activating the PZT to move the object surface back and forth. At first the modulation intensity is estimated by directly looking at local intensity variations on a TV monitor during motion of the object surface, and this information is used to optimize the beam intensity ratio by rotating the λ/2 plate. The final adjustment is made by recording several sets of specklegrams with slightly different beam intensity ratio and by evaluating modulation intensity for each setting.

The LFDM is used simultaneously to measure the displacement for comparison. It emits a laser beam that is focused on the surface as a spot 2 μm in diameter and measures out-of-plane displacement with a resolution of 0.1μm. The LFDM is placed behind the object surface to measure the displacement of its backside.

1.4.2 Flat mirror surface

The first verification is done by measuring slowly moving surface of a flat mirror. In this experiment, the aspherical object lens is not used but the beam shaping lens is placed between the PBS and the ground glass as an object lens. A series of 3000 specklegrams are taken at 30fps in each run of measurement. Out-of-plane displacement is given by heating and cooling of a micrometer head of the supporting stage, instead of using the PZT. It should be mentioned that the CW laser used for this preliminary experiment is not the one used currently (output energy of 60mW) but the one used for long and thus with lower effective output energy (25mW). This should be the reason for comparatively worse (but still satisfactory) results from the flat mirror surface than those from the glass rod described in the next section.

Figure 9 presents the result taken under the heating/cooling sequence. It begins with cooling and thus with negative displacement. This information is used to avoid the ambiguity in the initial direction of displacement.

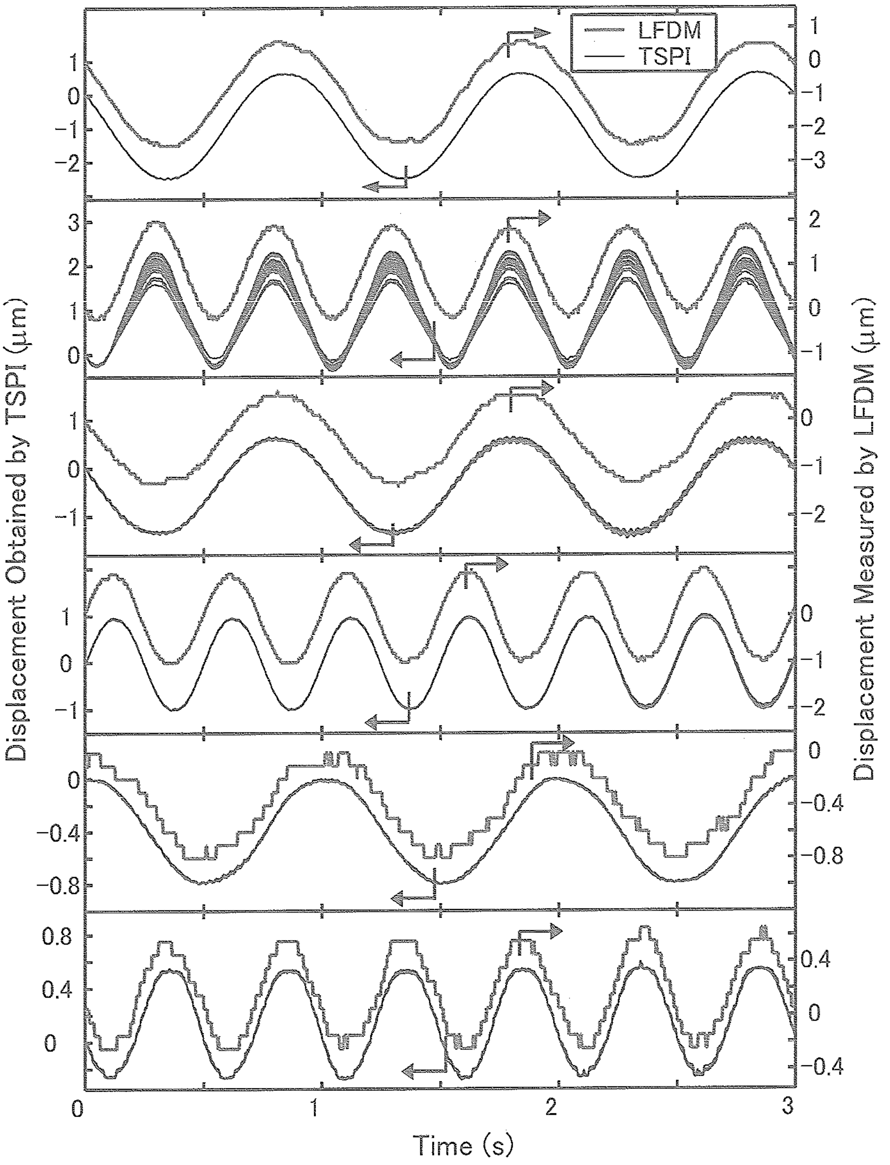

Fig. 10 Comparisons of dynamic displacements of a glass rod measured with the present TSPI and the LFDM: (a) case A, (b) case B, (c) case C, (d) case D, (e) case E, (f) case F.

The values of 0.8, 21 and 3 are used for α, N_s and N_f, respectively, in the RP detection algorithm, according to the simulation results described in Section 3.3. The data taken with the present TSPI system are indicated by thin lines and compared with the result taken with the LFDM indicated by a thick line. Note that the LFDM provides only a single point measurement while the TSPI provides measurements of all effective pixels, the number of which is about 111,000 in the present setup. The figure includes the TSPI data taken at 30 locations chosen arbitrarily from all effective pixels measured. As seen here, the agreement between TSPI and LFDM data is good for the whole heating/cooling sequence. Their difference defined as standard deviation is 0.12μm. Since this value includes measurement errors of LFDM, the standard deviation within the TSPI data is evaluated and it is 0.10μm.

Table 1 Evaluation of measurement results of glass rod surface.

	Case A	Case B	Case C	Case D	Case E	Case F
Amplitude (μm)	1.65	1.1	1.0	1.0	0.4	0.45
Frequency (Hz)	1.00	2.00	1.00	2.00	1.00	2.00
Error (μm)	0.075	0.180	0.085	0.089	0.039	0.038
Standard deviation (μm)	0.015	0.137	0.017	0.009	0.003	0.003

1.4.3 Glass rod

A glass rod made of BK7, 5mm both in diameter in length, is used for the measurement. The setup described in Section 4.1 is used to achieve the size of measurement area of 0.7×0.6mm^2. Figures 10(a)-(f) present comparison between the LFDM and the present TSPI for different oscillatory displacement conditions (i.e., amplitude and frequency) as summarized in Table 1. Those displacements are given by the PZT. A series of about 1000 specklegrams are captured continuously at 250fps for each measurement. Initial direction of displacement is determined from the data taken by the LFDM. The values of 0.8 and 21 are used respectively for α and N_s for all cases, while the values of N_f are 3 for Cases A to D and 5 for Cases E and F. Each figure includes TSPI data from 40 effective pixels randomly selected from the whole specklegram, where the modulation intensity of 25 is used to define the effective pixels. In the present experiments, the ratio of the effective pixels to the total pixels is always higher than 70%. The standard deviations between the TSPI data and the LFDM data are given in Table 1. They are well below 0.1μm except for Case B. The standard deviations within the TSPI data are also listed in the table. They are less than 0.02μm except for Case B. The reason for appreciably deteriorated (but still very satisfactory) result for Case B should be the instability of the laser that happens very occasionally.

The displacement is calculated from the unwrapped phase value through Eq. (9), which is simplified from Eq. (8) with neglecting the effect of surface curvature. This simplification is checked in Fig. 11, where the displacements measured at a total of 69 effective pixels located on diagonal lines crossing the whole FOV are plotted. It is obvious that there are no distinguishable discrepancies among the measurements. This indicates that the influence of the surface curvature can be neglected in the present measurement. This preferred feature is because the directional change of surface normal in the measurement area (0.7×0.6mm^2) is very small and it causes negligible effect on the displacement measurement (actually, the deviation is estimated to be less than 1%).

All the results shown in this section demonstrate well the validity and the accuracy of the present TSPI technique when applied to the measurement of dynamic displacement of cylindrical glass surface.

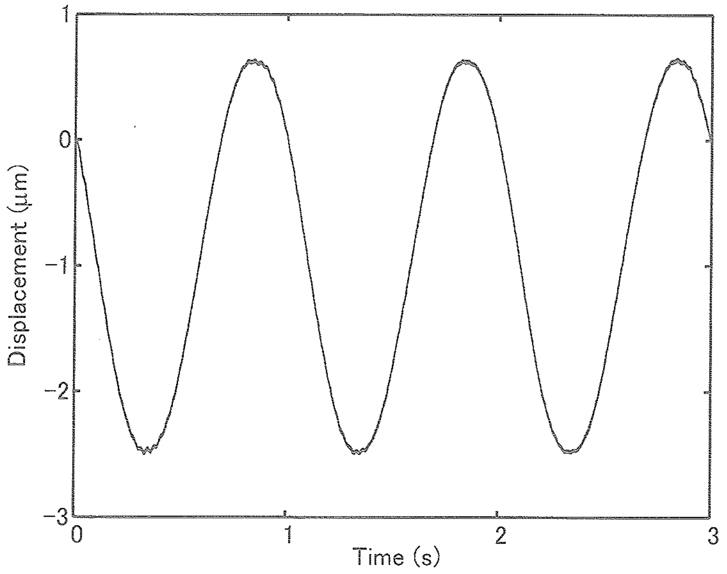

Fig. 11 Displacements of pixels on diagonal lines crossing the whole FOV of Case A.

Table 2 Evaluation of measurement results of liquid bridge surface.

	Case A	Case B	Case C	Case D
Amplitude (μm)	1.55	1.05	1.05	0.5
Frequency (Hz)	1.00	1.00	2.00	2.00
Error (μm)	0.162	0.138	0.152	0.073
Standard deviation (μm)	0.012	0.004	0.037	0.015

1.4.4 Liquid bridge

Four runs of measurement with different displacement amplitudes and frequencies are conducted as summarized in Table 2. The object lens is looking at the area near the upper disk. The size of the measurement area is 0.7×0.6mm^2 as before. The oscillatory displacement is given by the PZT and the comparison data is taken with the LFDM. Note that the frequency of displacement is low enough to guarantee that the whole liquid bridge is translated with the same amplitude. The values of the parameters for detecting RPs are α = 0.8 and N_s = 21 for all cases, and N_f = 3 for Cases A to C while N_f = 5 for Cases D. The result for Case B is shown in Fig. 12(a) in the form of a three-dimensional surface plot of measured displacement. As far as we know, this is the first displacement measurement of two-dimensional surface area of liquid bridge.

Comparison with the LFDM for Case B is shown in Fig. 12(b). The standard deviation between TSPI and LFDM is 0.138μm, while that within the TSPI data is only 0.004μm. Agreement between the present TSPI and the LFDM is still satisfactory as in the case of the glass rod except that standard deviations between the TSPI data and the LFDM data are higher. It is reasonable since the object surface is a free liquid surface instead of a solid surface. Not shown here, the results for Cases A, C and D are similarly good and well compared with those measured with LFDM, as one can recognize from the values of standard deviation in Table 2.

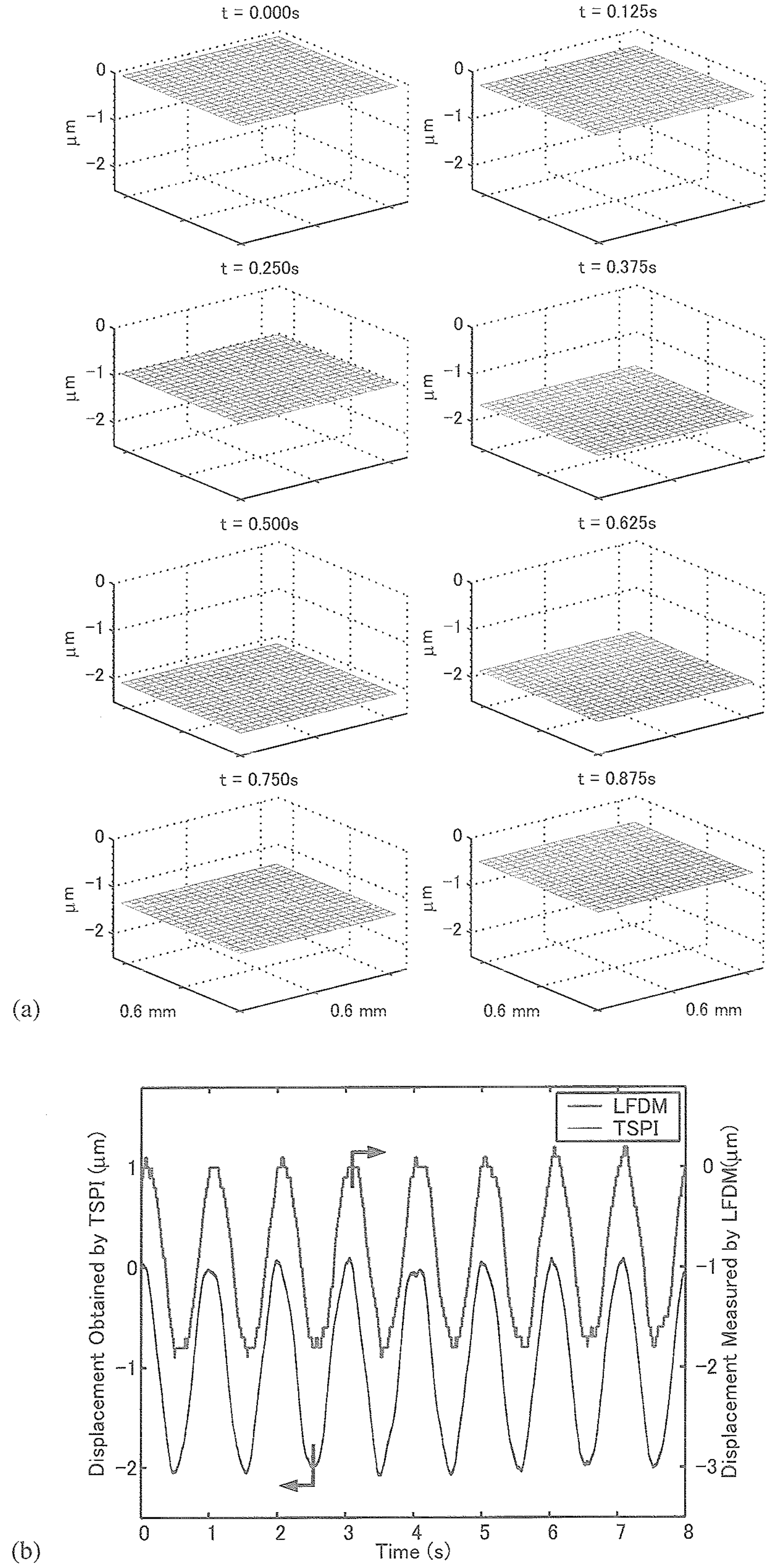

Fig. 12 Dynamic displacements of liquid bridge's surface measured with TSPI and LFDM:
(a) three-dimensional surface plots of displacement within the first second, and
(b) comparison of displacements obtained by TSPI and the LFDM.

1.5 Conclusions of Chapter 1

This chapter presents a technique based on temporal speckle pattern interferometry (TSPI), a recently developed version of electronic speckle pattern interferometry, for measuring micron-order surface motions of quasi-cylindrical liquid bridge. The time sequence phase method (TSPM) proposed recently has been extended to develop automated and robust procedures for phase unwrapping of time-varying speckle intensities generated from moving surfaces. The performance of the developed procedures is evaluated through a series of computer simulations made in a range of parameters involved. The technique is implemented into a TSPI system utilizing a ground glass for generating speckles from non-speckled reference and object wave fronts. Validity and accuracy of the technique are verified by the displacement measurement of oscillating surfaces of a flat mirror and a glass rod, where the detailed comparisons are made with a commercially available instrument for single-point displacement measurement. It is demonstrated that the present method is well applicable to the two-dimensional dynamic displacement measurement of a deformable surface of an actual liquid bridge.

2. Effect of G-jitter on the Measurement of DSD

2.1 Introduction

A liquid bridge suspended between two coaxial disks differentially heated is typical flow geometry for the investigation of flow instability of thermocapillary convection. When the temperature difference between the disks is small, a laminar state with an axisymmetric toroidal flow pattern appears in the liquid bridge. When the temperature difference is increased to exceed a certain critical value, ΔT_c, the flow and temperature fields start to oscillate. This onset of oscillation has been an extensive research target in theoretical, numerical and experimental work. High Prandtl number fluids, such as silicone oil, are usually used in the experiment.

Some recent studies (e.g., Kamotani et al. 2001) suggest that DSD of the liquid bridge of high Prandtl number fluid, particularly that near the hot disk, should play an important role in the transition mechanisms. This suggestion is based upon the experimental finding that the transition conditions for a wide range of liquid-bridge size are correlated well with a non-dimensional parameter representing "deformability" of the liquid bridge surface. The finding, however, seems to be in contrast with the assumption made in the past theoretical

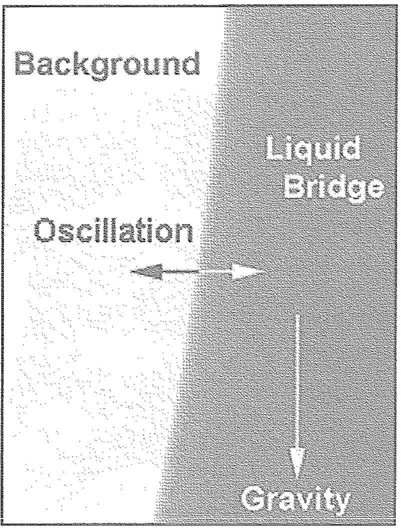

Fig. 13 Image of the edge of the liquid bridge seen in micro-imaging displacement meter (MIDM).

and numerical work, both based upon the governing equation neglecting the contribution of DSD. To clarify this issue, a microgravity experiment was proposed in response to the International Announcement of Opportunity in 2000 for microgravity experiments to be conducted in ISS. The proposal is now under consideration as a candidate for experiments to be conducted in the Fluid Physics Experiment Facility (FPEF) under development by JAXA.

In this proposed experiment, DSD of a liquid bridge will be measured with a microscopic imaging technique. As the DSD measurement can be influenced by g-jitter in ISS, the effect must be well examined. The present paper reports some results of the examination made in artificially generated g-jitter in the ground experiment. It is shown that a simple g-jitter table driven by a piezoelectric actuator can realize g-fluctuations of realistic magnitude in an adequate range of frequencies. It is also shown that the DSD component associated with the oscillatory state in the liquid bridge can clearly be distinguished, by means of appropriate filtering, from original DSD signals contaminated by the effect of g-jitter. This second result indicates the feasibility of DSD measurement in the proposed microgravity experiment in ISS.

2.2 Method

2.2.1 Micro-imaging displacement meter (MIDM)

A new technique for measuring dynamic surface deformation of liquid bridge is used here. It is based upon microscopic imaging of oscillatory motions of the edge of the liquid bridge illuminated by back lighting. A

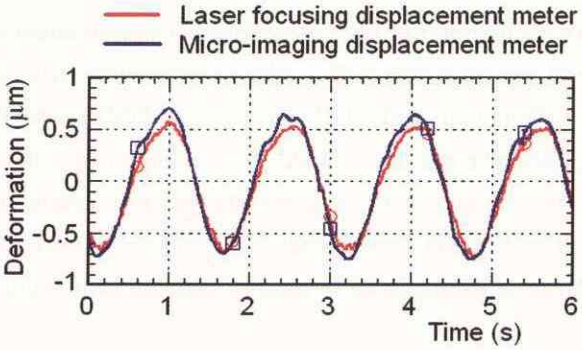

Fig. 14 Comparison of DSD measurement between the present MIDM and the laser focusing displacement meter (LFDM).

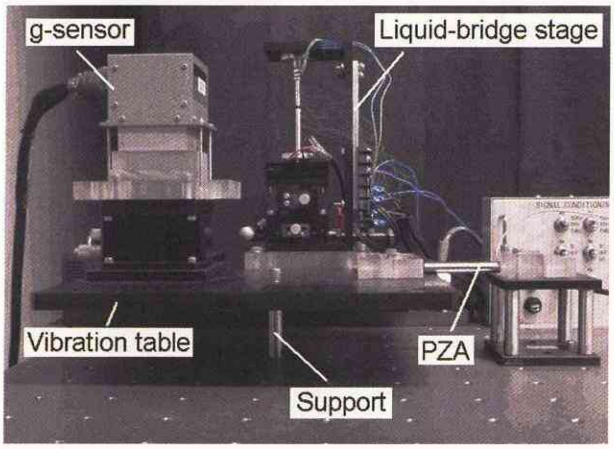

Fig. 15 Photo of the present vibration table driven by the piezoelectric actuator (PZA).

similar technique was used by Cao et al. (1991) and Yao et al. (1996), who, however, reported few details on the technique. The present technique, referred to as micro-imaging displacement meter (MIDM), consists of a black&white CCD camera (640×480 pixel) equipped with a microscope objective (Mitutoyo M Plan Apo 20×), a Xenon light source with a fiber light guide, and a frame grabber with 1 GB memory capacity. The microscope objective is characterized by its long working distance (30.5mm). The field of view is 410μm×325μm, giving a cell resolution of 0.65μm/pixel. As shown in Fig. 13, the liquid bridge taken with the camera appears as a black area in the white background. The DSD is observed as back-and-forth motion in horizontal direction in the image.

To detect the position of the edge of the liquid bridge, the edge-detection algorithm developed by Nishino et al. (2000) is implemented into the present MIDM. The edge detection is done along every horizontal line crossing the interface between the liquid bridge and the background. Averaging over eleven horizontal lines is taken to improve S/N of the detection. This leads the effective resolution of MIDM to become better than 0.1μm. Its temporal resolution is limited to 60fps presently by the framing speed of the camera. Figure 14 shows the comparison of DSD measurement between the present MIDM and the laser focusing displacement meter (LFDM). The latter is a commercially available instrument to measure DSD at a single spot (0.2μm) with a resolution of 0.1μm and it is applicable only to the liquid surface of little deformation. The agreement between MIDM and LFDM is quite satisfactory as recognized in this comparison. Further details of MIDM will be reported elsewhere.

2.2.2 G-jitter simulator

To generate g-jitter of realistic magnitude and frequency spectra in the ground experiment, a vibration table driven by a piezoelectric actuator (PZA) is constructed. The layout is shown in Fig. 15. The table is supported by a single metal rod. A liquid-bridge stage, a g-sensor and a CCD camera with a microscope objective (not shown here) are mounted on the table. The lowest resonance frequency of the table having those loads is measured to be about 170Hz, presenting no problem in the current g-jitter simulation conducted under 100Hz. The g-sensor has a resolution of 1μg and placed at the same height with the liquid bridge. The PZA used here achieves the maximum force of 800N and the maximum deformation of 60μg. It is capable of generating horizontal g-jitter of 15mg at 5Hz oscillation on the table.

The operation of the PZA is controlled by an analogue voltage supplier interfaced with a computer. A feedback control system using g-sensor signals is to be constructed to reproduce any desired frequency spectra of g-jitters on the vibration stage. In the present experiment, the g-jitter signal available at the web site of Principal Investigator Microgravity Services (PIMS) are used to determine the voltage given to the PZA. To do so, the g-jitter signal are integrated twice to obtain displacement signal that is then fed into the PZA by means of analogue voltage. Figure 16 shows the amplitude spectra of g-jitter from PIMS data and that generated and measured on the vibration table. Obviously, the generated g-jitter is different from PIMS data because of the non-linear property of the PZA used. Since the purpose of the present study is not to reproduce g-jitter identical to the PIMS data but to generate g-jitter with realistic amplitude and frequency spectra, the currently generated g-jitter is used to investigate their effect on DSD measurement. It should be mentioned that any frequency components of DSD higher than 30Hz are measured as lower frequency components as a result of aliasing in the present MIDM whose temporal resolution is 60Hz. This must be considered carefully in the interpretation of DSD measured.

2.2.3 Liquid bridge

A liquid bridge of silicone oil (5cSt) is suspended between two coaxial disks heated differentially. The upper disk is heated while the lower one is cooled to minimize the effect of buoyancy. The disk diameter, D, is 5mm, and the length of the liquid bridge, L, is 2.5mm, thus giving the aspect ratio of 0.5. The disk temperature is measured with thermocouples imbedded in the disks. The surface temperature of the liquid bridge is monitored with a fine thermocouple (25μm in diameter) placed near to but not in contact with the surface. The onset of oscillation is detected by the temperature signal from this thermocouple together with the DSD observed with naked eyes. The critical temperature difference, ΔT_c, is from 30 to 38K, depending on the ambient temperature. Yukawa et al. (2002) reported that a pulsating oscillation of 1.20Hz first appears and it then changes to a rotating oscillation of 0.95Hz at a slightly higher ΔT for the present conditions of liquid bridge. During DSD measurement, ΔT is kept constant to achieve a quasi-steady state of oscillation. The measurement of DSD is done at the middle height of the liquid bridge. Image acquisition is done for about 5s continuously.

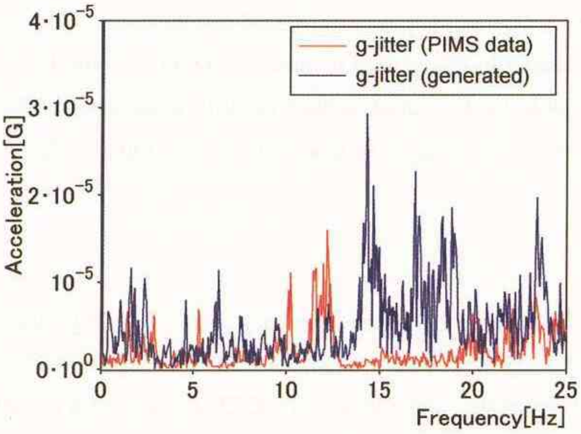

Fig. 16 Amplitude spectra of g-jitter from PIMS data and that generated and measured on the vibration stage.

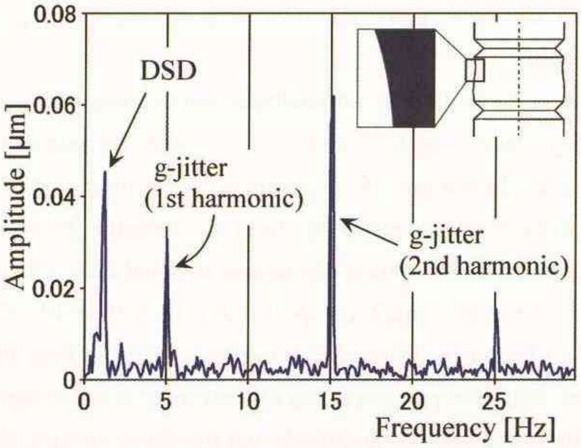

Fig. 17 Amplitude spectrum of DSD in the presence of harmonic g-jitter whose fundamental frequency is 5Hz.

2.3 Results and discussion

2.3.1 Harmonic g-jitter

The present experiment has begun with the imposition of harmonic g-jitter on the liquid bridge. Such harmonic g-jitters are generated by supplying sinusoidal voltage variations to the PZA. Sanz and Diez (1989) evaluated resonance frequencies of liquid bridge of inviscid fluid under the condition of no gravitational force. Their evaluation would predict resonance frequencies of 20.0, 7.3-11.5, 10.4-13.6, and 16.7Hz for modes of liquid-bridge oscillation for $(m, n)=(0,2)$, $(1,1)$, $(2,1)$ and $(3,1)$, respectively, where m and n are the azimuthal and axial modes of oscillation. It is found that the liquid bridge in the present experiment has a sensitive resonance frequency of about 15Hz, which might be corresponding to the one for $(m, n)=(2,1)$ or $(3,1)$ above. At this resonance frequency, the liquid bridge exhibits large DSD whose amplitude is much larger than that of natural DSD caused by the oscillatory state in the liquid bridge. However, the DSD components can be well discriminated in the plot of frequency spectrum as shown in Fig. 17. This result is obtained in the presence of harmonic g-jitter whose fundamental frequency is 5Hz. Since the g-jitter generated here has roughly triangular wave form rather than sinusoidal one, the odd multiples of the fundamental frequency appear as

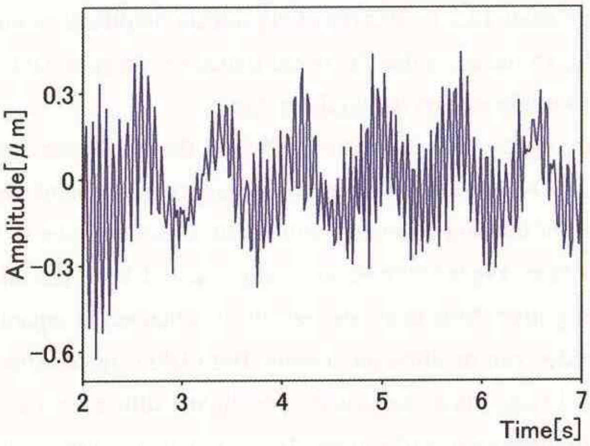

Fig. 18 DSD signal measured in the presence of non-harmonic g-jitters generated at ΔT=39K.

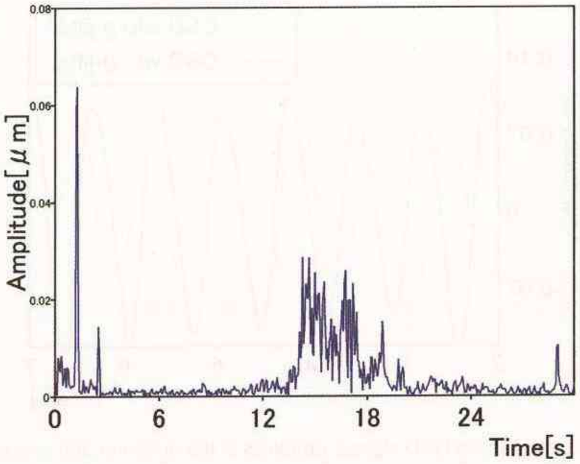

Fig. 19 DSD signal measured in the presence of non-harmonic g-jitters generated at ΔT=39K.

higher harmonics. It is seen in Fig. 17 that the natural DSD at about 1Hz is clearly recognized in the amplitude spectrum and it is well separated from other components of DSD generated by the g-jitter. This suggests that the natural DSD component can be discriminated from those due to g-jitter if their frequencies are not overlapping. Recently, Kawaji (2003) studied the effect of g-jitter on the liquid bridge of middle *Pr* fluid (acetone) to find their negligible effect on the onset of oscillation.

2.3.2 Non-harmonic g-jitter

DSD measurements are done in the presence of non-harmonic g-jitter of amplitude spectra as shown in Fig. 16. This condition should provide more realistic case for future ISS experiment. Figure 18 shows the DSD signal measured in the presence of non-harmonic g-jitter. Note that the liquid bridge is in the sate of oscillation (ΔT=39K), thus exhibiting an oscillatory DSD at about 1Hz. The DSD signal also exhibits the components of higher frequencies due to g-jitter. In particular, the component of about 15Hz, which should be corresponding to the resonance frequency of the liquid bridge mentioned above, has a dominating amplitude. The amplitude spectrum of DSD measured is plotted in Fig. 19. It is seen that there are two sharp peaks at 1.25 and 2.5Hz, which should be corresponding to the natural DSD frequency and its second harmonics, respectively. There is another broad frequency range from 13.5 to 20.5Hz of significant amplitude. Comparison with the amplitude spectra of g-jitter shown in Fig. 16 indicates that the broad frequency range in DSD seen in Fig. 19 is likely due to the significant power of g-jitter imposed on the liquid bridge.

The results shown so far suggest that the natural DSD in the oscillatory state of the liquid bridge can be well separated from the DSD caused by g-jitters by an appropriate band-pass filtering of DSD signals measured. Although the choice of filtering frequency will be an important issue in the actual ISS experiment, it is determined to be 0.8-2.0Hz here. Figure 20 presents comparison of band-pass filtered DSD signals obtained in the absence and presence of g-jitter. Note that these results are obtained in separate experiments and therefore the conditions of the liquid bridge can be different slightly. Both DSD signals show nearly the same amplitude even though it is smaller than 0.1μm. Their frequencies are slightly different; it is about 0.75Hz in the absence of g-jitter while it is 0.85Hz in the presence of g-jitter. This difference can be attributed to the difference in the liquid-bridge conditions.

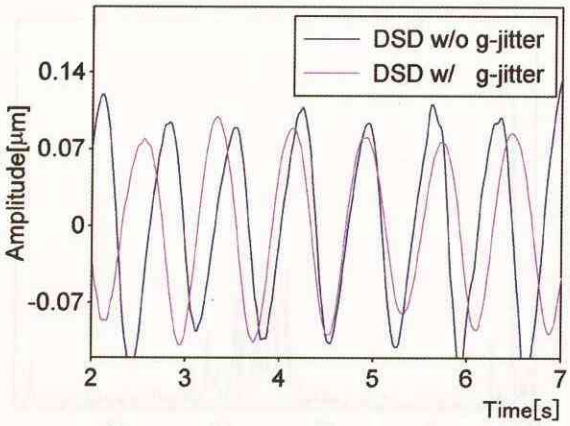

Fig. 20 Band-pass filtered DSD signals obtained in the absence and presence of g-jitter.

2.4 Conclusions of Chapter 2

Effects of g-jitter on the measurement of dynamic surface deformations (DSD) caused by the oscillatory thermocapillary convection in a liquid bridge have been studied experimentally. A vibration table driven by a piezoelectric actuator is constructed to generate g-jitters of realistic amplitude and frequency spectra. A micro-imaging displacement meter is used to measure DSD in the presence of g-jitter. It is shown that the natural DSD in the oscillatory state of thermocapillary convection is well separated in the frequency domain from that caused by harmonic and non-harmonic g-jitters. It is concluded that the DSD measurement in the future ISS experiment is feasible even in the presence of g-jitter there.

References

Cao, Z. H., You, X. T., Tang, Z. M. & Hu, W. R., 1001, Experimental investigation of thermocapillary convection in half floating zone, Advances in Space Research, Vol. 11, No. 7, p. 229.

Carlsson, T. E. & Wei, A., 2000, Phase evaluation of speckle patterns during continuous deformation by use of phase-shifting speckle interferometry, Applied Optics, Vol. 39, pp. 2628-2637.

Creath, K., 1985, Phase-shifting speckle interferometry, Applied Optics, Vol. 24, pp. 305-358.

Gustafsson, F., 1996, Determining the initial states in forward-backward filtering IEEE Transactions on Signal Processing, Vol. 44, No. 4, pp. 988-992.

Huntley, J. M., 2001, Automated analysis of speckle interferograms, *in* Digital Speckle Pattern Interferometry and Related Techniques, Rastogi, P. K. ed., Wiley, New York, pp. 59-139.

Joenathan, C., Franzec B., Haible, P. & Tiziani, H. J., 1998, Speckle interferometry with temporal phase evaluation for measuring large-object deformation, Applied Optics, Vol. 37, pp. 2608-2614.

Joenathan, C. & Torrba, R., 1991, Modified electronic speckle pattern interferometer employing an off-axis reference beam, Applied Optics, Vol. 30, pp. 1169-1171.

Jones, R. & Wykes, C., 1989, Holographic and speckle interferometry (2nd edition), Cambridge University Press.

Kamotani, Y. & Ostrach, S., 1998, Theoretical analysis of thermocapillary flow in cylindrical columns of high Prandtl number fluids, Transactions of the ASME, Journal of Heat Transfer, Vol. 120, pp. 758-764.

Kamotani, Y., Wang, L., Hatta, S., Bhunia, P. & Yoda, S., 2001, Study of oscillatory thermocapillary flow of high Prandtl number fluid, NASDA Technical Memorandum, NASDA-TMR-010015E, pp. 25-42.

Kawaji, M., 2003, private communication.

Kihm, K. D., 1997, Laser speckle photography technique applied for heat and mass transfer problem, Advances in Heat Transfer, Vol. 30, pp. 255-311.

Ko, H. S., Okamoto, K. & Madarame, H., 2001, Reconstruction of transient three-dimensional density distributions using digital speckle tomography, Measurement Science and Technology, Vol. 12, No. 8, pp. 1219-1226.

Kolenovic, E., Osten, W. & Jüptner, W., 1999, Non-linear speckle phase changes in the image plane caused by out of plane displacement, Optics Communications, Vol. 171, pp. 333-344.

Li, X., Tao, G. & Yang, Y., 2001, Continual deformation analysis with scanning phase method and time sequence phase method in temporal speckle pattern interferometry, Optics & Laser Technology, Vol. 33, 53-59.

Li, X., Soh, A.-K., Deng, B. & Guo, X., 2002, High-precision large deflection measurements of thin films using time sequence speckle pattern interferometry, Measurement Science and Technology, Vol. 13, No. 8, pp. 1304-1310.

Li, X. & Tao, G., 2002, Low-frequency harmonic vibration analysis with temporal speckle interferometry, Optics & Laser Technology, Vol. 34, pp. 259-264.

Madajarova, V. D., Kadano, H. & Toyooka, S., 2003, Dynamic electronic speckle pattern interferometry (DESPI) phase analyses with temporal Hilbert transformation, Optics Experss., Vol. 11, No. 6, pp. 617-623.

Nakadate, S. & Saito, H., 1985, Fringe scanning speckle-pattern interferometry, Applied Optics, Vol. 24, pp. 2172-2180.

Nishino, K., Kato, H. & Torii, K, 2000, Stereo imaging for simultaneous measurement of size and velocity of particles in dispersed two-phase flow, Measurement Science and Technology, Vol. 11, pp. 633-645.

Rastogi, P. K., 2001, Digital speckle pattern interferometry and related techniques, John Wiley & Sons, Ltd.

Roussev, I., Partalin, T., Toshev, E., Choulev, A. & Koulev, P., 1999, Digital speckle-metrology local investigation of sedimentation and surface effects in liquids, SPIE 3825, pp. 174-185.

Saldner, H. O., Molin, N. E. & Stetson, K. A., 1996, Fourier-transform evaluation of phase data in spatially phase-biased TV holograms, Applied Optics, Vol. 35, pp. 332-336.

Sanz, A. & Diez, J. L., 1989, Non-axisymmetric oscillations of liquid bridges, Vol. 205 , p. 503.

Takeda, M., 1990, Spatial-carrier fringe-pattern analysis and its applications to precision interferometry and profilometry: an overview, Ind. Metrology, Vol. 1, pp. 79-99.

Van der Auweraer, H., Steinbichler, H., Vanlanduit, S., Haberstok, C., Freymann, R., Storer, D. & Linet, V., 2002, Application of stroboscopic and pulsed-laser electronic speckle pattern interferometry (ESPI) to modal analysis problems, Measurement Science and Technology, Vol. 13, No. 4, pp. 451-463.

Verga, A., Baglioni, P., Dupont, O., Dewandel, J.-L., Beuselinck, T. & Bouwen, J., 1998, Use of electronic speckle pattern interferometers for the analysis of convective states of liquid in weightlessness, Optical Engineering, Vol. 37, No. 7, pp. 2161-2174.

Vikhagen, E., 1990, Nondestructive testing by use of TV holography and deformation phase gradient calculation, Applied Optics, Vol. 29, pp. 137-144.

Wang, J. & Grant, I., 1995, Electronic speckle interferometry, phase-mapping, and nondestructive testing techniques applied to real-time, thermal loading, Applied Optics, Vol. 34, pp. 3620-3627.

Wykes, C., 1982, Use of electronic speckle pattern interferometry (ESPI) in the measurement of static and dynamic surface displacements, Optical Engineering, Vol. 21, pp. 400-406.

Yao, Y. L., Liu, F. & Hu, W. R, 1996, How to determine critical Marangoni number in half floating zone convection, International Journal of Heat and Mass Transfer, Vol. 39, No. 12, p. 2539.

Yukawa, M., Nishino, K. & Torii, K., 2002, Mode structures of oscillatory Marangoni convection in a liquid bridge, CD-ROM Proceedings of the Tenth International Symposium on Flow Visualization, Paper F0330, Kyoto, Japan.

Numerical Simulation of Marangoni Convection in Consideration of Free Surface Displacement

By
Takanori Hashimoto[1], Yukifumi Kousaka[1], Ichiro Ueno[1], Hiroshi Kawamura[1]
and Shinichi Yoda[2]

Abstract: Thermocapillary-driven convection in a half-zone liquid bridge has been extensively examined. A large number of researches have been conducted concerning the transition of the flow field. Physical mechanism of the transition, however, has not been fully understood. In the present study, three-dimensional numerical simulations taking with and without dynamic free surface deformation (DSD) into account are carried out to evaluate the effect of the surface deformation upon the flow field. The surface shape is solved by considering the stress balance on the free surface, and the calculation coordinate is reconstructed at every time step with employing a boundary fitted coordinate. The test fluids are acetone (Pr=4.38) and 2cSt silicone oil (Pr=28.11). The free surface deformation is determined primarily by the pressure variation. For acetone, the effect of the DSD upon critical point and flow field was quite small in the range of present numerical simulation in previous report. In this report, the effect of DSD for 2cSt silicone oil is obtained.

1. INTRODUCTION

One of the purposes of the space environment utilization is the processing of a new material, because the buoyancy effect can be reduced in the space environment. Floating-zone method is one of the well-known material processing methods under the micro-gravity. In this method, however, the convection, still occurs induced by the surface tension difference on the free surface owing to the temperature gradient. This convection is called thermocapillary or Marangoni convection and has been widely investigated with a half-zone (HZ) model corresponding to half part of floating-zone model. In the HZ model, a liquid bridge is sustained between the coaxial cylindrical rods. Each rod is maintained at different temperature, thus the liquid bridge is exposed by a temperature difference ΔT between the both rods. When ΔT exceeds a critical value ΔTc, the induced flow in the HZ bridge of medium and high Prandtl number fluid exhibit a transition from a two-dimensional steady flow to a three-dimensional oscillatory one. The oscillatory flow has two patterns called as 'Standing wave' and 'Traveling wave'. These flows appear depending upon the temperature difference. The structure in the liquid bridge is characterized further by the azimuthal wave number m. The flow field is divided azimuthally into 2×m sectors; the alternate sector, m in total, consists of the same thermal-fluid structure.

The experiments for the thermocapillary convection have been widely conducted. Preisser et al. (1983) [1] investigated the oscillatory flow to study the effect of several parameters such as the aspect ratio and Marangoni number. Velten et al. (1991) [2] observed the periodic instability of thermocapillary convection in the cylindrical liquid bridge.

---

[1]Tokyo University of Science, 2641 Yamazaki, Noda-shi, Chiba 278-8510, Japan
[2]JAXA, 2-1-1 Sengen, Tsukuba City, 305-8505,Japan

As for the numerical simulation, Kuhlmann (1993)[3], Wanschura et al. (1995)[4] calculated the critical Reynolds number for the various non-dimensional numbers (Bi, Gr, Pr, A) using the linear stability analysis. Savino and Monti (1996) [5] simulated the oscillatory flow numerically and compared it with their experiments. Shevtsova et al. (1998) [6] studied the transition from two dimensional thermoconvective steady flow to a time-dependent flow considered for an axisymmetric liquid bridge of a high Prandtl number fluid (Pr = 105) with a static curved free surface.

It should be noted that most of the existing numerical simulations were conducted without considering the dynamic free surface movement. After the onset of oscillation, however, the pressure field fluctuates violently because of the unsteady flow. Therefore the free surface is expected to dynamically deform due to these fluctuation. In fact, the free surface vibration in the liquid bridge has been observed in some terrestrial experiments. Kamotani et al. (2000) [7] reported an experiment of the thermocapillary convection performed aboard the Spacelab in an open cylindrical container, and investigated the free surface movement. In addition, they analyzed the influence of surface deformation upon the critical condition in the half-zone configuration. Correlation between the criticality and the dynamic surface deformation, however, is not understood yet. An influence of surface vibration upon the flow field instability must be evaluated to understand the mechanism of the oscillatory flow. To the authors' knowledge, no numerical work has been done on the thermocapillary convection in a liquid bridge with including the dynamic deformation of the surface.

Recently, Kuhlmann et al. [8] have made a combined analytical and numerical study on the thermocapillary convection in a liquid bridge with including the DSD using the linear stability analysis. They analyzed the mutual relation between the flow field and the dynamic surface deformation of the most dangerous mode. The present study aims at understanding time-dependent thermal-fluid phenomena with dynamic free surface deformation in the half-zone liquid bridge by a direct nonlinear numerical simulation.

2. NOMENCLATURES

Γ	aspect ratio
D	diameter
g	gravity
h	heat transfer coefficient
H	height of the liquid bridge
I	unit matrix
J	Jacobian
m	azimuthal wave number
n	surface-normal vector
N	normalizing dominator
P	pressure
$r,\ \theta,\ z$	coordinates
$\xi,\ \zeta,\ \eta$	coordinates in the computational domain
$R,\ R_k$	position of the free surface
R_0	radius of the disk
$R_{1,2}$	main radii of curvature
S	stress tensor
t	time
T	temperature
T_0	reference temperature
U_0	maximum velocity
$V_{r,\theta,z},\ V_{x,y}$	velocities
v_i	compensated temporally velocity
v_i	temporally velocity
V	volume of the liquid bridge
$V_{\xi,\zeta,\eta}$	contravariant velocities
$V_{\xi,\zeta,\eta}$	temporally contravariant velocities
α	contact angle
β	thermal expansion coefficient
ΔT	temperature difference between the disks
δs	amount of free surface deformation
τ	time in the computational domain
$\sigma,\ \sigma(T)$	surface tension
$\sigma_0(T_0)$	reference surface tension
σ_T	thermal coefficient of surface tension
κ	thermal diffusivity
λ	thermal conductivity
μ	dynamic viscosity
ν	kinematic viscosity
ρ	density
Bi	Biot number
Bo	Bond number
Ca	Capillary number
Gr	Grashof number
Ma	Marangoni number
Pr	Prandtl number
Re	Reynolds number

3. NUMERICAL METHOD

The purpose of this study is to analyze the influence of the free surface deformation upon the thermocapillary flow. Therefore, a numerical method to capture the temporally varying surface motion is employed. The deformed surface is expressed using the boundary fitted coordinate (BFC).

To consider the thermocapillary convection in a liquid bridge, a configuration of the analysis is defined as shown in Fig. 1. The liquid bridge with volume V_0 is sustained by two rigid parallel disks of equal radii $r = R_0$ located at $z = 0$ and H. The temperature difference between these disks is defined by ΔT.

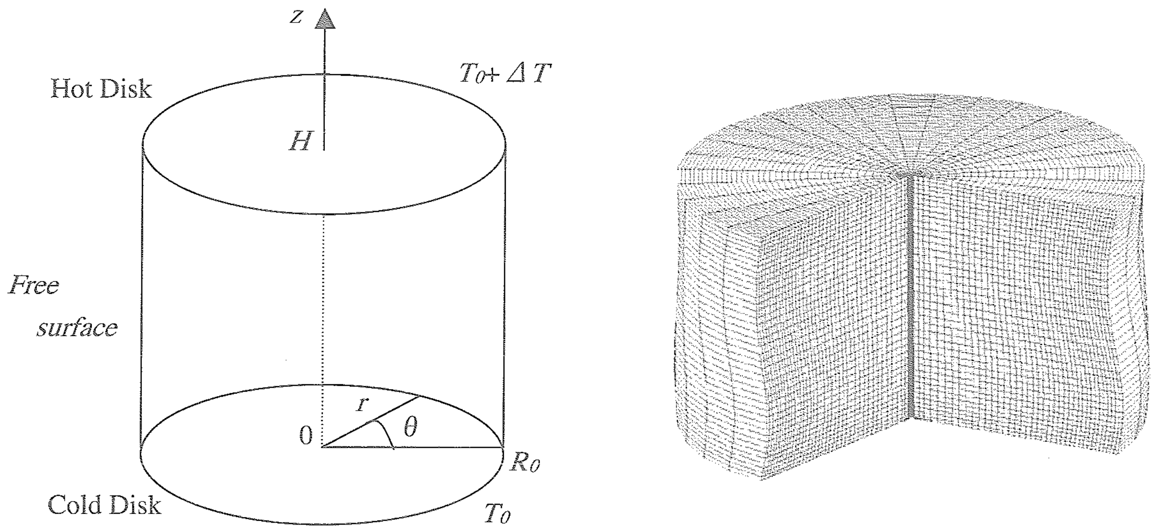

Figure 1: Numerical configuration

3.1 Governing equations

The liquid is assumed to be an incompressible Newtonian fluid of kinematic viscosity ν and density ρ. In a cylindrical coordinates system, the continuity, the Navier-Stokes and the energy equations are given by

$$\nabla \cdot \mathbf{u} = 0 \tag{1}$$

$$\frac{\partial \mathbf{u}}{\partial t} + \left(\mathbf{u} \cdot \nabla\right)\mathbf{u} = -\nabla P + \frac{Pr}{Ma}\nabla^2 \mathbf{u} \tag{2}$$

$$\frac{\partial T}{\partial t} + (\mathbf{u} \cdot \nabla)T = \frac{1}{Ma}\nabla^2 T \tag{3}$$

Variables are non-dimensionalized using scales as Table 1.

Table 1: Scales used for non-dimensionalization

Variable	r, z	t	$v = (v_r, v_\theta, v_z)$	p	T
Scale	H	$H\mu / \sigma_T \Delta T$	$\sigma_T \Delta T / \rho$	$\rho(\sigma_T \Delta T / \mu)^2$	ΔT

The non-dimensional numbers are defined by

$$Re = \frac{U_0 H}{\nu}$$

$$Pr = \frac{\nu}{\kappa}$$

$$Ma = \frac{1}{\mu\kappa}\left|\frac{\partial\sigma}{\partial T}\right|\Delta T \cdot H$$

3.2 Boundary fitted coordinate

The shape of the liquid bridge is deformed dynamically in this calculation. Therefore, the adequate coordinate system must be employed to calculate the flow field with the finite difference method. The boundary fitted coordinate method is applied to the governing equations in all directions. In the previous study, the computational domain was assumed to be cubic. The substantial error arises in the conversion from the cylinder in the physical domain to the cubic in the computational one. Thus, the present computational domain is modified to cylindrical coordinate. Equations (1)-(3) can be transformed from the physical domain to the computational domain by Jacobian matrix.

$$\begin{bmatrix} \frac{\partial}{\partial t} \\ \frac{\partial}{\partial r} \\ \frac{\partial}{\partial \theta} \\ \frac{\partial}{\partial z} \end{bmatrix} = \begin{bmatrix} 1 & \xi_t & \zeta_t & \eta_t \\ 0 & \xi_r & \zeta_r & \eta_r \\ 0 & \xi_\theta & \zeta_\theta & \eta_\theta \\ 0 & \xi_z & \zeta_z & \eta_z \end{bmatrix} \begin{bmatrix} \frac{\partial}{\partial \tau} \\ \frac{\partial}{\partial \xi} \\ \frac{\partial}{\partial \zeta} \\ \frac{\partial}{\partial \eta} \end{bmatrix} \tag{4}$$

$$\begin{bmatrix} \frac{\partial}{\partial \tau} \\ \frac{\partial}{\partial \xi} \\ \frac{\partial}{\partial \zeta} \\ \frac{\partial}{\partial \eta} \end{bmatrix} = \begin{bmatrix} 1 & r_\tau & \theta_\tau & z_\tau \\ 0 & r_\xi & \theta_\xi & z_\xi \\ 0 & r_\zeta & \theta_\zeta & z_\zeta \\ 0 & r_\eta & \theta_\eta & z_\eta \end{bmatrix} \begin{bmatrix} \frac{\partial}{\partial t} \\ \frac{\partial}{\partial r} \\ \frac{\partial}{\partial \theta} \\ \frac{\partial}{\partial z} \end{bmatrix} \tag{5}$$

Equation (5) is inversely transformed as follows,

$$\begin{bmatrix} \dfrac{\partial}{\partial t} \\ \dfrac{\partial}{\partial r} \\ \dfrac{1}{r}\dfrac{\partial}{\partial \theta} \\ \dfrac{\partial}{\partial z} \end{bmatrix} = \frac{1}{J} \begin{bmatrix} A_{11} & A_{12} & A_{13} & A_{14} \\ A_{21} & A_{22} & A_{23} & A_{24} \\ A_{31} & A_{32} & A_{33} & A_{34} \\ A_{41} & A_{42} & A_{43} & A_{44} \end{bmatrix} \begin{bmatrix} \dfrac{\partial}{\partial \tau} \\ \dfrac{\partial}{\partial \xi} \\ \dfrac{1}{\xi}\dfrac{\partial}{\partial \zeta} \\ \dfrac{\partial}{\partial \eta} \end{bmatrix} \tag{6}$$

where,

$$A_{11} = \frac{r}{\xi}\left(r_\xi \theta_\zeta z_\eta + r_\zeta \theta_\eta z_\xi + r_\eta \theta_\xi z_\zeta - r_\eta \theta_\zeta z_\xi - r_\zeta \theta_\xi z_\eta - r_\xi \theta_\eta z_\zeta\right),$$

$$A_{12} = -\frac{r}{\xi}\left(r_\tau \theta_\zeta z_\eta + r_\zeta \theta_\eta z_\tau + r_\eta \theta_\tau z_\zeta - r_\eta \theta_\zeta z_\tau - r_\zeta \theta_\tau z_\eta - r_\tau \theta_\eta z_\zeta\right),$$

$$A_{13} = r\left(r_\tau \theta_\xi z_\eta + r_\xi \theta_\eta z_\tau + r_\eta \theta_\tau z_\xi - r_\eta \theta_\xi z_\tau - r_\xi \theta_\tau z_\eta - r_\tau \theta_\eta z_\xi\right),$$

$$A_{14} = -\frac{r}{\xi}\left(r_\tau \theta_\xi z_\zeta + r_\xi \theta_\zeta z_\tau + r_\zeta \theta_\tau z_\xi - r_\zeta \theta_\xi z_\tau - r_\xi \theta_\tau z_\zeta - r_\tau \theta_\zeta z_\xi\right),$$

$$A_{21} = 0 \quad A_{22} = \frac{r}{\xi}\left(\theta_\zeta z_\eta - \theta_\eta z_\zeta\right), \quad A_{23} = -r\left(\theta_\xi z_\eta - \theta_\eta z_\xi\right), \quad A_{24} = \frac{r}{\xi}\left(\theta_\xi z_\zeta - \theta_\zeta z_\xi\right),$$

$$A_{31} = 0 \quad A_{32} = -\frac{1}{\xi}\left(r_\zeta z_\eta - r_\eta z_\zeta\right), \quad A_{33} = \left(r_\xi z_\eta - r_\eta z_\xi\right), \quad A_{34} = -\frac{1}{\xi}\left(r_\xi z_\zeta - r_\zeta z_\xi\right),$$

$$A_{41} = 0 \quad A_{42} = \frac{r}{\xi}\left(r_\zeta \theta_\eta - r_\eta \theta_\zeta\right), \quad A_{43} = -r\left(r_\xi \theta_\eta - r_\eta \theta_\xi\right), \quad A_{44} = \frac{r}{\xi}\left(r_\xi \theta_\zeta - r_\zeta \theta_\xi\right).$$

Each component can be related from Eqs. (4) and (6) as:

$$J = \frac{r}{\xi}\left(r_\xi \theta_\zeta z_\eta + r_\zeta \theta_\eta z_\xi + r_\eta \theta_\xi z_\zeta - r_\eta \theta_\zeta z_\xi - r_\zeta \theta_\xi z_\eta - r_\xi \theta_\eta z_\zeta\right),$$

$$\xi_t = -\frac{1}{J}\frac{r}{\xi}\left(r_\tau \theta_\zeta z_\eta + r_\zeta \theta_\eta z_\tau + r_\eta \theta_\tau z_\zeta - r_\eta \theta_\zeta z_\tau - r_\zeta \theta_\tau z_\eta - r_\tau \theta_\eta z_\zeta\right),$$

$$\zeta_t = \frac{1}{J} r\left(r_\tau \theta_\xi z_\eta + r_\xi \theta_\eta z_\tau + r_\eta \theta_\tau z_\xi - r_\eta \theta_\xi z_\tau - r_\xi \theta_\tau z_\eta - r_\tau \theta_\eta z_\xi\right),$$

$$\eta_t = -\frac{1}{J}\frac{r}{\xi}\left(r_\tau \theta_\xi z_\zeta + r_\xi \theta_\zeta z_\tau + r_\zeta \theta_\tau z_\xi - r_\zeta \theta_\xi z_\tau - r_\xi \theta_\tau z_\zeta - r_\tau \theta_\zeta z_\xi\right)$$

$$\xi_r = \frac{1}{J}\frac{r}{\xi}\left(\theta_\zeta z_\eta - \theta_\eta z_\zeta\right), \qquad \zeta_r = -\frac{1}{J} r\left(\theta_\xi z_\eta - \theta_\eta z_\xi\right), \qquad \eta_r = \frac{1}{J}\frac{r}{\xi}\left(\theta_\xi z_\zeta - \theta_\zeta z_\xi\right),$$

$$\xi_\theta = -\frac{1}{J}\frac{1}{\xi}\left(r_\zeta z_\eta - r_\eta z_\zeta\right), \qquad \zeta_\theta = \frac{1}{J}\left(r_\xi z_\eta - r_\eta z_\xi\right), \qquad \eta_\theta = -\frac{1}{J}\frac{1}{\xi}\left(r_\xi z_\zeta - r_\zeta z_\xi\right),$$

$$\xi_z = \frac{1}{J}\frac{r}{\xi}\left(r_\zeta \theta_\eta - r_\eta \theta_\zeta\right), \qquad \zeta_z = -\frac{1}{J} r\left(r_\xi \theta_\eta - r_\eta \theta_\xi\right), \qquad \eta_z = \frac{1}{J}\frac{r}{\xi}\left(r_\xi \theta_\zeta - r_\zeta \theta_\xi\right).$$

The continuity, the Navier- Stokes and the energy equations (Eqs. (1)-(3)) are transformed to the ones in the generalized coordinates.

[Continuity equation]

$$\frac{1}{\xi}\frac{\partial}{\partial \xi}\left(J\xi V_{\xi}\right)+\frac{1}{\xi}\frac{\partial}{\partial \zeta}\left(JV_{\zeta}\right)+\frac{\partial}{\partial \eta}\left(JV_{\eta}\right)=0 \tag{7}$$

where

$$V_{\xi}=\xi_r v_r+\frac{1}{r}\xi_{\theta}v_{\theta}+\xi_z v_z, \quad V_{\zeta}=\xi\zeta_r v_r+\frac{1}{r}\xi\zeta_{\theta}v_{\theta}+\xi\zeta_z v_z, \quad V_{\eta}=\eta_r v_r+\frac{1}{r}\eta_{\theta}v_{\theta}+\eta_z v_z .$$

These velocities are called as contravariant velocities.

[Navier-Stokes equation]

$$\begin{aligned}
&\frac{\partial v_i}{\partial t}+\xi_t\frac{\partial v_i}{\partial \xi}+\zeta_t\frac{\partial v_i}{\partial \zeta}+\eta_t\frac{\partial v_i}{\partial \eta}\\
&+\frac{1}{J}\left[\frac{1}{\xi}\frac{\partial}{\partial \xi}\left(J\xi V_{\xi}v_i\right)+\frac{1}{\xi}\frac{\partial}{\partial \zeta}\left(JV_{\zeta}v_i\right)+\frac{\partial}{\partial \eta}\left(JV_{\eta}v_i\right)+e_r\left(-\frac{Jv_{\theta}^2}{r}\right)+e_{\theta}\left(\frac{Jv_r v_{\theta}}{r}\right)\right]\\
&=-\left(\xi_i\frac{\partial P}{\partial \xi}+\zeta_i\frac{\partial P}{\partial \zeta}+\eta_i\frac{\partial P}{\partial \eta}\right)e_i\\
&+\frac{Pr}{Ma}\frac{1}{J}\Bigg[\ \frac{1}{\xi}\frac{\partial}{\partial \xi}\left(J\xi\xi_r\xi_r\frac{\partial v_i}{\partial \xi}\right)+\frac{1}{\xi}\frac{\partial}{\partial \xi}\left(J\xi\xi_r\zeta_r\frac{\partial v_i}{\partial \zeta}\right)+\frac{1}{\xi}\frac{\partial}{\partial \xi}\left(J\xi\xi_r\eta_r\frac{\partial v_i}{\partial \eta}\right)\\
&\qquad+\frac{1}{\xi}\frac{\partial}{\partial \zeta}\left(J\xi\zeta_r\xi_r\frac{\partial v_i}{\partial \xi}\right)+\frac{\partial}{\partial \zeta}\left(J\xi\zeta_r\zeta_r\frac{\partial v_i}{\partial \zeta}\right)+\frac{\partial}{\partial \zeta}\left(J\xi\zeta_r\eta_r\frac{\partial v_i}{\partial \eta}\right)\\
&\qquad+\frac{\partial}{\partial \eta}\left(J\eta_r\xi_r\frac{\partial v_i}{\partial \xi}\right)+\frac{\partial}{\partial \eta}\left(J\eta_r\zeta_r\frac{\partial v_i}{\partial \zeta}\right)+\frac{\partial}{\partial \eta}\left(J\eta_r\eta_r\frac{\partial v_i}{\partial \eta}\right)\\
&\qquad+\frac{\partial}{\partial \xi}\left(J\frac{1}{r^2}\xi_{\theta}\xi_{\theta}\frac{\partial v_i}{\partial \xi}\right)+\frac{\partial}{\partial \xi}\left(J\frac{1}{r^2}\xi_{\theta}\zeta_{\theta}\frac{\partial v_i}{\partial \zeta}\right)+\frac{\partial}{\partial \xi}\left(J\frac{1}{r^2}\xi_{\theta}\eta_{\theta}\frac{\partial v_i}{\partial \eta}\right)\\
&\qquad+\frac{1}{\xi}\frac{\partial}{\partial \zeta}\left(J\frac{\xi}{r^2}\zeta_{\theta}\xi_{\theta}\frac{\partial v_i}{\partial \xi}\right)+\frac{1}{\xi}\frac{\partial}{\partial \zeta}\left(J\frac{\xi}{r^2}\zeta_{\theta}\zeta_{\theta}\frac{\partial v_i}{\partial \zeta}\right)+\frac{1}{\xi}\frac{\partial}{\partial \zeta}\left(J\frac{\xi}{r^2}\zeta_{\theta}\eta_{\theta}\frac{\partial v_i}{\partial \eta}\right)\\
&\qquad+\frac{\partial}{\partial \eta}\left(J\frac{1}{r^2}\eta_{\theta}\xi_{\theta}\frac{\partial v_i}{\partial \xi}\right)+\frac{\partial}{\partial \eta}\left(J\frac{1}{r^2}\eta_{\theta}\zeta_{\theta}\frac{\partial v_i}{\partial \zeta}\right)+\frac{\partial}{\partial \eta}\left(J\frac{1}{r^2}\eta_{\theta}\eta_{\theta}\frac{\partial v_i}{\partial \eta}\right)\\
&\qquad+\frac{1}{\xi}\frac{\partial}{\partial \xi}\left(J\xi\xi_z\xi_z\frac{\partial v_i}{\partial \xi}\right)+\frac{\partial}{\partial \xi}\left(J\xi\xi_z\zeta_z\frac{\partial v_i}{\partial \zeta}\right)+\frac{\partial}{\partial \xi}\left(J\xi\xi_z\eta_z\frac{\partial v_i}{\partial \eta}\right)\\
&\qquad+\frac{1}{\xi}\frac{\partial}{\partial \zeta}\left(J\xi\zeta_z\xi_z\frac{\partial v_i}{\partial \xi}\right)+\frac{\partial}{\partial \zeta}\left(J\xi\zeta_z\zeta_z\frac{\partial v_i}{\partial \zeta}\right)+\frac{\partial}{\partial \zeta}\left(J\xi\zeta_z\eta_z\frac{\partial v_i}{\partial \eta}\right)
\end{aligned}$$

$$\begin{aligned}
&+ \frac{\partial}{\partial \eta}\left(J\eta_z\xi_z \frac{\partial v_i}{\partial \xi}\right) + \frac{\partial}{\partial \eta}\left(J\eta_z\zeta_z \frac{\partial v_i}{\partial \zeta}\right) + \frac{\partial}{\partial \eta}\left(J\eta_z\eta_z \frac{\partial v_i}{\partial \eta}\right) \\
&+ e_r\left(-J\frac{v_r}{r^2} - J\frac{2}{r^2}\left(\frac{1}{r}\xi_\theta \frac{\partial v_\theta}{\partial \xi} + \frac{1}{r}\zeta_\theta \frac{\partial v_\theta}{\partial \zeta} + \frac{1}{r}\eta_\theta \frac{\partial v_\theta}{\partial \eta}\right)\right) \\
&+ e_\theta\left(-J\frac{v_\theta}{r^2} - J\frac{2}{r^2}\left(\frac{1}{r}\xi_\theta \frac{\partial v_r}{\partial \xi} + \frac{1}{r}\zeta_\theta \frac{\partial v_r}{\partial \zeta} + \frac{1}{r}\eta_\theta \frac{\partial v_r}{\partial \eta}\right)\right) \Bigg] \\
&+ e_z\left(\frac{Gr}{Re^2} T\right)
\end{aligned} \tag{8}$$

where, $v_i = (v_r, v_\theta, v_z)$.

[Energy equation]

$$\begin{aligned}
&\frac{\partial T}{\partial t} + \xi_t \frac{\partial T}{\partial \xi} + \zeta_t \frac{\partial vT}{\partial \zeta} + \eta_t \frac{\partial T}{\partial \eta} \\
&+ \frac{1}{J}\left[\frac{1}{\xi}\frac{\partial}{\partial \xi}\left(J\xi V_\xi T\right) + \frac{1}{\xi}\frac{\partial}{\partial \zeta}\left(JV_\zeta T\right) + \frac{\partial}{\partial \eta}\left(JV_\eta T\right)\right] \\
&= \frac{1}{Ma}\frac{1}{J}\Bigg[\frac{1}{\xi}\frac{\partial}{\partial \xi}\left(J\xi\xi_r\xi_r \frac{\partial T}{\partial \xi}\right) + \frac{1}{\xi}\frac{\partial}{\partial \xi}\left(J\xi\xi_r\zeta_r \frac{\partial T}{\partial \zeta}\right) + \frac{1}{\xi}\frac{\partial}{\partial \xi}\left(J\xi\xi_r\eta_r \frac{\partial T}{\partial \eta}\right) \\
&\qquad + \frac{1}{\xi}\frac{\partial}{\partial \zeta}\left(J\xi\zeta_r\xi_r \frac{\partial T}{\partial \xi}\right) + \frac{\partial}{\partial \zeta}\left(J\xi\zeta_r\zeta_r \frac{\partial T}{\partial \zeta}\right) + \frac{\partial}{\partial \zeta}\left(J\xi\zeta_r\eta_r \frac{\partial T}{\partial \eta}\right) \\
&\qquad + \frac{\partial}{\partial \eta}\left(J\eta_r\xi_r \frac{\partial T}{\partial \xi}\right) + \frac{\partial}{\partial \eta}\left(J\eta_r\zeta_r \frac{\partial T}{\partial \zeta}\right) + \frac{\partial}{\partial \eta}\left(J\eta_r\eta_r \frac{\partial T}{\partial \eta}\right) \\
&\qquad + \frac{\partial}{\partial \xi}\left(J\frac{1}{r^2}\xi_\theta\xi_\theta \frac{\partial T}{\partial \xi}\right) + \frac{\partial}{\partial \xi}\left(J\frac{1}{r^2}\xi_\theta\zeta_\theta \frac{\partial T}{\partial \zeta}\right) + \frac{\partial}{\partial \xi}\left(J\frac{1}{r^2}\xi_\theta\eta_\theta \frac{\partial T}{\partial \eta}\right) \\
&\qquad + \frac{1}{\xi}\frac{\partial}{\partial \zeta}\left(J\frac{\xi}{r^2}\zeta_\theta\xi_\theta \frac{\partial T}{\partial \xi}\right) + \frac{1}{\xi}\frac{\partial}{\partial \zeta}\left(J\frac{\xi}{r^2}\zeta_\theta\zeta_\theta \frac{\partial T}{\partial \zeta}\right) + \frac{1}{\xi}\frac{\partial}{\partial \zeta}\left(J\frac{\xi}{r^2}\zeta_\theta\eta_\theta \frac{\partial T}{\partial \eta}\right) \\
&\qquad + \frac{\partial}{\partial \eta}\left(J\frac{1}{r^2}\eta_\theta\xi_\theta \frac{\partial T}{\partial \xi}\right) + \frac{\partial}{\partial \eta}\left(J\frac{1}{r^2}\eta_\theta\zeta_\theta \frac{\partial T}{\partial \zeta}\right) + \frac{\partial}{\partial \eta}\left(J\frac{1}{r^2}\eta_\theta\eta_\theta \frac{\partial T}{\partial \eta}\right) \\
&\qquad + \frac{1}{\xi}\frac{\partial}{\partial \xi}\left(J\xi\xi_z\xi_z \frac{\partial T}{\partial \xi}\right) + \frac{\partial}{\partial \xi}\left(J\xi\xi_z\zeta_z \frac{\partial T}{\partial \zeta}\right) + \frac{\partial}{\partial \xi}\left(J\xi\xi_z\eta_z \frac{\partial T}{\partial \eta}\right) \\
&\qquad + \frac{1}{\xi}\frac{\partial}{\partial \zeta}\left(J\xi\zeta_z\xi_z \frac{\partial T}{\partial \xi}\right) + \frac{\partial}{\partial \zeta}\left(J\xi\zeta_z\zeta_z \frac{\partial T}{\partial \zeta}\right) + \frac{\partial}{\partial \zeta}\left(J\xi\zeta_z\eta_z \frac{\partial T}{\partial \eta}\right) \\
&\qquad + \frac{\partial}{\partial \eta}\left(J\eta_z\xi_z \frac{\partial T}{\partial \xi}\right) + \frac{\partial}{\partial \eta}\left(J\eta_z\zeta_z \frac{\partial T}{\partial \zeta}\right) + \frac{\partial}{\partial \eta}\left(J\eta_z\eta_z \frac{\partial T}{\partial \eta}\right)
\end{aligned}$$

(9).

In this analysis, fractional step method is utilized to solve these governing equations. Adams-Bashforth method is adapted for time advancement. The Crank-Nicholson scheme is applied only the circumferential constituent of the viscous terms in the Navier-Stokes and the energy equations in order to ensure a larger stability margin.

3.3 Boundary conditions

3.3.1 Boundary condition of the velocity

To derive the boundary condition of the velocity on the free surface, the balance between the shearing stress and the surface tension must be considered.

The relation between the shearing stress and the surface tension is shown in Fig. 2.

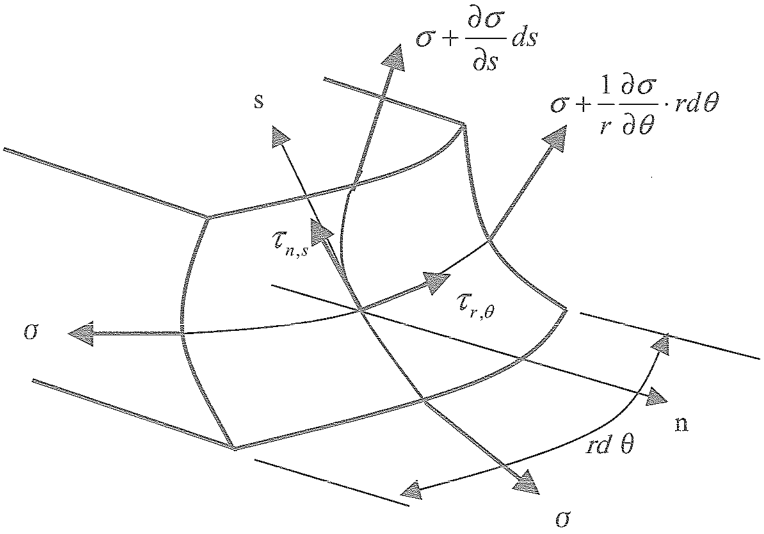

Figure 2: Stress balance between shearing stress and surface tension

From Fig. 2 the equations of the balance between the shearing stress and the surface tension are described as

$$\begin{cases} \tau_{n,s} \cdot r d\theta ds = \left\{ \left(\sigma + \frac{\partial \sigma}{\partial s} \cdot ds \right) - \sigma \right\} \cdot r d\theta \\ \tau_{r,\theta} \cdot r d\theta ds = \left\{ \left(\sigma + \frac{1}{r} \frac{\partial \sigma}{\partial \theta} \cdot r d\theta \right) - \sigma \right\} \cdot r ds \end{cases} \qquad (10).$$

Newton's law of viscosity is expressed as follows.

$$\begin{cases} \tau_{n,s} = \mu \left\{ \frac{\partial v_s}{\partial n} + \frac{\partial v_n}{\partial s} \right\} \\ \tau_{r,\theta} = \mu \left\{ \frac{1}{r} \frac{\partial v_r}{\partial \theta} + r \frac{\partial}{\partial r} \left(\frac{v_\theta}{r} \right) \right\} \end{cases} \qquad (11).$$

From Eqs. (10) and (11), equation (12) is derived.

$$\begin{cases} \mu\left\{\dfrac{\partial v_s}{\partial n}+\dfrac{\partial v_n}{\partial s}\right\}=\dfrac{\partial \sigma}{\partial s} \\ \mu\left\{\dfrac{1}{r}\dfrac{\partial v_r}{\partial \theta}+r\dfrac{\partial}{\partial r}\left(\dfrac{v_\theta}{r}\right)\right\}=\dfrac{1}{r}\dfrac{\partial \sigma}{\partial \theta} \end{cases} \qquad (12).$$

If the velocity on the free surface in the normal direction is assumed to be zero, equation (12) can be shown as follows.

$$\begin{cases} \mu\dfrac{\partial v_s}{\partial n}=\dfrac{\partial \sigma}{\partial s} \\ \mu\left\{\dfrac{1}{r}\dfrac{\partial v_r}{\partial \theta}+r\dfrac{\partial}{\partial r}\left(\dfrac{v_\theta}{r}\right)\right\}=\dfrac{1}{r}\dfrac{\partial \sigma}{\partial \theta} \end{cases} \qquad (13).$$

Equation (11) can be non-dimensionalized as following equations.

$$\begin{cases} \dfrac{\partial v_s}{\partial n}=-\dfrac{\partial \sigma}{\partial s} \\ \dfrac{1}{r}\dfrac{\partial v_r}{\partial \theta}+r\dfrac{\partial}{\partial r}\left(\dfrac{v_\theta}{r}\right)=-\dfrac{1}{r}\dfrac{\partial \sigma}{\partial \theta} \end{cases} \qquad (14)$$

In the equation of the relation between normal and tangential directions, the tangential velocity v_s is divided into radius and axial directions (See Fig. 3).

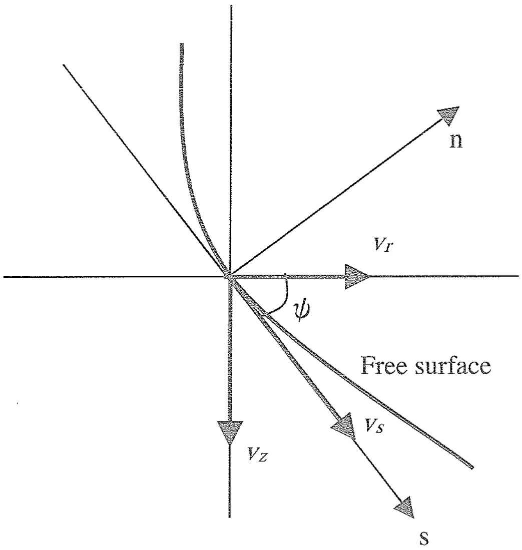

$$\begin{cases} v_r = v_s cos\varphi \\ v_z = v_s sin\varphi \end{cases} \qquad (15)$$

$$\Leftrightarrow \begin{cases} v_s = \dfrac{v_r}{cos\varphi} \\ v_s = \dfrac{v_z}{sin\varphi} \end{cases} \qquad (16)$$

$$\Leftrightarrow \begin{cases} \dfrac{\partial v_s}{\partial n} = \dfrac{\partial}{\partial n}\left(\dfrac{v_r}{cos\varphi}\right) \\ \dfrac{\partial v_s}{\partial n} = -\dfrac{\partial}{\partial n}\left(\dfrac{v_z}{sin\varphi}\right) \end{cases} \qquad (17)$$

$$\Leftrightarrow \begin{cases} \dfrac{\partial}{\partial n}\left(\dfrac{v_r}{cos\varphi}\right) = -\dfrac{\partial T}{\partial s} \\ \dfrac{\partial}{\partial n}\left(\dfrac{v_z}{sin\varphi}\right) = -\dfrac{\partial T}{\partial s} \end{cases} \qquad (18)$$

Figure 3: Velocity on the free surface

Generally the following relations are derived in the normal and tangential directions.

[Normal Derivatives]

$$\begin{cases} \dfrac{\partial \phi}{\partial n^{(\xi)}} = \dfrac{1}{J\sqrt{\alpha}}\left(\alpha\phi_\xi - \beta\phi_\eta\right) \\ \dfrac{\partial \phi}{\partial n^{(\eta)}} = \dfrac{1}{J\sqrt{\gamma}}\left(-\beta\phi_\xi + \gamma\phi_\eta\right) \end{cases} \tag{19}$$

[Tangential Derivatives]

$$\begin{cases} \dfrac{\partial \phi}{\partial s^{(\xi)}} = \dfrac{1}{\sqrt{\alpha}}\phi_\eta \\ \dfrac{\partial \phi}{\partial s^{(\eta)}} = \dfrac{1}{\sqrt{\gamma}}\phi_\xi \end{cases} \tag{20}$$

where, $\alpha = r_\eta^2 + z_\eta^2$, $\quad \beta = r_\xi r_\eta + z_\xi z_\eta$, $\quad \gamma = r_\xi^2 + z_\xi^2$.

Using eq. (19), the equation of the stress balance in normal and tangential directions is obtained.

$$\frac{1}{J\sqrt{\alpha}}\left(\alpha\frac{\partial v_z}{\partial \xi} - \beta\frac{\partial v_z}{\partial \eta}\right) = -sin\varphi\frac{1}{\sqrt{\alpha}}\frac{\partial T}{\partial \eta} \tag{21}$$

The axial velocity is derived from eq. (21). The radius velocity is derived from the relation of following equation.

$$v_r = \frac{cos\varphi}{sin\varphi}v_z \tag{22}$$

On the other hand, the boundary condition of the circumferential velocity is defined by

$$\frac{1}{r}\frac{\partial v_r}{\partial \theta} + r\frac{\partial}{\partial r}\left(\frac{v_\theta}{r}\right) = -\frac{1}{r}\frac{\partial T}{\partial \theta} \tag{23}$$

Equation (23) is transformed to the one in the computational domain by the Jacobian matrix as

$$\begin{aligned} &\frac{1}{r}\left(\xi_\theta\frac{\partial v_r}{\partial \xi} + \zeta_\theta\frac{\partial v_r}{\partial \zeta} + \eta_\theta\frac{\partial v_r}{\partial \eta}\right) + r\left(\xi_r\frac{\partial}{\partial \xi}\left(\frac{v_\theta}{r}\right) + \zeta_r\frac{\partial}{\partial \zeta}\left(\frac{v_\theta}{r}\right) + \eta_r\frac{\partial}{\partial \eta}\left(\frac{v_\theta}{r}\right)\right) \\ &= -\frac{1}{r}\left(\xi_\theta\frac{\partial T}{\partial \xi} + \zeta_\theta\frac{\partial T}{\partial \zeta} + \eta_\theta\frac{\partial T}{\partial \eta}\right) \end{aligned} \tag{24}$$

3.3.2 Boundary condition of the temperature

The condition of the heat transfer over the free surface is assumed to be adiabatic. Therefore the equation of the boundary condition of the temperature is

$$\frac{\partial T}{\partial n} = 0 \tag{25}$$

Equation (25) is transformed by the Jacobian matrix as

$$\frac{\partial T}{\partial \xi}\frac{\partial \xi}{\partial n}+\frac{\partial T}{\partial \zeta}\frac{\partial \zeta}{\partial n}+\frac{\partial T}{\partial \eta}\frac{\partial \eta}{\partial n}=0. \tag{26}$$

To transform into the computational domain, equation (19) is utilized.

$$\frac{\partial T}{\partial n}=\frac{1}{J\sqrt{\alpha}}\left(\alpha\frac{\partial T}{\partial \xi}-\beta\frac{\partial T}{\partial \eta}\right) \tag{27}$$

3.3.3 Treatment of the liquid center axis

In this analysis the governing equations are described in the cylindrical coordinate. Therefore the center of the cylinder (r = 0) can not be solved directly by the present equation. This problem is solved by a method described below. The computational grid is fixed at the center.

The Navier-Stokes equation in the axial direction and the energy equation at the center are derived by azimuthal integration.

[Navier-Stokes equation of the liquid center]

$$\begin{aligned}
&r\frac{\partial v_z}{\partial t}+\frac{\partial}{\partial r}\left(rv_rv_z\right)+\frac{\partial}{\partial \theta}\left(v_\theta v_z\right)+\frac{\partial}{\partial z}\left(rv_zv_z\right)\\
&=-r\frac{\partial P}{\partial z}+\frac{Pr}{Ma}\left[\frac{\partial}{\partial r}\left(r\frac{\partial v_z}{\partial r}\right)+\frac{\partial}{\partial \theta}\left(\frac{1}{r}\frac{\partial v_z}{\partial \theta}\right)+\frac{\partial}{\partial z}\left(r\frac{\partial v_z}{\partial z}\right)\right]\\
&\Rightarrow \frac{\partial v_z}{\partial t}+\frac{\Delta\theta}{\pi\Delta r}\sum_{\theta=0}^{2\pi}\left(v_rv_z\right)+\frac{1}{\Delta z}\left[v_z^2\right]_0^{\Delta z}\\
&\qquad=-\frac{\partial P}{\partial z}+\frac{Pr}{Ma}\left[\frac{\Delta\theta}{\pi\Delta r}\sum_{\theta=0}^{2\pi}\left.\frac{\partial v_z}{\partial r}\right|_{\Delta r}+\frac{1}{\Delta z}\left[\frac{\partial v_z}{\partial z}\right]_0^{\Delta z}\right]
\end{aligned} \tag{28}$$

[Energy equation]

$$\begin{aligned}
&r\frac{\partial T}{\partial t}+\frac{\partial}{\partial r}\left(rv_rT\right)+\frac{\partial}{\partial \theta}\left(v_\theta T\right)+\frac{\partial}{\partial z}\left(rv_zT\right)\\
&\qquad=\frac{1}{Ma}\left[\frac{\partial}{\partial r}\left(r\frac{\partial T}{\partial r}\right)+\frac{\partial}{\partial \theta}\left(\frac{1}{r}\frac{\partial T}{\partial \theta}\right)+\frac{\partial}{\partial z}\left(r\frac{\partial T}{\partial z}\right)\right]\\
&\Rightarrow r\frac{\partial T}{\partial t}+\frac{\Delta\theta}{\pi\Delta r}\sum_{\theta=0}^{2\pi}\left(v_rT\right)+\frac{1}{\Delta z}\left[v_zT\right]_0^{\Delta z}\\
&\qquad=\frac{1}{Ma}\left\{\frac{\Delta\theta}{\pi\Delta r}\sum_{\theta=0}^{2\pi}\left.\frac{\partial T}{\partial r}\right|_{\Delta r}+\frac{1}{\Delta z}\left[\frac{\partial T}{\partial z}\right]_0^{\Delta z}\right\}
\end{aligned} \tag{29}$$

As for the radius and circumference velocity at the center, the velocity is evaluated by summed value over the surrounding mesh points (See Fig.4).

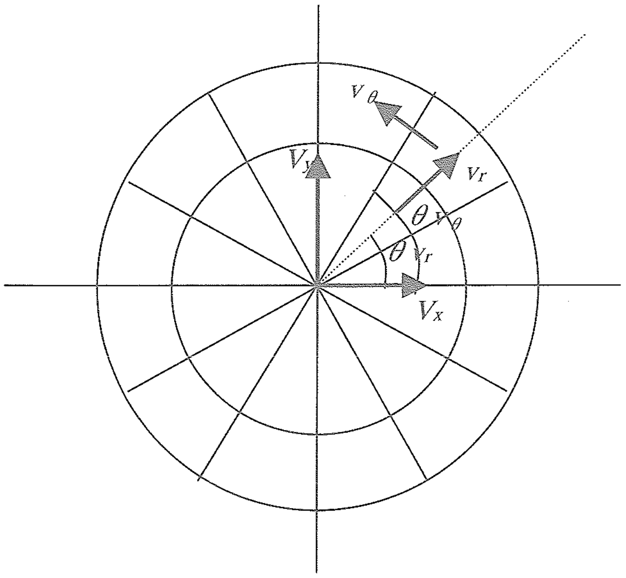

$$V_x = \sum_{\theta=0}^{2\pi}\left\{v_r cos\theta_{v_r} + v_\theta cos\left(\theta_{v_\theta} + \frac{\pi}{2}\right)\right\}$$

$$V_y = \sum_{\theta=0}^{2\pi}\left\{v_r sin\theta_{v_r} + v_\theta sin\left(\theta_{v_\theta} + \frac{\pi}{2}\right)\right\}$$

Figure 4: The velocity at the center axis

After the summation, the velocities V_x, V_y are divided into the radius and circumference components (v_r, v_θ) as follows;

$$\begin{aligned} v_r &= \left[V_x cos\theta_{v_r} + V_y cos\left(\frac{\pi}{2} - \theta_{v_r}\right)\right]\frac{1}{nj} \\ v_\theta &= \left[V_x\left(-sin\theta_{v_\theta}\right)cos + V_y sin\left(\frac{\pi}{2} - \theta_{v_\theta}\right)\right]\frac{1}{nj} \end{aligned} \qquad (31).$$

Here, nj shows the division number of the circumference direction. This treatment at the center axis is also applied to the energy equation.

3.4 Free surface deformation

The stress balance over the free surface must be considered to compute the free surface shape. Along the interface between two immiscible fluids (1) and (2), the forces over the surface must be balanced. If the surface is plane and the surface tension is constant, the stress balance over the surface leads

$$\mathbf{S}^{(1)} \cdot \mathbf{n} = \mathbf{S}^{(2)} \cdot \mathbf{n} \qquad (32)$$

where S is the stress tensor and n is the unit normal vector directed out of liquid (1) into the ambient fluid (2). The each component in the stress tensor is described as

$$S_{i,j} = -P\delta_{i,j} + \mu e_{i,j} \qquad (33),$$

where $e_{i,j}$ can be expressed in the cylindrical coordinate as

$$e_{rr} = \frac{\partial v_r}{\partial r}, \quad e_{\theta\theta} = \frac{1}{r}\frac{\partial v_\theta}{\partial \theta} + \frac{v_r}{r}, \quad e_{zz} = \frac{\partial v_z}{\partial z},$$
$$e_{r\theta} = \frac{1}{2}\left\{ r\frac{\partial}{\partial r}\left(\frac{v_\theta}{r}\right) + \frac{1}{r}\frac{\partial v_r}{\partial \theta} \right\}, \quad e_{\theta z} = \frac{1}{2}\left\{ \frac{1}{r}\frac{\partial v_z}{\partial \theta} + \frac{\partial v_\theta}{\partial z} \right\}, \quad e_{r\theta} = \frac{1}{2}\left\{ \frac{\partial v_r}{\partial z} + \frac{\partial v_z}{\partial r} \right\} \tag{34}$$

On the other hand, if the free surface has curvature and the surface tension varies along the interface, the equation of the stress balance becomes [8]

$$\mathbb{S}^{(1)} \cdot \mathbf{n} + \sigma(\nabla \cdot \mathbf{n})\mathbf{n} - (\mathbb{I} - \mathbf{nn}) \cdot \nabla\sigma = \mathbb{S}^{(2)} \cdot \mathbf{n} \tag{35}$$

where, I is the identity matrix. The element σ ($\nabla \cdot$ n) in the second term is so-called Laplace pressure. The mean curvatures of the interface,

$$\nabla \cdot \mathbf{n} = \frac{1}{R_1} + \frac{1}{R_2} \tag{36}$$

can be expressed as the sum of the inverse principle radii of curvatures R_1 and R_2. The mean curvatures of the interface can be described with Cartesian coordinate system as follows;

$$\begin{aligned}\nabla \cdot \mathbf{n} = \frac{-1}{R^3 N^3}\Bigg[& R\frac{\partial^2 R}{\partial z^2}\left\{R^2 + \left(\frac{\partial R}{\partial \theta}\right)^2\right\} \\ & + 2\frac{\partial R}{\partial z}\frac{\partial R}{\partial \theta}\left(\frac{\partial R}{\partial z}\frac{\partial R}{\partial \theta} - R\frac{\partial^2 R}{\partial z \partial \theta}\right) \\ & - \left\{1 + \left(\frac{\partial R}{\partial z}\right)^2\right\}\left\{R^2 + 2\left(\frac{\partial R}{\partial \theta}\right)^2 - R\frac{\partial^2 R}{\partial \theta^2}\right\}\Bigg]\end{aligned} \tag{37}$$

where, $N = \left[1 + \left(\frac{\partial R}{\partial z}\right)^2 + \frac{1}{R^2}\left(\frac{\partial R}{\partial \theta}\right)^2\right]^{\frac{1}{2}}$

The second term in the left hand side of equation (35) indicates the surface force acting tangentially originated from the surface tension σ. The operator I-nn represents the orthogonal projection of a vector onto the tangent plane defined by n.

Equation (35) can be non-dimensionalized using the scale as Table 1.

$$\mathbb{S}^{(1)} \cdot \mathbf{n} + \left(\frac{1}{Ca} - T\right)(\nabla \cdot \mathbf{n})\mathbf{n} - (\mathbb{I} - \mathbf{nn}) \cdot \nabla T = \mathbb{S}^{(2)} \cdot \mathbf{n} \tag{38}$$

Here, the dimensionless parameter is called the Capillary number, defined as

$$Ca = \frac{\sigma_T \Delta T}{\sigma_0} \tag{39}$$

From these equations, the equation of the stress balance is led in the three directions. Since the two directions of the curvature exist in the three dimension, the two tri-diagonal matrices must be considered for axial and circumferential directions. The tri-diagonal equations are indicated below.

[Radius direction]

$$
\begin{aligned}
\frac{\partial^2 R}{\partial z^2} = \frac{-R^3 N^3}{R\left\{R^2 + \left(\partial R/\partial\theta\right)^2\right\}\left(1/Ca - T\right)} \Bigg[& \; Re\left(P^{(1)} - P^{(2)}\right) - \frac{Bo}{Ca}\left(H - z\right) - \frac{\partial v_r}{\partial r} \\
& - \frac{1}{2}\left\{ r\frac{\partial}{\partial r}\left(\frac{v_\theta}{r}\right) + \frac{1}{r}\frac{\partial v_r}{\partial \theta}\right\}\frac{n_\theta}{n_r} - \frac{1}{2}\left(\frac{\partial v_r}{\partial z} + \frac{\partial v_z}{\partial r}\right)\frac{n_z}{n_r} \\
& - \frac{1 - n_r^2}{n_r}\frac{\partial T}{\partial r} + n_\theta \frac{1}{r}\frac{\partial T}{\partial \theta} + n_z \frac{\partial T}{\partial z} \Bigg] \\
& + \frac{1}{R\left\{R^2 + \left(\partial R/\partial\theta\right)^2\right\}}\Bigg[-2\frac{\partial R}{\partial z}\frac{\partial R}{\partial \theta}\left(\frac{\partial R}{\partial z}\frac{\partial R}{\partial \theta} - R\frac{\partial^2 R}{\partial z \partial \theta}\right) \\
& + \left\{1 + \left(\frac{\partial R}{\partial z}\right)^2\right\}\left\{R^2 + 2\left(\frac{\partial R}{\partial \theta}\right)^2 - R\frac{\partial^2 R}{\partial \theta^2}\right\}\Bigg]
\end{aligned}
\tag{40}
$$

[Circumferential direction]

$$
\begin{aligned}
\frac{\partial^2 R}{\partial \theta^2} = \frac{-R^3 N^3}{R\left\{R^2 + \left(\partial R/\partial z\right)^2\right\}\left(1/Ca - T\right)} \Bigg[& \; Re\left(P^{(1)} - P^{(2)}\right) - \frac{Bo}{Ca}\left(H - z\right) - \frac{\partial v_r}{\partial r} \\
& - \frac{1}{2}\left\{ r\frac{\partial}{\partial r}\left(\frac{v_\theta}{r}\right) + \frac{1}{r}\frac{\partial v_r}{\partial \theta}\right\}\frac{n_\theta}{n_r} - \frac{1}{2}\left(\frac{\partial v_r}{\partial z} + \frac{\partial v_z}{\partial r}\right)\frac{n_z}{n_r} \\
& - \frac{1 - n_r^2}{n_r}\frac{\partial T}{\partial r} + n_\theta \frac{1}{r}\frac{\partial T}{\partial \theta} + n_z \frac{\partial T}{\partial z} \Bigg] \\
& + \frac{1}{R\left\{R^2 + \left(\partial R/\partial z\right)^2\right\}}\Bigg[-R\frac{\partial^2 R}{\partial z^2}\left\{R^2 + \left(\frac{\partial R}{\partial \theta}\right)^2\right\} \\
& - 2\frac{\partial R}{\partial z}\frac{\partial R}{\partial \theta}\left(\frac{\partial R}{\partial z}\frac{\partial R}{\partial \theta} - R\frac{\partial^2 R}{\partial z \partial \theta}\right)\Bigg] \\
& + \frac{2}{R}\left(\frac{\partial R}{\partial \theta}\right)^2 + R
\end{aligned}
\tag{41}
$$

In addition to these tri-diagonal equations, the constant volume equation is solved to maintain the volume of the liquid bridge.

$$
\int_0^H \int_0^{2\pi} \frac{1}{2} R^2 d\theta dz = V \tag{42}
$$

The position of the free surface R can be obtained by using Tri-Diagonal Matrix Algorithm (TDMA) in the axial and circumferential directions. [10]

4. RESULTS

Calculation of high Pr fluid needs fine grid in order to researches its quite thin thermal boundary layer. We perform the simulation with 2cSt silicone oil (Pr = 28.11), aspect ratio $\Gamma = 1.0$ and volume ratio = 1.0 under the zero gravity. The calculation gird points are increased up to $(r \cdot \theta \cdot z) = (56 \times 32 \times 70)$ with uniform size mesh. In the medium Pr case, we employed the grids in the last annual reports.

4.1 The effects of DSD on the flow field and the critical value

The steady flow states in the cases with and without the DSD are discussed. Temperature and velocity distributions in r-z plane, and those over the free surface are shown in fig.5 and fig.6, respectively. Those figure indicate the flow states at Ma = 20,000. No significant differences in those distributions can have seen in both cases. As for the case with DSD, the liquid bridge deformed statically from the straight cylinder as the initial shape. Statically deformed free surface and the pressure distribution over the free surface under the same conditions of figs.5 and 6 are shown in fig.7.

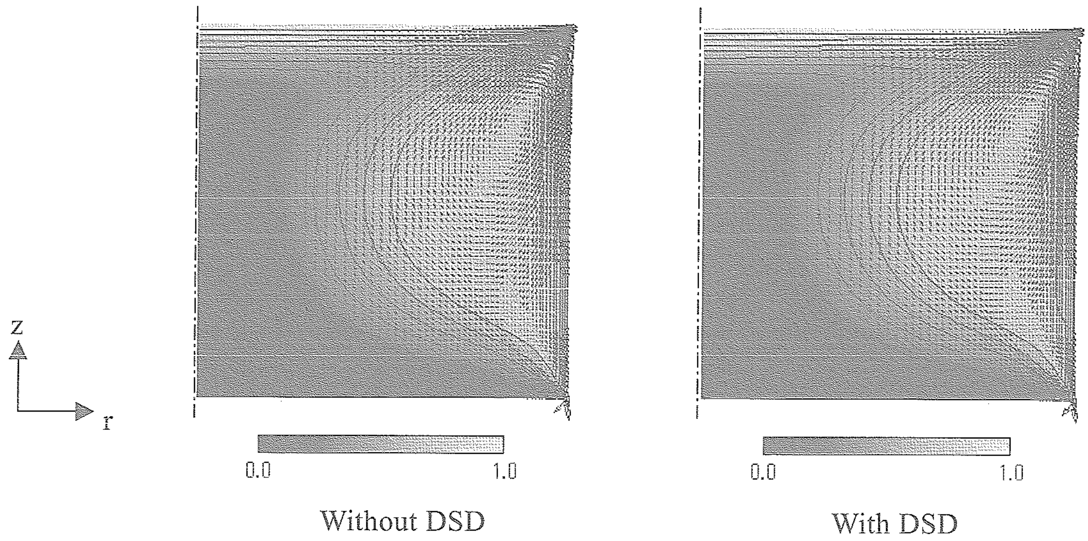

Figure 5: Temperature and velocity distribution for Ma = 30,000 with and without DSD.

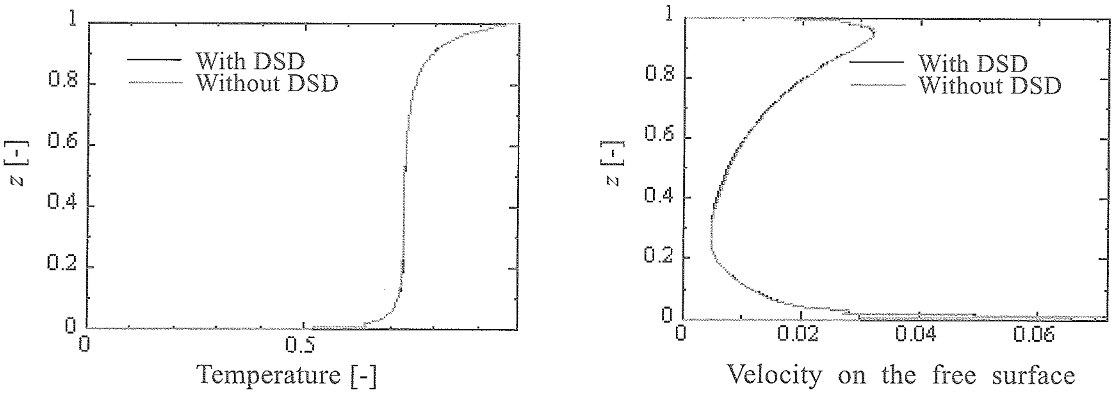

Figure 6: Free surface shape and pressure variation on the free surface for 2cSt silicone oil (Pr = 28.11), Ma= 30,000.

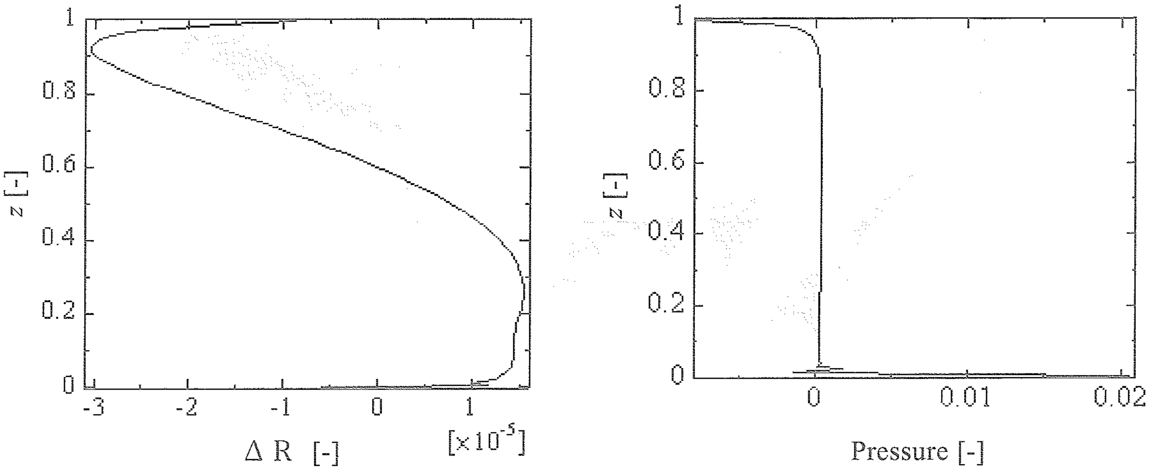

Figure 7: Free surface shape and pressure variation on the free surface for 2cSt silicone oil (Pr = 28.11), Ma = 30,000.

We evaluate the critical Marangoni numbers in the cases with and without DSD. Figure 8 shows the azimuthal velocity variation on the free surface at mid-height of the liquid bridge for both cases. Table 4 exhibits the evaluated value of Ma_c. In the case of high Pr fluid, the Ma_c with DSD shows a slightly lower value than the one without DSD. This tend is different from that in the case of medium Pr fluid as indicated in the last annual report; the Mac with DSD is almost equal to that without DSD.

At $Ma > Ma_c$, the flow exhibits a transition from the 2D steady to the 3D oscillatory flow in the both cases with and without DSD. It is noted that there exists a difference in the flow field after the transition; in the case without DSD, the flow changes into the standing-wave flow first, and then into the traveling-wave one soon. In the case with DSD, on the other hand, after exhibiting the standing-wave flow, that flow regime maintains for longer period. This can be indicated by monitoring. The azimuthal velocity and the temperature variations on the free surface at mid-height as shown in Fig.10. This figure shows the variations for Ma = 40,000. The black line indicates the value at $\theta = 1/4\pi$, which corresponds to the node point of the temperature and the anti-node point of the azimuthal velocity in the standing wave oscillation. On the other hand, the gray line indicates the value at $\theta = 0$, the anti-node point of the temperature and the node point of the azimuthal velocity. From this figure, the flow exhibits the standing wave flow at the early stage of the oscillation. The temperature and the azimuthal velocity of the node point are increasing. After all, the amplitudes of black and gray lines become equal, and the flow exhibit the traveling wave flow. With DSD, however, the temperature and the azimuthal velocity of the node point are not increasing but stable (Fig. 10(b)). With DSD, therefore, the flow field stays at standing wave flow for a long time.

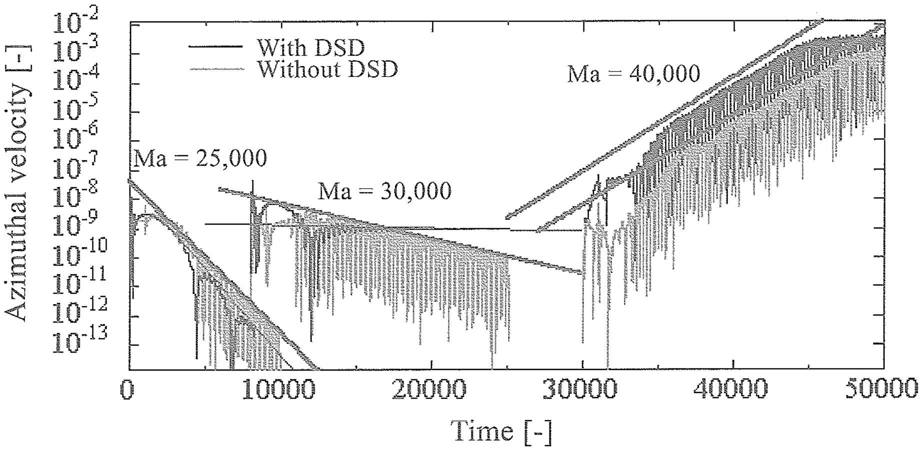

Figure 8: Azimuthal velocity variations for 2cSt silicone oil (Pr = 28.11), Ma = 25,000 ~ 40,000 with and without DSD

Table 4: Critical Marangoni number

2cSt silicone oil	Without DSD	With DSD
Ma_c	32,400	30,300

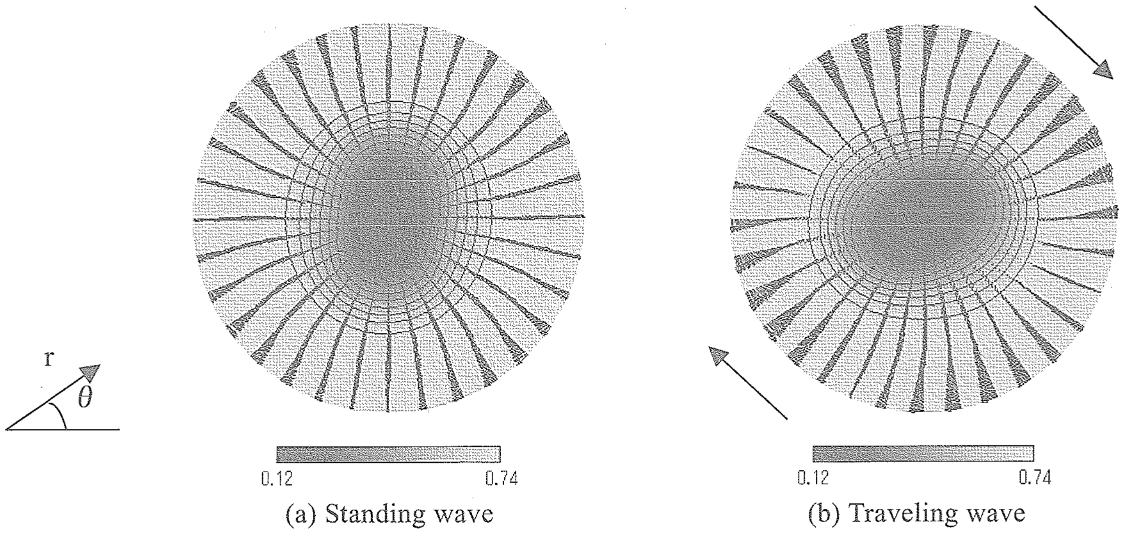

(a) Standing wave

(b) Traveling wave

Figure 9: Temperature and velocity distributions in the standing wave (a) and traveling wave (b) oscillation, 2cSt silicone oil (Pr = 28.11), Ma = 40,000 without DSD in r - θ place at mid-height.

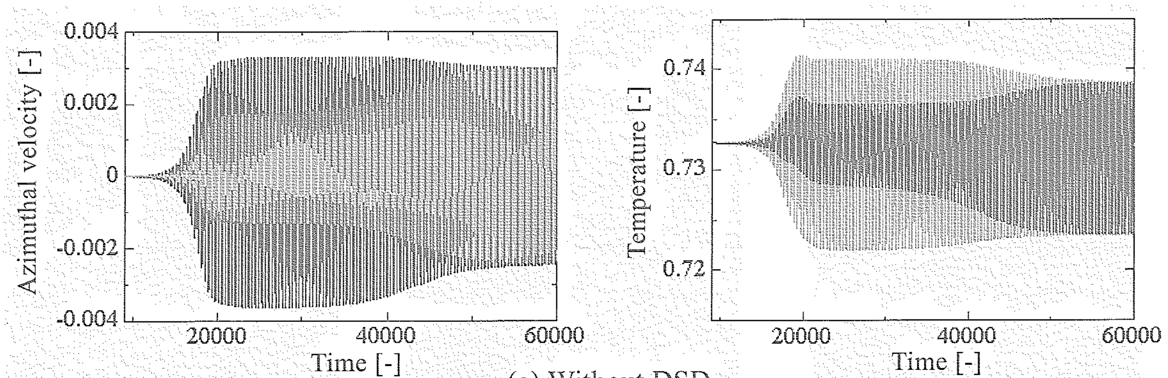

(a) Without DSD

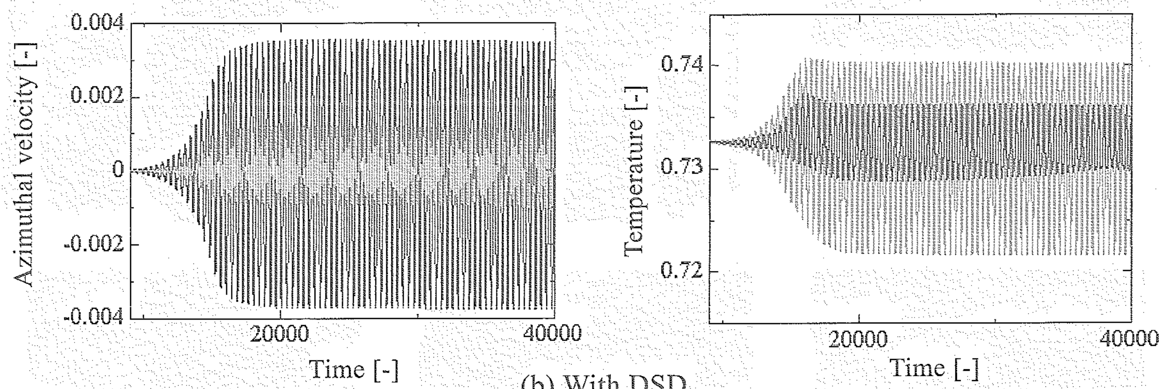

(b) With DSD

Figure 10: Azimuthal velocity and temperature variations at mid-height for 2cSt silicone oil (Pr = 28.11), Ma = 40,000. (a): without DSD, (b): with DSD. (black: θ = 1/4π, gray: θ = 0)

4.2 Spatiotemporal flow in the oscillatory state

Figure 11 shows the spatiotemporal correlation among the free surface deformation, the temperature and the pressure variations for the traveling wave state. Fluctuation of the free surface displacement from the initial position is magnified in 10^3 times. The difference from medium Pr fluid appears in this figure; as the fluid at lower temp reaches the free surface, the pressure in the vicinity of the free surface rises, and the surface expands. On the other hand, as the fluid at higher temp reaches the free surface, the pressure in the vicinity of the free surface falls, and the surface become concaved. Figure 12 shows the mutual correlations among the dynamic free surface deformation, the temperature, and the absolute axial velocity in the traveling-wave state at the different height. These figures show one cycle of oscillation in the traveling wave state. A phase lag of about π exists between the temperature difference and the surface deformation at any heights. Nishino et al. exhibited this correlation through the experiment (Figure 13(a)). The present results show a good agreement with the experimental results as shown in Fig.13.

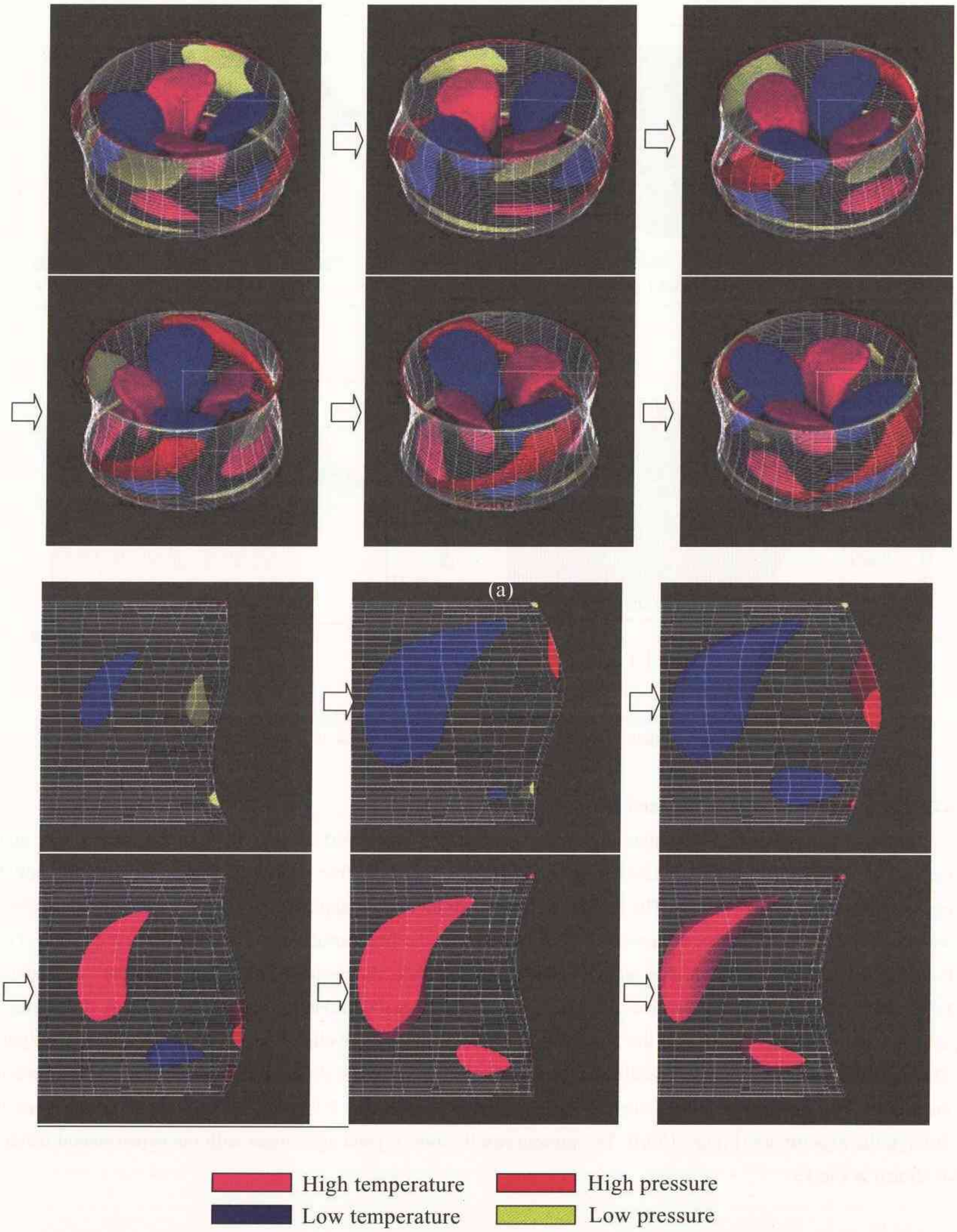

Figure 11: Bird's-eye view of traveling wave os cillation (a) and with fluctuations of temperature and pressure, in r – z place (b), 2cSt silicone oil (Pr = 28.11), Ma = 40,000. (DSD is magnified by a factor of 10^3)

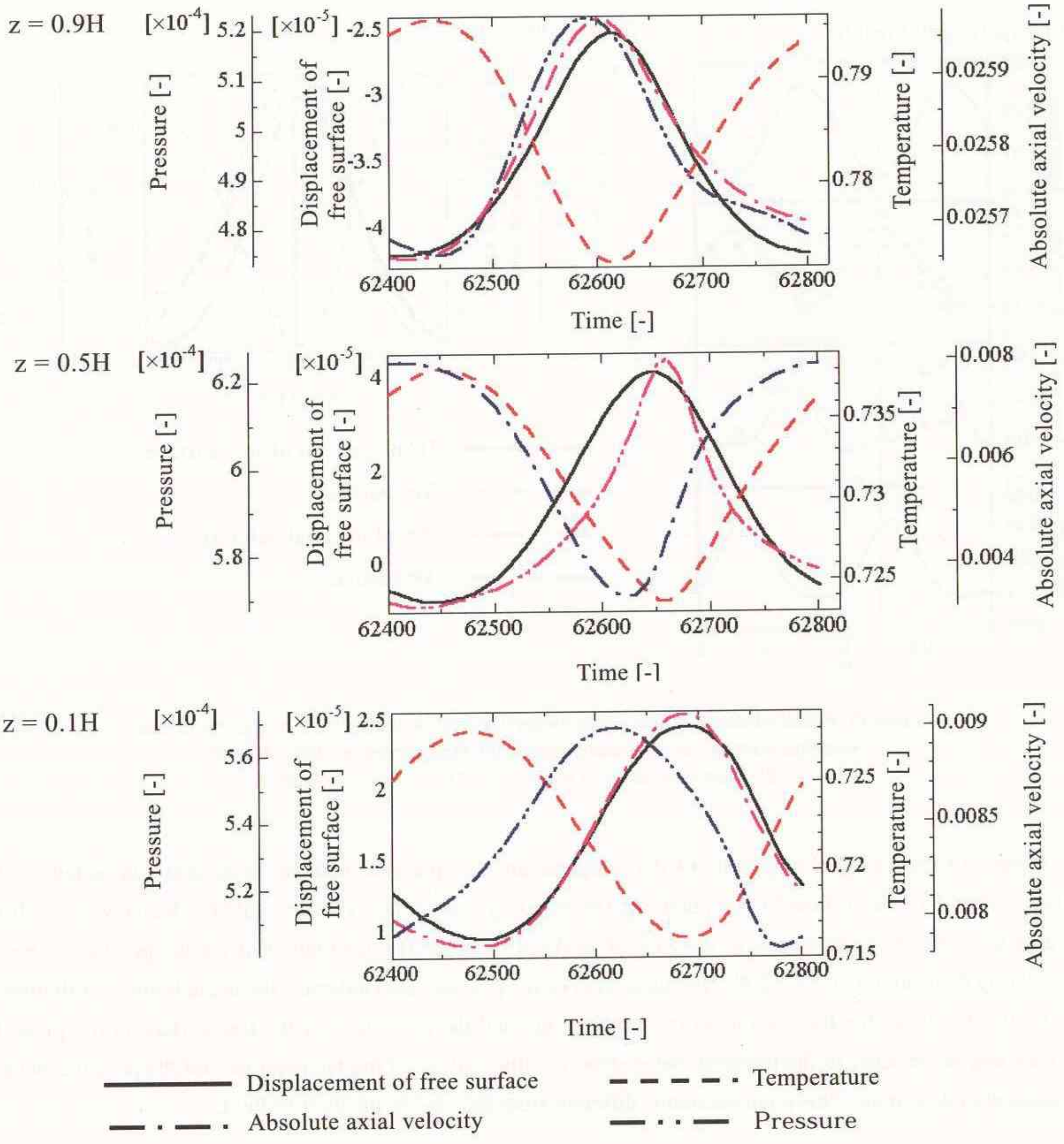

Figure 12: Relation between the surface deformation, pressure, temperature and absolute axial velocity near the both disks and at mid-height with DSD, 2cSt silicone oil, traveling wave oscillation, Ma = 40,000.

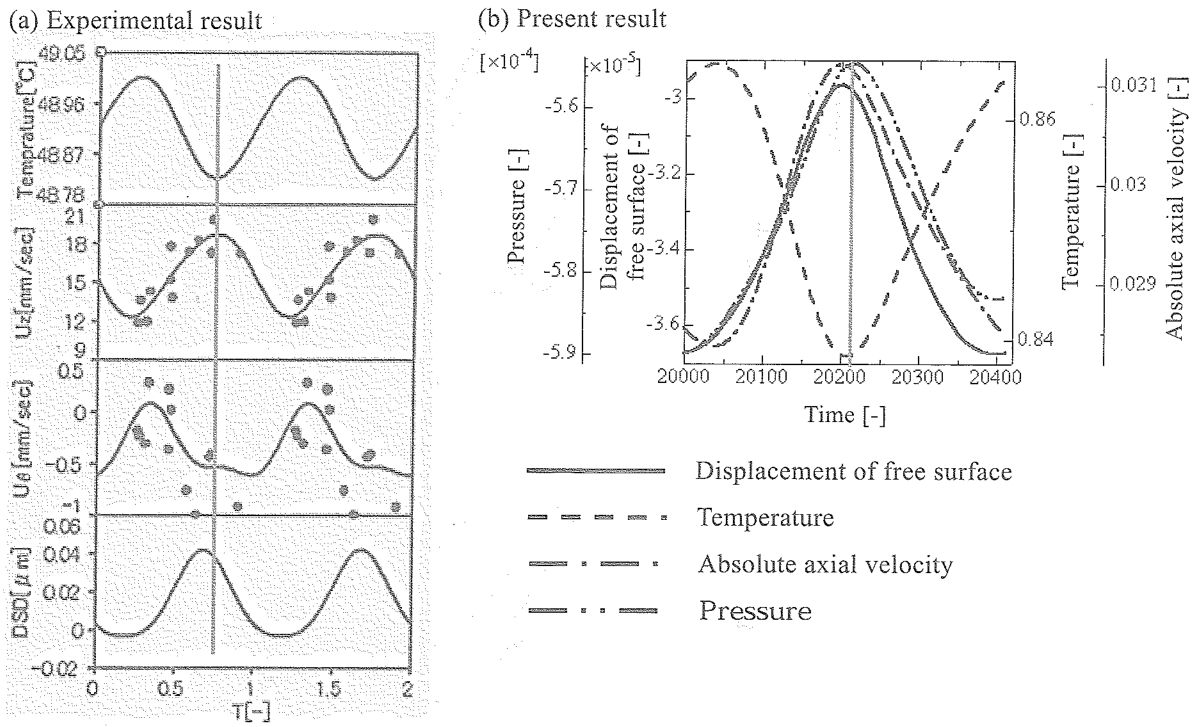
(a) Experimental result
(b) Present result

Figure 13: Relation between surface deformation, pressure, temperature and absolute axial velocity.z=0.96H, traveling wave oscillation, 2cSt silicone oil, Ma = 40,000.
(a): Experimental result (Nishino et al.), (b): Present result

Figure 14 shows the fluctuations of the temperature, the pressure and the azimuthal component of the velocity over the free surface in θ-z plane for the standing wave state. The azimuthal velocity vectors direct towards the coldest zone, as seen in the case of medium Pr fluid. The fluctuation of the temperature indicates meandering distribution at $z \sim 0.2\ H$. The fluctuation of the pressure also indicates the meandering distribution.

Figure 15 shows the fluctuations of the temperature and the pressure over the free surface in θ-z plane for the traveling wave state. In the traveling wave state, the fluctuations of the temperature and the pressure twist in the azimuthal directions. This phenomenon is different from the case of medium Pr fluid.

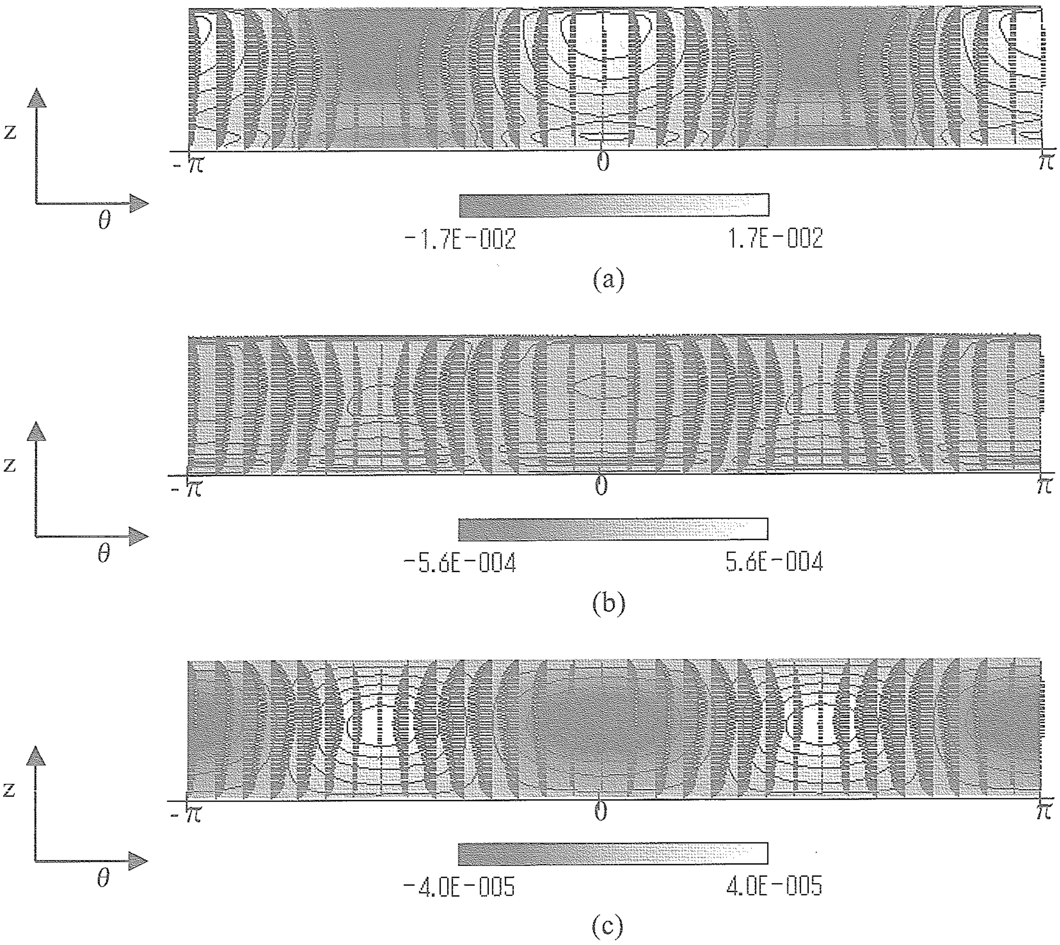

(a)

(b)

(c)

Figure 14: The fluctuations of the (a)temperature, (b)pressure, (c)surface deformation and the azimuthal velocity over the free surface with DSD in the standing wave in θ-z plane for Ma = 40,000, 2cSt silicone oil.

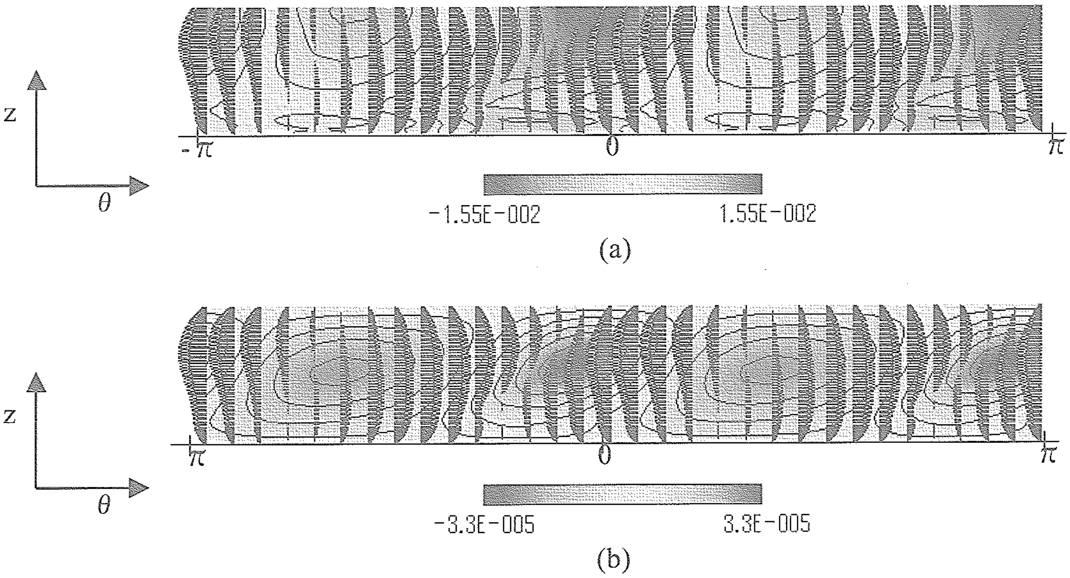

(a)

(b)

Figure 15: The fluctuations of the (a)temperature , (b)pressure and the azimuthal velocity over the free surface with DSD in the traveling wave in θ-z plane for Ma = 40,000, 2cSt silicone oil.

4.3 Comparison of the flow fields between the medium and high Pr fluid cases

In this section, the flow field of high Pr fluid is compared with that of low Pr fluid. Figure 16 shows the static free surface deformations in the case of the 2D steady flow. The free surface near the hot disk is concaved by low pressure due to Marangoni convection, and the one near the cold disk is expanded by high pressure in both cases. In the case of silicone oil, however, the free surface near the upper disk is widely concaved. Compared with the result of acetone the velocity near the upper disk is larger because of the steeper temperature gradient. The fluid vortex shifts up and the return-flow are strong.

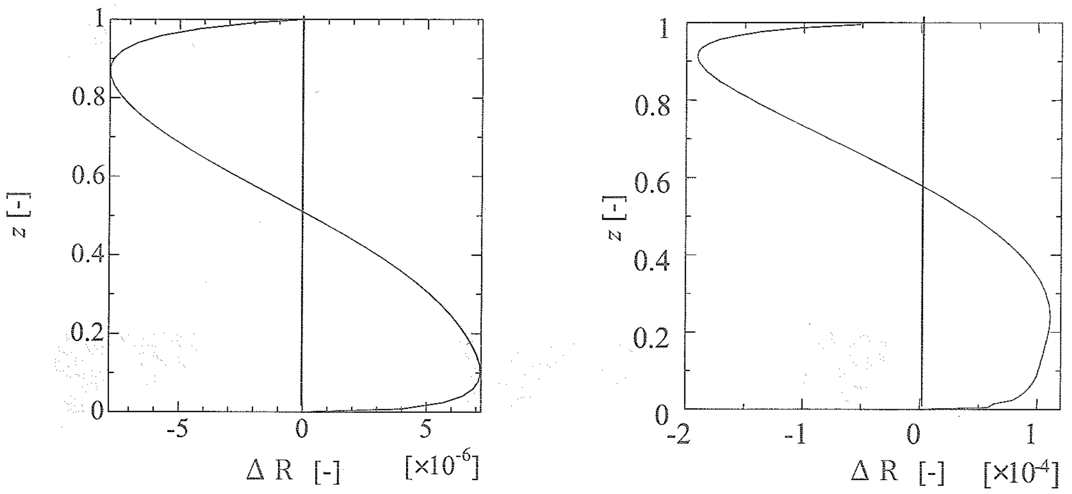

Figure 16: Free surface shape variations on the free surface (a): Acetone, Re = 900. (b): 2cSt silicone oil, Re = 890.

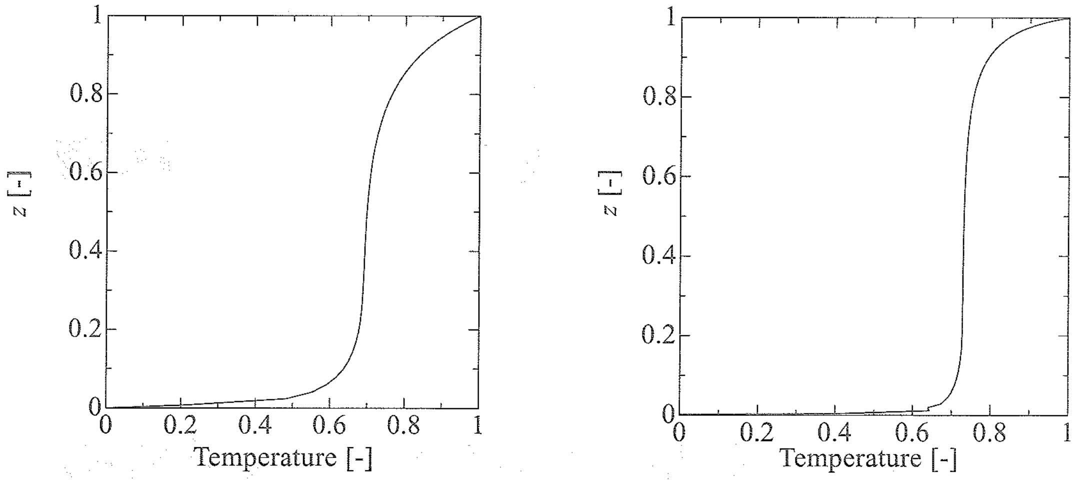

Figure 17: Temperature variations on the free surface (a): Acetone, Re = 900. (b): 2cSt silicone oil, Re = 890.

Figures 18 and 19 show the mutual correlations among the free surface deformation, the temperature and the pressure variations for the traveling wave state in the cases of 2cSt silicone oil and acetone, respectively. In both figure of medium and high Pr fluid, a phase lag exists between the temperature difference and the surface deformation. In case of high Pr fluid, this lag is about π. On the other hand, in case of medium Pr fluid, this lag is about π/2. It is conceived that the difference of a phase lag relates to height of the return-flow reaching. Figure 20 shows temperature and velocity distributions near the hot corner, in the r – z plane. Figure 21 shows fluctuations of the temperature and the velocity over the free surface in θ - z plane in a range of π/2 in θ. In the case of medium Pr fluid, low temperature field reaches widely to the free surface near upper disk. In the case of high Pr fluid, on the other hand, reaching range is narrow. Figure 21 shows that low temperature range is narrow near the upper disk. In medium Pr fluid, a phase relationship of high Pr fluid near the upper disk appears at little far from the upper disk.

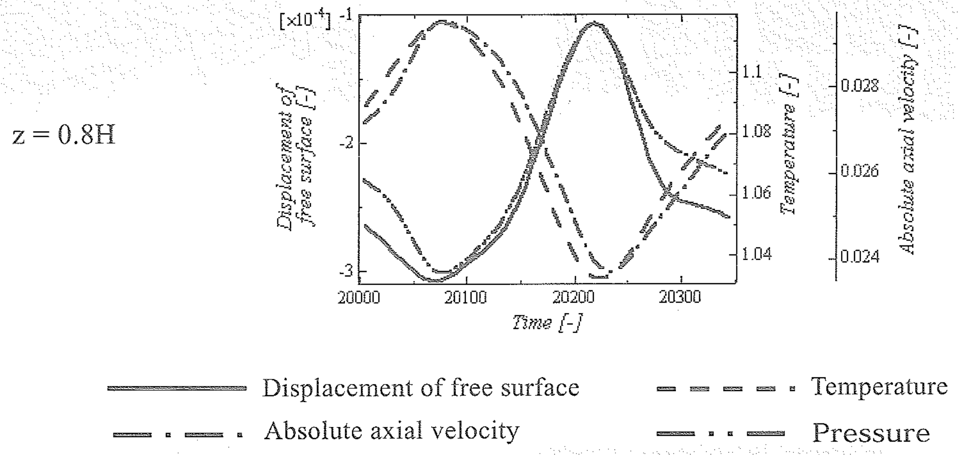

Figure 18: Relation between the surface deformation, pressure, temperature and absolute axial velocity near the both disks and at mid-height with DSD, 2cSt silicone oil, traveling wave oscillation, Ma = 40,000.

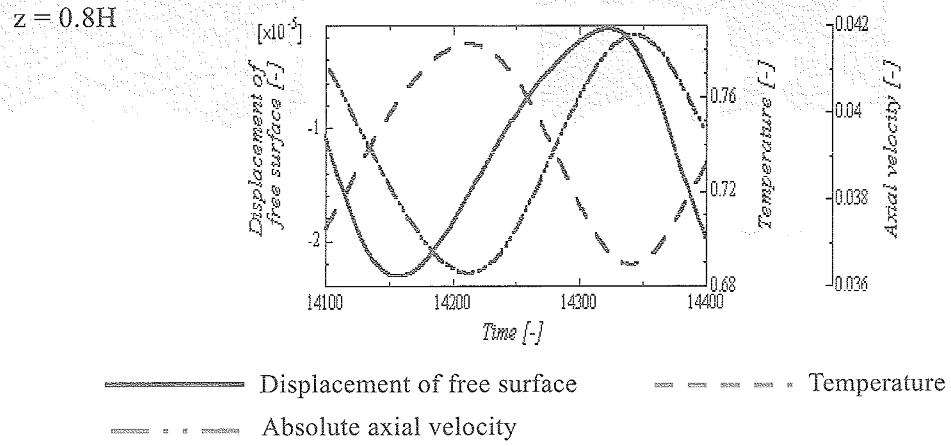

Figure 19: Relation between the surface deformation, temperature and absolute axial velocity at z = 0.8H with DSD, acetone, traveling wave oscillation, Re = 1,300.

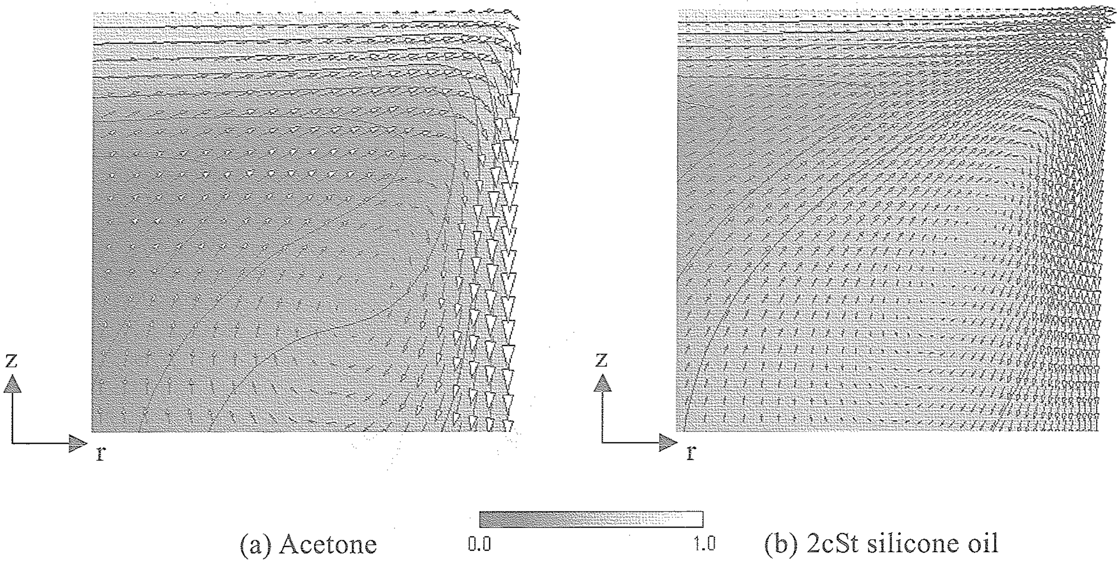

(a) Acetone (b) 2cSt silicone oil

Figure 20: Temperature and velocity distributions near the hot corner, r – z plane.
(a): Acetone, Re = 1,300. (b): 2cSt silicone oil, Re = 1,440.

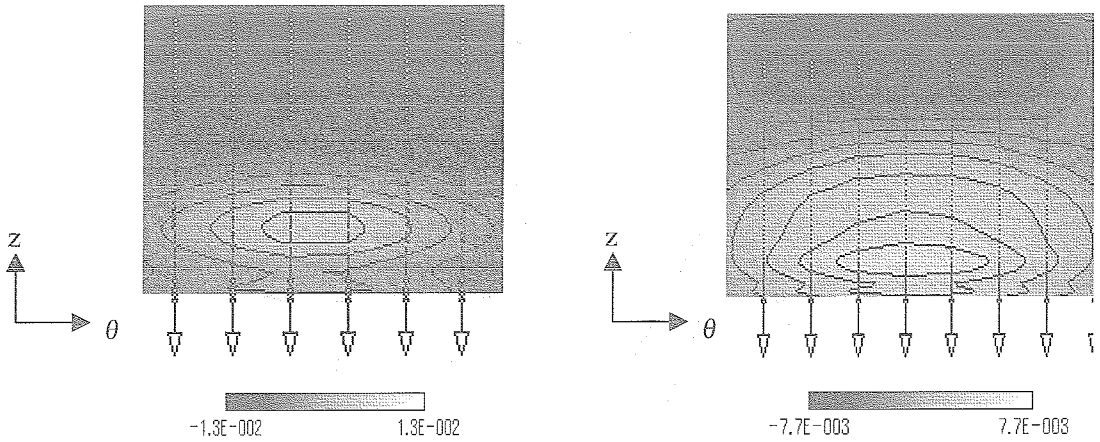

(a) Acetone

(b) 2cSt silicone oil

Figure 21: Fluctuations of the temperature and the velocity over the free surface in the standing wave oscillation in θ-z plane (π/2).
(a): Acetone, Re = 1,300. (b): 2cSt silicone oil, Re = 1,440.

5. CONCLUSIONS

(1) In the case of high Pr fluid, traveling flow with DSD using finer grids is obtained.

(2) The obtained critical Marangoni number in the case with DSD is smaller than the one without DSD.

(3) Mutual relation among DSD, temperature, pressure and axial velocity is obtained and is in good agreement with the experimental result near the hot corner (Nishino et al.).

(4) The differences of the oscillatory flow fields between the cases of acetone and of 2cSt silicone oil are indicated.

Effects of Small Vibrations on The Surface of a Liquid Bridge

By
R.Q. Liang and M. Kawaji

Abstract: The effects of small vibrations on the surface oscillation of a liquid bridge, especially the resonance behavior, were investigated numerically, using a three-dimensional code based on the level set method to capture the gas-liquid interface. The surface oscillation of an isothermal liquid bridge held vertically between solid disks was predicted, and the predictions were compared with an analytical model based on a mass-spring-damper analogy. By subjecting the liquid bridge to various horizontal vibrations, the surface resonance frequencies were clearly determined numerically and analytically. The numerical resonance frequencies compared well with the analytical model predictions. The effect of small vibrations on the surface oscillation amplitudes of the liquid bridge was also investigated.

1. INTRODUCTION

In preparation for a Marangoni convection experiment proposed in an International AO and to be conducted aboard the International Space Station using the Fluid Physics Experiment Facility (FEPF) in JEM, it is necessary to investigate the g-jitter induced oscillation of a liquid bridge surface. The liquid bridge in the IAO experiment simulates a floating zone method which is a popular technique used to produce single crystals of semiconductor materials. In this method, a solid rod is heated from outside to melt a part of the rod so that the molten material is held between two solid rods. By gradually moving the heated zone, the molten zone also moves leaving behind a crystal structure in the solidified zone. When the floating zone method is used in space, two effects have been identified which may produce fluid motion within the liquid bridge:

1. Marangoni convection due to a temperature and/or concentration gradient at the liquid surface,
2. Small accelerations referred to as g-jitter due to small vibrations.

Many investigations into Marangoni flow in the liquid bridge have shown that the Marangoni flow changes from a steady to oscillatory flow when the temperature and/or concentration gradient exceeds a critical value [1-7]. Such an oscillation in flow may lead to non-uniformities in crystal structure such as striations.

Apart from the effect of Marangoni convection, the behavior of the liquid bridge may also be affected significantly by small vibrations in space platforms such as the International Space Station. These vibrations are caused by the operation of various on-board devices, physical activities of astronauts, thruster firings for attitude control and so on. Since g-jitter is known to contain a wide spectrum of vibration frequencies and the liquid bridge may have one or more resonance frequencies, its free surface may oscillate dynamically with very high amplitudes, even though the vibration amplitude is very small. The dynamic oscillations of the free surface may in turn affect the oscillatory Marangoni convection phenomnena.

In order to predict the dynamic response of a liquid bridge to small vibrations under microgravity conditions, numerical and analytical models were developed. A three-dimensional numerical simulation model uses a DNS technique coupled with a level set approach to capture the interface motions of small amplitudes for non-

---

Department of Chemical Engineering and Applied Chemistry, University of Toronto, 200 College Street, Toronto, Ontario M5S 3E5, Canada

axisymmetric, viscous and isothermal liquid bridges. An analytical model had also been developed to predict the resonance behavior of a cylindrical liquid bridge subjected to horizontal vibrations. The model contained one adjustable parameter, the value of which has been determined in this work by comparing the predictions of the numerical and analytical models. The numerical model was then used to determine the vibration characteristics of liquid bridges of large diameter (D = 30 mm) and height (H = 10) under microgravity, subjected to single-frequency vibration normal to the liquid bridge axis.

2. NUMERICAL MODEL FORMULATION

2.1 EQUATIONS OF MOTION

The equations of motion for an incompressible flow are given by the following Navier-Stokes equations which include gravitational and small horizontal acceleration forces, and viscosity and surface tension effects.

$$\frac{\partial u}{\partial x}+\frac{\partial v}{\partial y}+\frac{\partial w}{\partial z}=0, \tag{1}$$

$$\frac{\partial u}{\partial t}=-u\frac{\partial u}{\partial x}-v\frac{\partial u}{\partial y}-w\frac{\partial u}{\partial z}+FGX+\frac{1}{\rho}\left(-\frac{\partial p}{\partial x}+\frac{\mu}{\mathrm{Re}}\left(\frac{\partial^2 u}{\partial x^2}+\frac{\partial^2 u}{\partial y^2}+\frac{\partial^2 u}{\partial z^2}\right)+\frac{1}{We}\kappa\delta(d)\mathbf{n}\right), \tag{2}$$

$$\frac{\partial v}{\partial t}=-u\frac{\partial v}{\partial x}-v\frac{\partial v}{\partial y}-w\frac{\partial v}{\partial z}+\frac{1}{\rho}\left(-\frac{\partial p}{\partial y}+\frac{\mu}{\mathrm{Re}}\left(\frac{\partial^2 v}{\partial x^2}+\frac{\partial^2 v}{\partial y^2}+\frac{\partial^2 v}{\partial z^2}\right)+\frac{1}{We}\kappa\delta(d)\mathbf{n}\right), \tag{3}$$

$$\frac{\partial w}{\partial t}=-u\frac{\partial w}{\partial x}-v\frac{\partial w}{\partial y}-w\frac{\partial w}{\partial z}+\frac{1}{Fr^2}+\frac{1}{\rho}\left(-\frac{\partial p}{\partial z}+\frac{\mu}{\mathrm{Re}}\left(\frac{\partial^2 w}{\partial x^2}+\frac{\partial^2 w}{\partial y^2}+\frac{\partial^2 w}{\partial z^2}\right)+\frac{1}{We}\kappa\delta(d)\mathbf{n}\right). \tag{4}$$

Here, $FGX=\frac{g_x\bar{L}}{U_\infty^2}$ is the body force in x direction induced by external acceleration, $g_x=A\omega^2\sin\omega t$ is the external acceleration in x direction, A is the vibration amplitude, $\omega=2\pi f$ is the angular frequency and f is the vibration frequency, u, v, and w are the fluid velocities in x, y, and z directions, respectively, $\rho=\rho$ (x, t) is the fluid density, $\mu=\mu$ (x, t) is the fluid viscosity, κ is the curvature of the interface, d is the normal distance to the interface, δ is the Dirac delta function, **n** is the unit normal vector at the interface, t is the time, and p is the pressure.

The dimensionless parameters used are Reynolds number, Froude number, and Weber number defined as $\mathrm{Re}=\frac{\rho_l\bar{L}U_\infty}{\mu_l}$, $Fr=U_\infty\sqrt{\frac{1}{g\bar{L}}}$, $We=\frac{\rho_l\bar{L}U_\infty^2}{\sigma}$, respectively, where ρ_l and μ_l are the liquid density and viscosity, respectively and g is the gravitational acceleration.

2.2 Level set function and its formulation

The level set method was originally introduced by Osher and Sethian [8] to numerically predict the moving interface between two fluids. Instead of explicitly tracking the interface, the level set method implicitly captures the interface by introducing a smooth signed distance from the interface in the entire computational domain. The level set function is taken to be positive outside the liquid bridge, zero at the interface and negative inside the liquid bridge. We consider a closed moving interface Γ(t), that encloses a region Ω(t). We associate Ω(t) with an auxiliary function ϕ (x, t), which is called the level set function,

$$\phi(\mathrm{x},t)=\begin{cases}dist(\mathrm{x},\Gamma(t),t) & if\ \ \mathrm{x}\ \ outside\ \ \Gamma(t)\\ -dist(\mathrm{x},\Gamma(t),t) & if\ \ \mathrm{x}\ \ inside\ \ \Gamma(t)\end{cases}, \tag{5}$$

$$\Gamma(t)=\left\{\mathrm{x}\in\Omega:\phi(\mathrm{x},t)=0\right\}. \tag{6}$$

The density ρ and viscosity μ in the flow field can then be expressed as follows.

$$\rho(\phi)=\rho_{in}+\left(\rho_{out}-\rho_{in}\right)H_\alpha(\phi), \tag{7}$$

$$\mu(\phi)=\mu_{in}+\left(\mu_{out}-\mu_{in}\right)H_\alpha(\phi), \tag{8}$$

$$H_\alpha(\phi)=\begin{cases}0 & \phi<-\alpha \\ (\phi+\alpha)/(2\alpha)+\sin(\pi\phi/\alpha)/2\pi & |\phi|\le\alpha \\ 1 & \phi>\alpha\end{cases}, \tag{9}$$

where the suffixes *in* and *out* stand for the liquid and gas phases, respectively, and α is the prescribed thickness of the interface. In this work, we used α = x/2.

The interface motion is predicted by solving the following convection equation for the level set function ϕ given by,

$$\phi_t+\mathbf{u}\cdot\nabla\phi=0. \tag{10}$$

The 3-D problem was solved in the following computational domain,

$$\Omega=\{(x,y,z)|\ \ 0\le x\le 4R,\ \ 0\le y\le 4R,\ \ 0\le z\le R\},$$

where R is the radius of the liquid bridge at the top and bottom. The non-slip condition was used at the upper and lower walls in contact with the liquid bridge, and the free-slip condition was used at the other wall boundaries.

2.3 Re-initialization of level set function

Because we initialize the level set function ϕ as a signed distance from the interface, we have

$$|\nabla\phi|=1. \tag{11}$$

When we move the level set function ϕ with Eq. (10), ϕ will no longer be a distance function and may become irregular at later times.

$$|\nabla\phi|\neq 1. \tag{12}$$

This will necessarily result in the variation of the interface thickness in time, making further computation and contour plotting highly inaccurate. Fortunately, we can ignore all values of ϕ far from the zero level set and replace the solution ϕ at any time by another function ϕ_0 with the same zero set as ϕ and then take ϕ_0 as the initial data to use. Sussman et al.'s [9] proposal for an iterative procedure is used to fulfill the above process.

$$\phi_t=sign(\phi_0)(1-|\nabla\phi|), \tag{13}$$

$$\phi(\mathbf{x},0)=\phi_0(\mathbf{x}). \tag{14}$$

2.4 Body force due to surface tension force

The model of Continuum Surface Force (CSF) was employed to treat the surface tension force at an interface, which interprets the surface tension force as a continuous effect across the interface rather than as a boundary condition on the interface [10]. By using the level set function, body force due to surface tension can be expressed as,

$$\frac{1}{We}\kappa\delta(d)\mathbf{n}=\frac{1}{We}\kappa(\phi)\delta(\phi)\nabla\phi. \tag{15}$$

The curvature of the interface is evaluated from

$$\kappa(\phi)=-(\nabla\cdot\mathbf{n})=-\nabla\cdot\left(\frac{\nabla\phi}{|\nabla\phi|}\right). \tag{16}$$

The Dirac delta function is defined as

$$\delta_\alpha(\phi)=\frac{dH_\alpha(\phi)}{d\phi}=\begin{cases}0 & |\phi|>\alpha \\ \dfrac{1}{2\alpha}\left[1+\cos\left(\dfrac{\pi\phi}{\alpha}\right)\right] & |\phi|\le\alpha\end{cases}. \tag{17}$$

2.5 Poisson equation solver

Briefly, we may write the Poisson equations for pressure as

$$\nabla \cdot \left(\frac{\nabla p}{\rho} \right) = \frac{\nabla \mathbf{G}}{\Delta t}, \tag{18}$$

$$\mathbf{G} = \begin{pmatrix} G_x \\ G_y \\ G_z \end{pmatrix} = \mathbf{u} + \Delta t \left(-(\mathbf{u} \cdot \nabla)\mathbf{u} + \frac{\mathbf{n}_{i\{i=x,z\}}}{Fr^2_{i\{i=x,z\}}} + \frac{1}{\rho} \left(\frac{1}{\mathrm{Re}} \nabla \cdot (2\mu D) + \frac{1}{We} \kappa(\phi) \delta(\phi) \nabla \phi \right) \right), \tag{19}$$

where $\mathbf{n}_{i(i=x,z)}$ is a unit normal vector in x or z direction.

The Successive Over Relaxation (SOR) method has been used to solve the Poisson equation for pressure.

2.6 The algorithm to catch small displacements of the surface

When a small vibration is applied, the movement of the liquid bridge surface can be extremely small, in the order of microns. It is not easy to capture such tiny surface movements in gas-liquid two phase flow simulations using grids of much larger dimensions. The Volume of Fluid method would have an insurmountable difficulty in overcoming this spatial resolution problem. In contrast, the level set approach can avoid this problem using a new algorithm developed in this work.

Step 1. Determine a monitoring point on the interface.
Step 2. Find out the grid point, which bounds the monitoring point outside the interface or on the interface when the interface moves through the grid at every time step.
Step 3. Calculate the position of the monitoring point.

Let us take a cross section in the x-y plane at a certain height of the liquid bridge. When the interface traverses through the grid, there are two ways for the interface to intersect with the grid. One way is that the interface intersects with the grid line between two grid points as shown in Fig. 1, and the other is the interface directly falling on one of the grid points. In Fig. 1, Γ represents the interface, and (i, j, k) and $(i+1, j, k)$ represent two arbitrary grid points on opposite sides of the interface (Γ). The level set function ϕ can be constructed by choosing the sign of ϕ to be negative inside the interface and positive outside the interface. If the interface intersects with the grid point, for example, (i, j, k), the level set function ϕ at this point should be zero and the position of the monitoring point in the x direction can be determined by using the coordinate value of (i, j, k). If the interface intersects with the grid line between the two grid points, for example, (i, j, k) and $(i+1, j, k)$, the two points should be determined as follows:

$$\phi(i,j,k)\phi(i+1,j,k) < 0\,. \tag{20}$$

According to the principle of the level set method, the value of the level set function ϕ at (i, j, k) is equal to the signed distance from this point to the interface. Therefore, the position of the monitoring point in the x direction can be determined by using the coordinate value of (i, j, k) and the value of the level set function ϕ at (i, j, k).

3. ANALYTICAL MODEL

An analytical model was previously developed by Ichikawa et al. [11] by considering a mass-spring-damper system to predict the resonance frequency of a cylindrical liquid bridge of diameter, D, and height, H. The model briefly summarized below was used to determine the functional dependence of the resonance frequency on the liquid bridge dimensions and physical properties. Let the following parameters represent the relevant system parameters: the moving liquid mass, m, damping coefficient, $2mk$, and restoring force (or spring) coefficient, $m\omega_0^2$. The forced external vibration is assumed to be given by $F_0 \sin\omega t$, where F_0 is the amplitude of the external force, ω is the angular frequency and t is time. The governing equation is given by,

$$m\ddot{x} + 2mk\dot{x} + m\omega_0^{\,2} x = F_0 \sin \omega t\ , \tag{21}$$

where x is the displacement of the center of mass of the liquid bridge from the equilibrium position. For $k < \omega_0$, an analytical solution to Eq. (21) is given by,

$$x = C \cdot e^{-kt} \cos\left(\sqrt{\omega_0^2 - k^2} \cdot t + \beta\right) + \frac{1}{\sqrt{\left(\omega_0^2 - \omega^2\right)^2 + 4k^2\omega^2}} \cdot \frac{F_0}{m} \sin\left(\omega t - q\right). \tag{22}$$

where C and β are constants, and q is determined from $\tan q = 2k\omega/(\omega_0^2 - \omega^2)$. The second term on the right-hand side is the particular solution and indicates the motion of the liquid bridge responding to the external forced vibration. If $k < \omega_0/\sqrt{2}$, this term has a local maximum at the following angular frequency,

$$\omega = \sqrt{\omega_0^{\,2} - 2k^2}\ . \tag{23}$$

Equation (23) shows the resonance frequency of the system, ω_R, at which the amplitude of the liquid bridge displacement is expected to be exceptionally large.

To apply these results to the liquid bridge motion, we need to evaluate the values of m, k and ω_0, and thus use the following assumptions.

1) Liquid is a Newtonian fluid and the flow induced within the liquid bridge is laminar.
2) The liquid bridge moves only in the horizontal direction. The shape of the horizontal cross section remains circular and the same at any height of the liquid bridge.
3) Gravity effects are negligible.

Evaluation of *m*

In the case of a deforming liquid bridge, the moving mass, m, is not the total mass of the liquid between the two disks because of the no-slip condition at the upper and lower disk surfaces. To account for this, a parameter, B, which is a ratio of the moving mass to the total mass of the liquid bridge is introduced. Then, the moving mass of the liquid bridge can be written as

$$m = \frac{\rho\pi D^2 H}{4} \cdot B\,, \tag{24}$$

where ρ is the liquid density. Possible values of B for three hypothetical situations are shown in Fig. 2.

Evaluation of *k* (Damping effect)

The value of k represents the damping effect, which is caused by the viscosity of the liquid bridge, μ. Under the assumption of the liquid bridge motion shown in Fig. 2 (c), the value of k is obtained from the following:

$$k = \frac{\pi D^2}{4mH}\mu = \frac{\nu}{H^2} \cdot \frac{1}{B}\,, \tag{25}$$

where ν $(=\mu/\rho)$ is the kinematic viscosity of liquid.

Evaluation of ω_0 (Restoring force)

The last parameter is the restoring force due to surface tension that brings the deformed surface to the equilibrium position given by a straight cylinder in this case. We can calculate the x-direction force from the integral of the pressure difference for the entire free surface of the liquid bridge. By assuming the principal radii of the surface curvature at any height are the same as those at the mid-height of the liquid bridge, the restoring force parameter is given by,

$$\omega_0 = \frac{4}{H}\sqrt{\frac{\sigma}{D\rho}\cdot\frac{1}{B}}. \tag{26}$$

Evaluation of resonance frequency

By combining Eqs. (22) through (26), the resonance frequency in Hz is given by,

$$f_R = \frac{\omega_R}{2\pi} = \frac{1}{2\pi H}\sqrt{\frac{2}{B}\left(\frac{8\sigma}{D\rho} - \frac{\nu^2}{H^2 B}\right)}. \tag{27}$$

The resonance frequency is predicted to decrease with increasing D, ρ and ν, and to increase with an increase in σ. In practical situations, the second term in the brackets is negligible in comparison with the first term. This is easily found if we calculate the two terms using the thermophysical properties of 5cSt silicone oil. In this situation, equation (27) can be written as,

$$f_R = \frac{2}{\pi H}\sqrt{\frac{\sigma}{D\rho B}}. \tag{28}$$

The resonance frequency would decrease with increases in H, D, ρ and B.

The analytical model was checked against a limited amount of available resonance frequency data obtained in space by Martinez [12] as shown in Table 1.

4. RESULTS AND DISCUSSION

4.1 Numerical simulation results

The present numerical simulations were performed using a mesh 51 x 51 x 51 and the physical properties of 5 cSt silicon oil under normal gravity as shown in Table 2. The initial shape of the liquid bridge is shown in Fig. 3, which is a straight cylinder. Both the liquid bridge and the surrounding air are at rest initially. After the computation is started, the liquid bridge shape first deforms due to gravity and then responds to the small vibrations applied in the horizontal direction. The amplitudes of periodic surface oscillations predicted were determined at different elevations above the bottom of the liquid bridge.

To quantify the response of the liquid bridge surface to small vibrations applied in the horizontal direction, simulations were systematically conducted for a liquid bridge under normal gravity using a 51 x 51 x 51 mesh. The diameter of the liquid bridge was 7.0 mm, and the height was 3.5 mm. The applied vibration frequencies ranged from 3 to 17 Hz, in increments of 2 Hz. The acceleration level in the horizontal direction was kept constant at 18-mg. Three monitoring points on the surface of the liquid bridge were selected at heights of $H/4$, $H/2$, $3H/4$, from the bottom disk. Figures 4 and 5 show the oscillation of the surface for vibration frequencies of 3Hz and 9Hz, respectively. Because of the deformation of the liquid bridge due to gravity, the surface oscillation amplitudes obtained at the three heights are different, and the mid-height of the bridge is the position that gives the largest amplitude among the three monitoring points as shown in Figs. 4 and 5. The tendency of the surface oscillation at heights $H/4$, $H/2$, and $3H/4$ is the same except for the initial period.

The relationship between the surface amplitude at the mid-height and the applied vibration frequency is shown in Fig. 6 for the case of a liquid bridge with the ratio of the minimum diameter of the liquid bridge to the disk diameter ($D_{\mathrm{min}}/D_{\mathrm{disk}}$) equal to 0.778. In Fig. 6, an extremely large amplitude can be seen at about 11Hz. The amplitudes at other vibration frequencies are much lower, and they have the same order of magnitude. It is clear that the resonance frequency is at about 11Hz in this set of computations.

4.2 Surface oscillation characteristics under microgravity

To compare the numerically predicted resonance frequency with that of an analytical model described earlier, additional numerical simulations were conducted under zero gravity. In this set of computations, the diameter and height of the liquid bridge were 8.4mm and 4.2mm, respectively, and the applied vibration frequency ranged from 3 to 17Hz. The acceleration level in the horizontal direction was again kept constant at 18-mg, and the mesh used was 51 x 51 x 51.

Figures 7 and 8 show the evolution of the surface position at the mid-height ($H/2$) for vibration frequencies of 3Hz and 9Hz, respectively. The surface of the liquid bridge vibrates periodically due to the horizontal vibration applied, and the amplitude almost reaches a constant value after a few cycles. The surface oscillation amplitude for the vibration frequency of 9Hz is much higher than that predicted for 3Hz. By measurement the amplitudes for the surface of the liquid bridge at every vibration frequency, the relation between the liquid bridge oscillation amplitude and the vibration frequency applied is obtained as shown in Fig. 9. The surface oscillation amplitude remains low at all vibration frequencies except for 9Hz, at which significantly larger amplitude is obtained due to the resonance behavior of the liquid bridge.

4.3 Effects of liquid bridge diameter and height on the resonance frequency

Figure 10 shows the relation between the numerically predicted resonance frequency and the disk diameter for a liquid bridge of H = 3.5mm. The calculations were performed at an acceleration level of 5mg in the absence of gravity. As predicted by the analytical model, Eq. (27) or (28), the resonance frequency decreases with the increasing disk diameter. The predictions of the analytical model are also shown in the figure for several different values of B, B=1 and B = 0.9 (for D = 5.0 mm) or 0.92 (for D = 7.0 and 10.0 mm), where B is the ratio of the moving mass to the total mass of the liquid bridge. In general, due to the no slip condition at the upper and lower disk surfaces, the moving mass is not the total mass of the liquid, thus B can not be equal to 1.0.

For the analytical model, we expected the value of B to fall between 1/2 and 1.0. By comparing the numerical results with the analytical model predictions, it is clear that the analytical predictions with B = 0.9 or 0.92 are closer to the numerical results than those obtained with B=1.0. That means about 90% of the mass of the liquid bridge is induced to move in response to the horizontal vibrations.

Next, the effect of the liquid bridge height on the resonance frequency is investigated. Three different liquid bridge heights were considered while keeping the diameter of the bridge constant at D = 7.0mm and the acceleration at 5mg in the absence of gravity. As shown in Fig. 11, the resonance frequency decreases with the increasing height of the liquid bridge. The resonance frequency varies over the range of 3-11Hz when the height of liquid bridge is changed from 3.5mm to 10.5mm. Both the computational results and the analytical model predictions show the same trend, and they agree closely for different values of the parameter B.

4.4 Effects of physical properties on the resonance frequency

Figure 12 shows the relation between the resonance frequency and density of the liquid bridge calculated for a liquid bridge of 3.5 mm height, 7.0 mm diameter, and an acceleration level of 5mg, in the absence of gravity. The density of the bridge was changed from 700 kg/m^3 to 1200 kg/m^3. It is clear from Fig. 12 that the resonance frequency decreases with the increasing density.

The effect of the liquid density predicted by the numerical model are in close agreement with the analytical model predictions. The best agreement is obtained with B = 0.9 ~ 0.92 rather than B = 1.0 in the analytical model.

4.5 The optimum value of *B*

In the analytical model, a parameter *B* was introduced, which is the ratio of the moving mass to the total mass of the liquid bridge. Its value was considered to fall between 1/2 and 1, but would depend on the height of the liquid bridge for a given diameter, or the aspect ratio. From several comparisons of analytical model predictions with the numerical simulations, it is clear that the best value of *B* is not constant for different aspect ratios of the liquid bridge. The relation between the best value of *B* and the aspect ratio has been determined and is shown in Fig. 13. Because of the no-slip condition at the upper and lower disk surfaces, as the liquid bridge height is increased, a smaller fraction of the total liquid mass would remain stationary despite the external vibrations. Thus, it is reasonable that the best value of *B* increases as the aspect ratio is increased, and reaches a constant value almost equal to unity when the aspect ratio is larger than 1.5.

4.6 Effects of liquid bridge height and diameter on the surface oscillation amplitude

Next, the numerical simulation results for the surface oscillation amplitudes are examined in detail. The effect of the liquid bridge height is studied for different vibration frequencies including the resonance frequency. Figure 14 shows the relation between the surface oscillation amplitude and liquid bridge height when the disk diameter is 7.0 mm and the acceleration level is 5 mg. From the curve corresponding to the resonance frequency, it is clear that the surface amplitude increases as the height is increased, especially when the height is large than 7.0 mm. At other vibration frequencies, changing the height does not affect the surface amplitude significantly. Because the resonance frequency of the liquid bridge decreases as the height is increased (the resonance frequency is 10.6Hz, 5.05Hz, 3.36Hz, at H=3.5mm, 7.0mm, and 10.5mm, respectively), the vibration frequency of 9Hz is always far from the resonance frequency and the surface amplitude does not increase with the liquid bridge height. For the vibration frequency of 1.0 Hz, the vibration energy imparted to the liquid bridge is smaller and the surface amplitude remains low regardless of the liquid bridge height.

4.7 Relation between the applied vibration amplitude and surface oscillation amplitude

The relation between the surface oscillation amplitude and applied vibration amplitude is shown in Fig. 15. Both the analytical model predictions with B = 0.9 and numerical simulation results show a linear relation between the applied vibration amplitude and surface amplitude of a liquid bridge with D = 7.0 mm, H = 3.5 mm, at an applied vibration frequency of 5Hz. This vibration frequency is well below the resonance frequency of 10.6Hz. As the applied vibration amplitude is increased from 10 microns to 200 microns while keeping the applied vibration frequency constant at 5Hz, the surface amplitude increases from 2.8 microns to 56 microns. The surface amplitude of the liquid bridge is approximately equal to 0.284 times the vibration amplitude. The analytical model predictions are again seen to be in good agreement with the numerical simulation results.

4.8 Predictions for larger cylindrical bridges

Finally, the surface oscillation of a large diameter liquid bridge for a vibration frequency of 5 Hz and acceleration level of 5 mg under microgravity is predicted as shown in Fig. 16. The liquid bridge diameter is 30.0 mm and the height is 10 mm. From this prediction, the surface amplitude is estimated to be about 100 microns. Another prediction for a vibration frequency of 9 Hz is shown in Fig. 17. The amplitude is smaller as the vibration frequency is further away from the resonance frequency which is predicted by the analytical model to be 1.706 Hz, if B = 1.0 is used. The relation between the numerically predicted surface amplitude and applied vibration frequency is shown in Fig. 18. The resonance frequency is predicted to be near 1.7 Hz, which is close to the analytically predicted value.

5. CONCLUSIONS

The vibration-induced oscillation of an isothermal liquid bridge has been investigated numerically. A three-dimensional DNS analysis of the liquid bridge was conducted using a level set approach to capture small surface oscillations for a non-axisymmetric liquid bridge induced by a horizontal vibration of different frequencies and amplitudes. An analytical model developed earlier based on a mass-spring-damper analogy was also used to compare with the numerical simulation predictions. Analytical expressions were derived for the surface oscillation amplitude and resonance frequency for a liquid bridge with the shape of a straight cylinder. From this work, the following conclusions can be drawn.

1. Three-dimensional oscillatory behavior of a liquid bridge could be predicted by the present numerical model, even for the case of a large density ratio between the liquid and surrounding gas. The level set approach can be used to capture micro-scale displacement of the free surface even though relatively coarse grids are used for simulation.
2. The existence of a resonance frequency, at which the oscillation amplitude of the liquid bridge increases significantly, was clearly predicted both analytically and numerically. The analytical model predictions and numerical simulation results were consistent with one another.
3. Numerical simulations have shown that the resonance frequency decreases with increases in height, diameter and density of the liquid bridge, but increases with surface tension. These predictions for the parametric dependence were consistent with the analytical model predictions.
4. The surface oscillation amplitude of the liquid bridge increases linearly with the applied vibration amplitude at non-resonance frequencies.
5. A comparison of the numerical results with the analytical model predictions showed that about 90% of the total mass of the liquid bridge would move in response to the horizontal vibrations. This fraction is predicted to increase with the liquid bridge height but decrease with the diameter.
6. The numerical simulation model can predict the vibration-induced oscillation of deformed liquid bridges under both normal gravity and microgravity, while the analytical model is applicable to liquid bridges with a straight cylindrical shape that are obtained only under microgravity.

ACKNOWLEDGMENTS

The authors would like to thank the Japan Aerospace Exploration Agency and Canadian Space Agency for financially supporting this IAO project.

REFERENCES

1. A. Pline, T. Jacobson, Y. Kamotani and S. Ostrach: Surface Tension Driven Convection Experiment, AIAA Paper 93-4312 (1993).
2. A. Hirata, S. Nishizawa, N. Imaishi, S. Yasuhiro, S. Yoda and K. Kawasaki: Oscillatory Marangoni Convection in a Liquid Bridge under Microgravity by Utilizing TR-IA Sounding Rocket, J. Jpn. Soc. Microgravity Appl., 10-4, 241 (1993).

3. K. Nishino, T. Yamasaki and M. Takami: Three-Dimensional Flow Visualization and Measurement of Suspended Liquid Bridge, J. Jpn. Soc. Microgravity Appl., 12-4, 205 (1995).
4. S. Nakamura, T. Hibiya, K. Kakimoto, N. Imaishi, S. Nishizawa, A. Hirata, K. Mukai, S. Yoda, and T. Morita: Temperature Fluctuations of the Marangoni Flow in a Liquid Bridge of Molten Silicon under Microgravity on Board the TR-IA-4 Rocket, J. Crystal Growth, 186, 85 (1998).
5. L. Carotenuto, D. Castagnolo, C. Albanese and R. Monti: Instability of Thermocapillary Convection in Liquid Bridges, Phys. Fluids, 10-3, 555 (1998).
6. V. M. Shevtsova and J.C. Legros: Oscillatory Convective Motion in Deformed Liquid Bridges, Phys. of Fluids, 10-7, 1621 (1998).
7. Q. S. Chen and W. R. Hu: Influence of Liquid Bridge Volume on Instability of Floating Half Zone Convection, Int. J. Heat Mass Transfer, 41, 825 (1998).
8. S. Osher and J. A. Sethian: Fronts Propagating with Curvature-Dependent Speed: Algorithms Based on Hamilton-Jacobi Formulations, J. Comput. Phys. 79, 49 (1988).
9. M. Sussman, P. Smereka, and S. Osher: A Level Set Approach for Computing Solutions to Incompressible Two-Phase Flow, J. Comput. Phys. 114, 146 (1994).
10. J. U. Brackbill, D. B. Kothe, and C. Zemach: A Continuum Method for Modeling Surface Tension, J. Comput. Phys. 100(2), 335 (1992).
11. N. Ichikawa, M. Kawaji and M. Misawa: Resonance Behavior of a Liquid Bridge Caused by Horizontal Vibrations. Journal of the Japan Society of Microgravity Applications, Vol. 20, No. 4, pp. 292-300 (2003).
12. I. Martinez: Stability of Liquid Bridges, Results of SL-D1 Experiment, Acta Astronautica, 15, 449 (1987).

Table 1. Comparison of analytical model predictions with SL-D1 experimental results by Martinez [12]

Experimental Run	Aspect Ratio (H/D)	Experimental Resonance Frequency (Hz)	Resonance frequency predicted by model (Hz) B=1.0
SL-D1-#2	2.71	0.18	0.17
SL-D1-#3	2.71	0.19	0.17
SL-D1-#4	2.86	0.17	0.16
SL-D1-#5	2.71	0.17	0.17
SL-D1-#6	2.57	0.19	0.18

Table 2. Physical properties for 5 cSt silicon oil

	5 cSt silicone oil	Air
Density ρ [kg/m^3]	915	1.226
Viscosity μ [kg/ms]	4.575×10^{-3}	1.78×10^{-5}
Surface tension σ [N/m]	1.97×10^{-2}	—
Gravity g [m/s^2]	9.81	

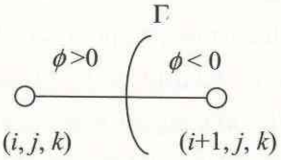

Fig. 1 An interface intersecting with a grid at x-y plane

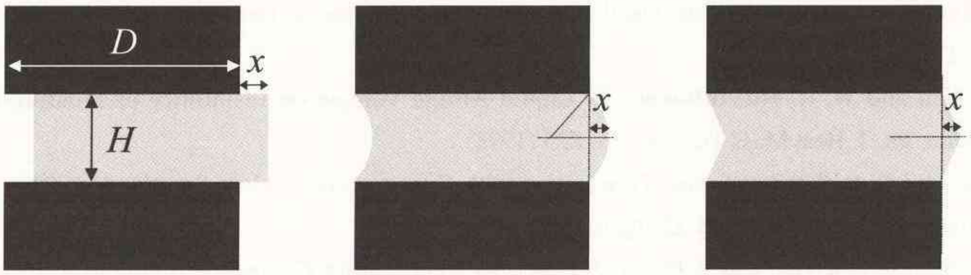

(a) whole liquid moving (B = 1) (b) curved interface (1/2 < B < 1) (c) triangular interface (B = ½)

Fig. 2 Models of a liquid bridge movement and values of B

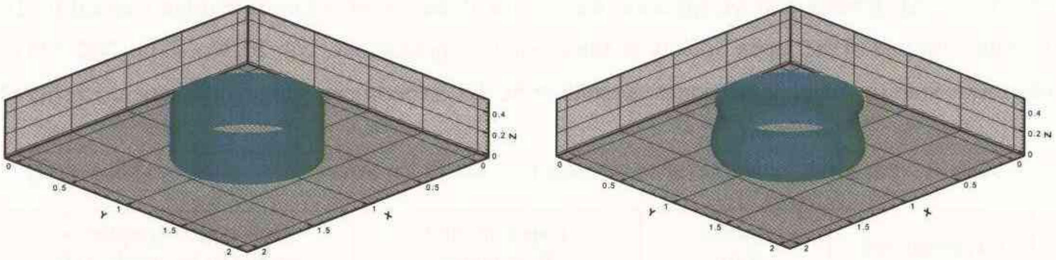

Fig. 3 Deformation of an initially cylindrical liquid bridge due to gravity

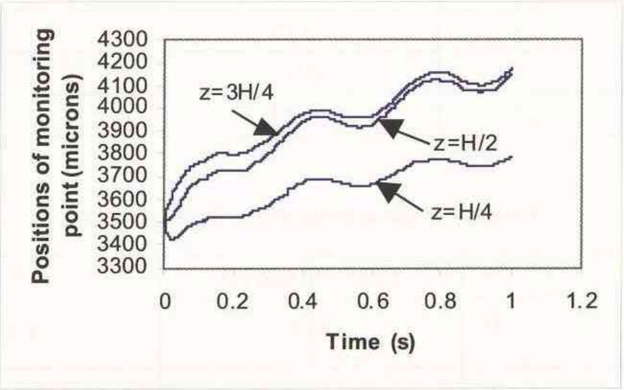

Fig. 4 Evolution of the surface positions at three different heights for a liquid bridge of D = 7.0 mm, H = 3.5 mm for an applied vibration frequency of 3Hz and acceleration level of 18 mg

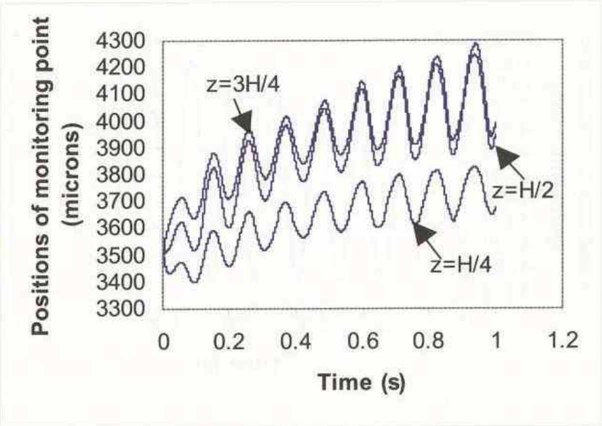

Fig. 5 Evolution of the surface positions at three different heights for a liquid bridge of D = 7.0 mm, H = 3.5 mm for an applied vibration frequency of 9Hz and acceleration level of 18 mg

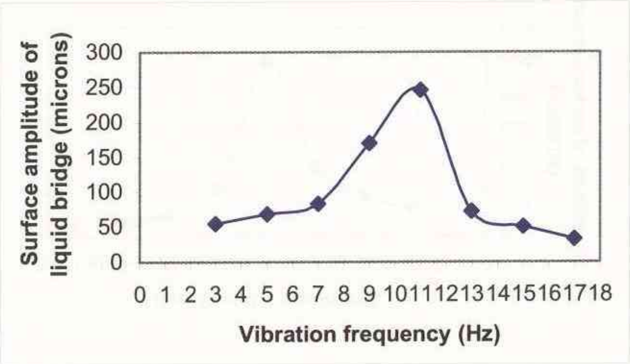

Fig. 6 Relation between surface oscillation amplitudes and applied vibration frequencies for a liquid bridge of D = 7.0 mm, H = 3.5 mm and the minimum diameter of the liquid bridge to the disk diameter (D_{min}/D_{disk}) = 0.778 under normal gravity

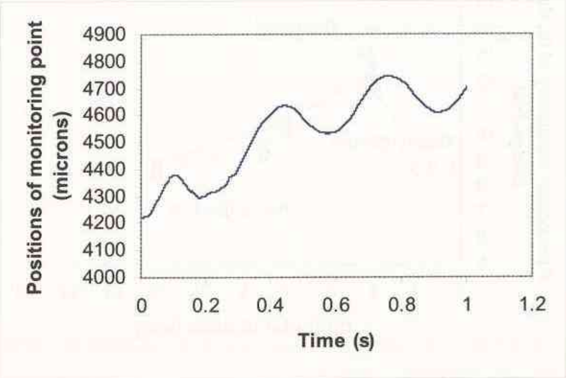

Fig. 7 Evolution of the surface position at mid-height for a liquid bridge of D = 8.4 mm and H = 4.2 mm at an applied vibration frequency of 3Hz and acceleration level of 18 mg

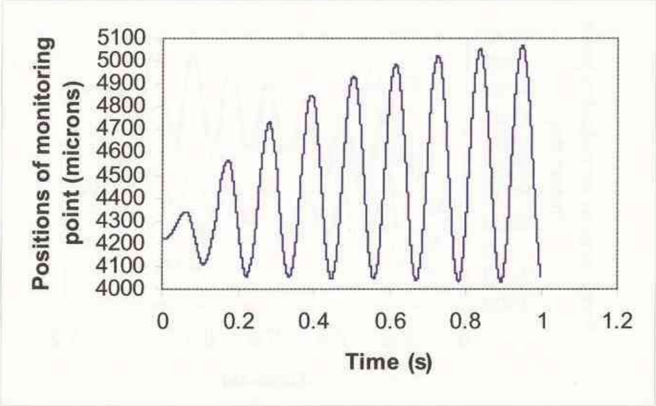

Fig. 8 Evolution of the surface position at mid-height for a liquid bridge of D = 8.4 mm and H = 4.2 mm at an applied vibration frequency of 9 Hz and acceleration level of 18 mg

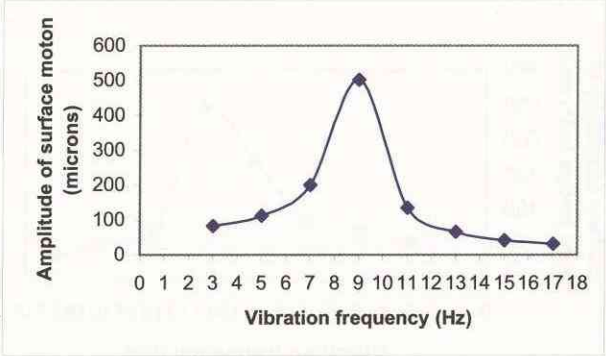

Fig.9 Relation between surface amplitude and vibration frequency for a liquid bridge of D = 8.4 mm and H = 4.2 mm

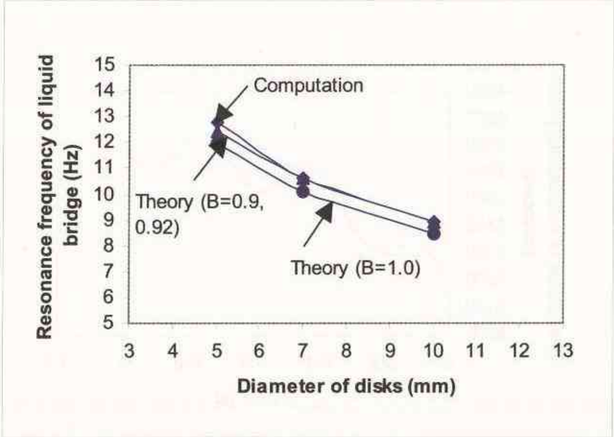

Fig. 10 Variation of resonance frequency with disk diameter for a liquid bridge of H = 3.5 mm

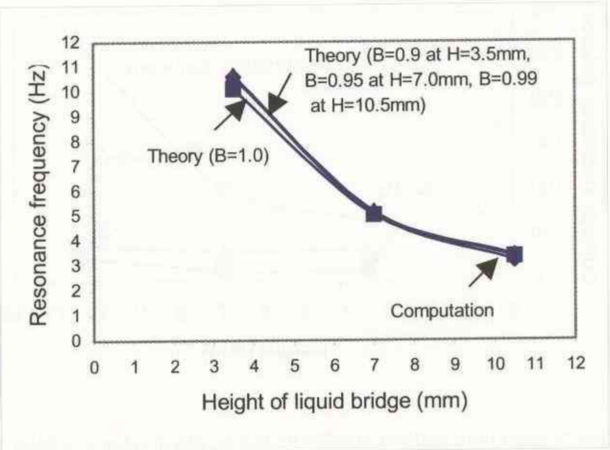

Fig. 11 Effect of liquid bridge height on resonance frequency for a liquid bridge of D = 7.0 mm

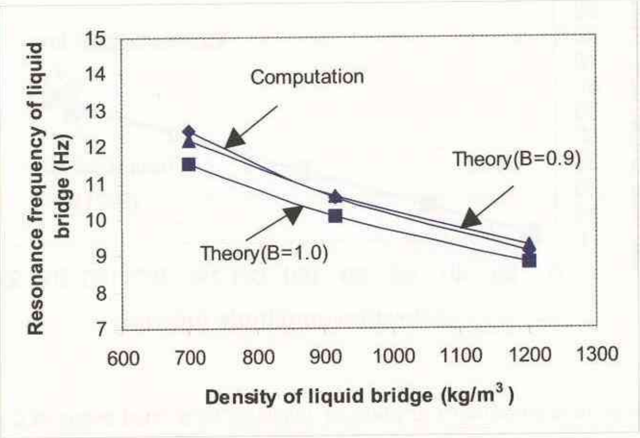

Fig. 12 Effect of density on the resonance frequency of a liquid bridge of D= 7.0mm and H = 3.5mm

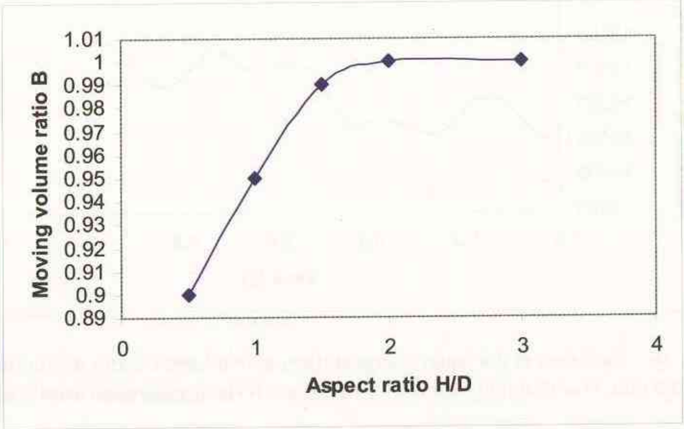

Fig. 13 Relation between moving volume ratio, B, and aspect ratio for a liquid bridge of D = 7.0 mm and H = 3.5 mm

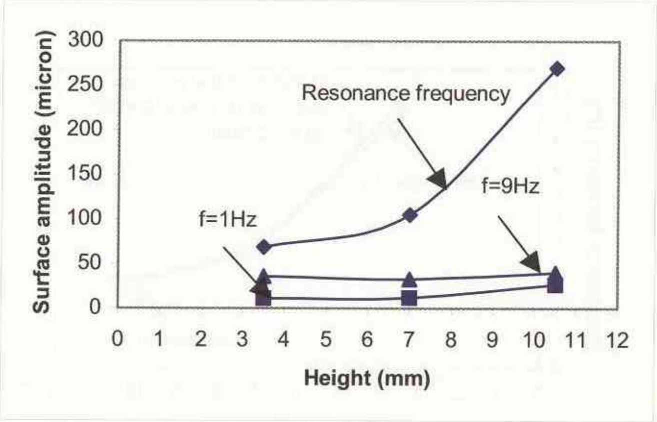

Fig. 14 Relation between the surface amplitude and height of a liquid bridge for D = 7.0 mm

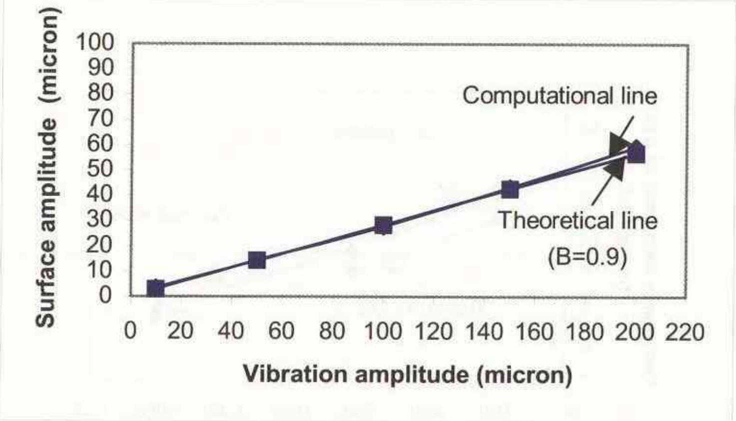

Fig. 15 Relation between surface amplitude and vibration amplitude for a liquid bridge of D = 7.0 mm and H = 3.5 mm

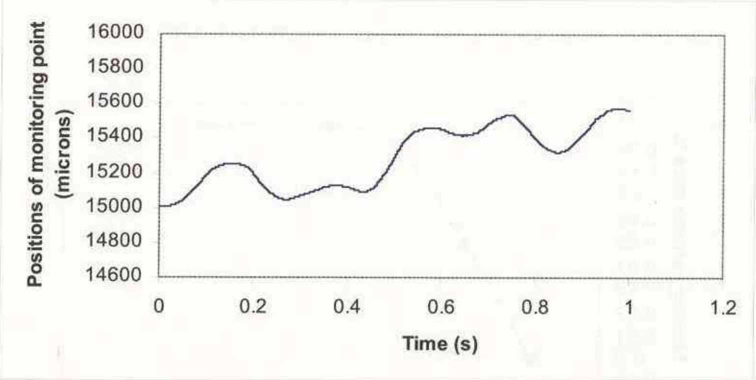

Fig. 16 Evolution of the liquid bridge surface at mid-height under microgravity
(D = 30.0 mm, H = 10.0 mm, vibration frequency = 5 Hz, acceleration level = 5.0 mg)

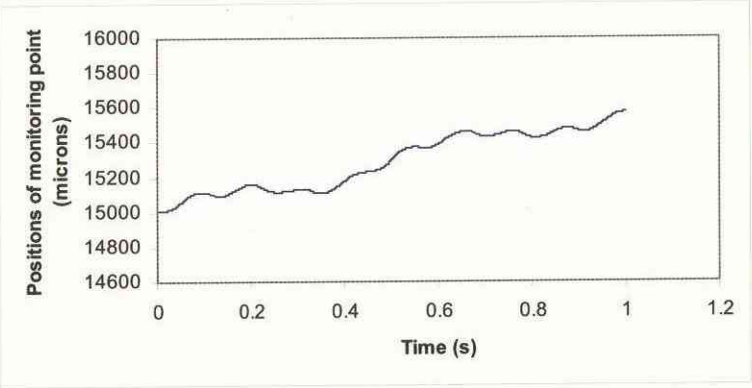

Fig. 17 Evolution of the liquid bridge surface at mid-height under microgravity (D = 30.0 mm, H = 10.0 mm, vibration frequency = 9 Hz, acceleration level = 5.0 mg)

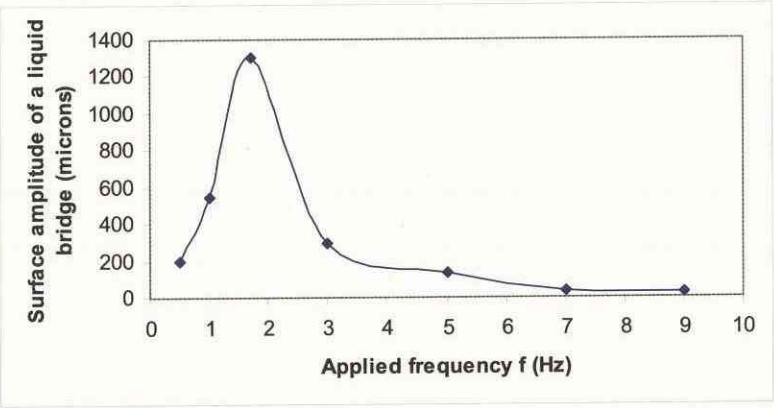

Fig. 18 Relation between the surface amplitude of a liquid bridge and applied vibration frequency under microgravity (D = 30.0 mm, H = 10.0 mm, Acceleration level = 5.0 mg; Computational resonance frequency = 1.7Hz, analytical resonance frequency=1.706Hz)

Part B.　Investigations for Low Prandtl Fluid

Oscillatory Marangon Flow in Half-Zone Liquid Bridge of Molten Tin

By
N. Imaishi[1], K. Li[1], S. Yasuhiro[1], S. Yoda[2]

Abstract: To evaluate the experimental observations at JAXA, a long-run numerical simulation was conducted on a realistic model of a half-zone liquid bridge of molten tin, which is identical to the apparatus of the JAXA's experiment. Using time dependent temperature difference imposed on both ends of the supporting rods, which is calculated based on the experimental temperature recordings measured through two thermocouples, the numerical results reproduce the experimentally observed oscillations of melt free surface temperature with different frequencies and explain the experimental results. The present study also indicates that very sensitive temperature measuring system must be developed to experimentally determine the critical conditions of Marangoni flow transitions through the melt free surface temperature measurements.

1. Introduction

Studies on stability of Marangoni flow in half-zone liquid bridges of low-Pr fluid are stimulated by the experimental fact that Marangoni flow instability in floating zones may cause striations in crystals grown in space [1]. It is well known that in half-zone liquid bridges of low-Pr fluid, Marangoni flow is axisymmetric and steady under a small temperature difference (ΔT). At a certain threshold value of ΔT (the first critical ΔT_{c1}), a transition to a three-dimensional steady Marangoni flow occurs. At a further higher threshold value of ΔT (the second critical ΔT_{c2}), a second transition to oscillatory Marangoni flow occurs. Many experimental studies were conducted on the Marangoni flow in half-zone liquid bridges over a wide range of Pr number. However, few [2-15] have been reported on low-Pr fluids due to the difficulties in conducting well-controlled experiments induced by the opacity, high reactivity with oxygen and high melting temperatures of the low-Pr fluids (mostly liquid metals). On the other hand, theoretical studies conducted on the Marangoni flow in half-zone liquid bridges of low-Pr fluid, both linear stability analyses [16-22] and direct numerical simulations [22-30], confirmed the two-step transition. In the numerical studies, a simple liquid bridge model was adopted, i.e., the liquid bridge was supported between two differentially heated isothermal discs and the calculation domain was restricted to the melt zone.

Recently, JAXA conducted on-ground experiments [31] on incipience of the oscillatory Marangoni flow in a small size liquid bridge of molten tin supported by iron rods. The imposed temperature difference on the liquid bridge was measured through two fine thermocouples mounted in the rods ($\Delta T'$). The thermocouple junction was located on the axis of the supporting rods with a certain distance (d = 0.5*mm*) apart from the melt/rod interface. By measuring the melt free surface temperatures at two different points through radiation pyrometers, the oscillations of melt free surface temperatures were successfully detected. However, the detected temperature oscillations are low with large amplitude. The frequencies are much lower than the critical frequencies predicted

---

[1]Institute for Materials Chemistry and Engineering, Kyushu University, Fukuoka, Japan
[2]JAXA, Sengen, Tsukuba, Japan

by the numerical simulations. Moreover, the critical Marangoni numbers based on $\Delta T'$ are larger than the numerical predicted ones by a factor of 1.5 to 2.0 . It is noted that for such a low-Pr fluid liquid bridge apparatus, the thermal conductivity of the supporting iron rods (k_r) is smaller than that of the molten tin (k). The large heat flux through the rods and melt zone may cause significant temperature drops even if the thermocouples position offsets (d) are small. So $\Delta T'$ may not correctly represent the effective temperature difference which drives the Marangoni flow. On the other hand, there remains a question about the observability of the critical point, i.e., the incipience of the oscillatory disturbances. In the experiment, the imposed temperature difference was gradually increased and the oscillatory disturbances started growth process after the critical condition was satisfied. Thus, the observed critical condition may substantially larger than the theoretical one. However, the above aspects have not been studied in detail so far except in our previous study on a liquid bridge of As = 2.0 [32].

In present study, a long-run numerical simulation was conducted on a realistic model of the half-zone liquid bridge of motlen tin to precisely review the JAXA experiment on a liquid bridge of As = 1.22 [31]. The numerical results reproduce the experimentally observed supercritical melt free surface temperature oscillations of different frequencies and explain the experimental results. The present study also gives the first and second critical Marangoni numbers and indicates that very sensitive temperature measuring system is necessary to be developed to detect the temperature oscillations right after the incipience of the oscillatory Marangoni flow experimentally. The numerical results are described in the dimensional form for the convienent comparison with the experiment results.

2. Problem statement

The schematics of the half-zone liquid bridge model adopted in the present study are shown in Fig.1. The gravity level is assumed to be zero because the dynamic Bond number of the liquid bridge in the experiment is smaller than unity, so the melt free surface is assumed to be non-deformable and cylindrical. A cylindrical coordinate system (r, θ, z) is adopted here with the origin of the coordinate located at the center of the lower melt/rod interface. The radius of the liquid bridge is R. The length of the melt zone is L and the length of iron rod is L_r. The thermocouple junctions are located on the axis of the supporting rods with certain distance d apart from the melt/rod interfaces. The aspect ratios are defined as: As = L/R, $As_r = L_r/R$ and $As_d = d/R$ respectively. The fluid being considered is molten tin of Pr = 0.009. It is assumed to be an incompressible Newtonian fluid with constant properties. With the above assumptions, the fundamental equations are expressed in dimensional form as follows:

In the liquid bridge:

$$\nabla \cdot \mathrm{U} = 0 \tag{1}$$

$$\frac{\partial \mathrm{U}}{\partial t} + \mathrm{U} \cdot \nabla \mathrm{U} = -\frac{1}{\rho}\nabla p + \nu \nabla^2 \mathrm{U} \tag{2}$$

$$\frac{\partial \mathrm{T}}{\partial t} + \mathrm{U} \cdot \nabla \mathrm{T} = \alpha \nabla^2 \mathrm{T} \tag{3}$$

In the iron rods,

$$\frac{\partial \mathrm{T}}{\partial t} = \alpha_r \nabla^2 \mathrm{T} \tag{4}$$

where $\mathbf{U} = (U_r, U_\theta, U_z)$ is the velocity vector, ν the kinematic viscosity, t time, ρ the density, p pressure, T temperature and α the thermal diffusivity for fluid, α_r the thermal diffusivity for rod respectively. The fluid is assumed to be motionless and isothermal before the temperature difference between the supporting iron rods is imposed.

The boundary conditions are defined as follows:
At the free surface of the liquid bridge (r = R):

$$U_r = 0, \quad \frac{\partial}{\partial r}\left(\frac{U_\theta}{r}\right) = -\frac{\sigma_T}{r^2 \rho\nu}\frac{\partial T}{\partial \theta}, \quad \frac{\partial U_z}{\partial r} = -\frac{\sigma_T}{\rho\nu}\frac{\partial T}{\partial z}, \quad \frac{\partial T}{\partial r} = 0 \tag{5}$$

At the surface of the rods (r = R):

$$\frac{\partial T}{\partial r} = 0 \tag{6}$$

At the upper and lower melt/rod interface (z = L and z = 0):

$$U_r = U_\theta = U_z = 0, \quad k\frac{\partial T}{\partial z} = k_r\frac{\partial T}{\partial z} \tag{7}$$

where k and k_r are the heat conductivity for the rod and melt respectively. A simple heat conduction dominant model [33] is employed to convert the thermocouple temperature recordings T_1 (thermocouple-1) and T_2 (thermocouple-2) to the time dependent temperatures imposed on the hot end (T_H) and cold end (T_C), i.e., the heat flux through the rods and melt zone is assumed to be one-dimensional in axial direction, steady and totally governed by heat conduction. The heat conduction dominant model gives the follows,

$$T_H = T_1 + \Delta T'\left(\frac{(L_r - d)}{\frac{k_r}{k}L + 2d}\right), \qquad T_C = T_2 - \Delta T'\left(\frac{(L_r - d)}{\frac{k_r}{k}L + 2d}\right) \tag{8}$$

where $\Delta T' = T_1 - T_2$. As mentioned above, $\Delta T'$ does not precisely represent the effective temperature difference driving the Marangoni flow, thus the effective temperature difference acting on the liquid bridge melt/solid interfaces is introduced as follows,

$$\Delta T_e = \left\{\int_0^{2p} T(R,\theta,0)\,d\theta - \int_0^{2p} T(R,\theta,L)\,d\theta\right\} \Big/ 2p \tag{9}$$

The Prandtl number and the Marangoni number referred in the present study are defined as:

$$\Pr = \frac{\nu}{\alpha}, \quad \mathrm{Ma} = -\frac{R\sigma_T \Delta T_e}{\rho\nu\alpha}.$$

3. Numerical methods

The governing equations are discretized by the finite difference method with a Kawamura scheme of third order accuracy for the convective terms [34]. Non-uniform staggered grids are adopted to increase the resolution near the boundary. The radial velocities at the central axis are calculated by the method of Ozoe et al. [35]. A fully implicit code is developed based on the preconditioned Bi-CGSTAB method [36]. The details of the numerical method can be found elsewhere [27-30]. In the present study, the total grid number is 27×63×94 ($N_r \times N_\theta \times N_z$), and 40 grids are placed in the z-direction of the melt zone. The numerical simulation was carried on a vector processor of Fujitsu VPP-5000. The thermophysical properties and geometric parameters for the liquid bridge model are listed in **Table 1**, which are identical to the experiment conditions.

4. Results

As shown in Fig.2, the experimental temperature recordings of the thermocouples are simplified to be linear with a constant heating velocity ($d\Delta\mathrm{T}'/dt = 0.34$ K/min, i.e., Case-1 hereafter), which is the same as the experimental averaged heating velocity. The temperatures at the hot and cold ends calculated by the heat conduction dominant model are also shown in Fig.2, and taken as the thermal boundary conditions for the simulation. To evaluate the effect of the heating velocity on the incipience of the critical conditions, the calculation with a faster heating velocity ($d\Delta\mathrm{T}'/dt = 2.04$ K/min, i.e., Case-2 hereafter) was also conducted.

For case-1, Fig.3 shows the evolution of maximum absolute value of the radial velocity at the axis ($\left|\mathrm{U}_{\mathrm{r(r=0,=0.5L)}}\right|_{\mathrm{max}}$, i.e., indicator velocity hereafter), which is the most sensitive parameter for current oscillatory transition, against the temperature difference between the hot and cold ends ($\Delta\mathrm{T} = \mathrm{T_H} - \mathrm{T_C}$). In the early stage, the temperature and flow fields are steady and axisymmetric with a small ΔT, and the corresponding azimuthal velocities of four monitor points at the melt free surface are zero (see Fig.4). When ΔT is increased, the amplitude of the indictor velocity increases gradually. At $\Delta T = 7.89$ K ($t = 303.5$ s), the azimuthal velocities of the monitor points start increasing quickly from zero indicating the growth of three-dimensional disturbance. The flow pattern change also results in the sudden decrease of the indicator velocity. When ΔT is further increased, the three-dimensional disturbance reaches the fully developed stage, and the azimuthal velocities decrease slowly. The corresponding three-dimensional temperature and flow fields are steady with the characterized azimuthal wave number $m = 2$ (see Fig.5), and maintained during the disturbance growth process. At $\Delta\mathrm{T} = 43.05$ K ($t = 1655.2$ s), the indicator velocity starts oscillation with a frequency of $f = 0.54$ Hz by FFT analysis (see Fig.6). As shown in Fig.7, its amplitude grows exponentially and its frequency increases to $f = 1.13$ Hz (It is noted that because of the absolute value function in the definition of the indicator velocity, soon after the incipience of the oscillatory transition, the frequency of the indicator velocity is two times of the corresponding frequency of the flow field oscillation). The corresponding oscillation mode is 2+1 [30], i.e., the superimposition of $m = 1$ type three-dimensional oscillatory disturbance on the three-dimensional steady flow $m = 2$. It results in an oscillatory radial velocity on the axis. Since $\Delta\mathrm{T} = 49.4$ K ($t = 1900$ s), the oscillatory flow reaches the fully developed stage. During the time period ($t = 1900 \sim 2100$ s), the amplitude of the indicator velocity is slightly increased as shown in Fig.6, and the corresponding frequency is nearly constant (see Fig.8). On the other hand, the fully developed flow oscillation induces the oscillation of the effective temperature difference between the melt/solid interfaces (see Fig.9). When ΔT is further increased, during the time period ($t = 2100 \sim 2156$ s), a new oscillation of $2T$ mode [30] appears, which produces the torsional oscillation (twisting) in the core of the flow. As shown in Fig.10, the $2T$ mode oscillation of low frequency ($f_l = 0.039$ Hz) enhances the oscillation amplitude of the indicator velocity, and modulates the 2+1 mode oscillation of relatively high frequency ($f_h = 0.72$ Hz). When the coexistence of two oscillation modes reaches the fully developed stage, the oscillation amplitude grows slowly, and the frequencies of the two oscillation modes gradually increase to $f_l = 0.05$ Hz and $f_h = 0.75$ Hz respectively (see Fig.11). Fig.3 also shows the evolution of indicator velocity against ΔT for case-2. The behavior of the two-step Marangoni flow transitions is similar to the case-1. The first and second bifurcation points are $\Delta\mathrm{T} = 10.61$ K ($t = 68$ s) and $\Delta\mathrm{T} = 44.7$ K ($t = 286.9$ s) respectively, and the occurrences of the bifurcations are delayed. It may results from the time lag between the imposed temperature difference and the developments of the temperature and flow fields under the relatively fast heating velocity.

Fig.12 shows the evolutions of the azimuthal velocities at the monitor point against the effective temperature difference (ΔT_e). For case-1, when the effective temperature difference (ΔT_e) is 1.14 K, the local azimuthal velocity starts growth, and the first critical Marangoni number is estimated as $Ma_{c1} = 15.68$. For case-2, the first critical Marangoni number is estimated as $Ma_{c1} = 20.19$ ($\Delta T_e = 1.47$ K). The second critical Marangoni number is determined through the indicator velocity. As shown in Fig.13, when ΔT_e is 5.95 K, the indicator velocity of case-1 starts oscillation with a frequency of $f = 0.54$ Hz by FFT analysis. The corresponding second critical Marangoni number is $Ma_{c2} = 81.7$. For case-2, the second critical Marangoni number is $Ma_{c2} = 84.4$ ($\Delta T_e = 6.15$ K), and the corresponding oscillation frequency is $f = 0.565$ Hz. Fig.12 also indicates that the definition of the incipience of the oscillation is always accompanied with some uncertainty due to the transient imposed temperature difference. Fig.14 summaries the critical Marangoni numbers of the liquid bridges of low Pr number fluids as the function of aspect ratio [27-30,32]. The results are given by the current realistic model and by the simple model corresponding to the marginal stability limits. It can be seen that small heating velocity is beneficial to the accurate prediction of the critical Marangoni numbers.

5. Discussions

It is worthy to be noted that in the JAXA's experiment [31], the melt free surface temperatures is measured by three radiation thermometers, and four thermocouples were inserted in the cold disk to reveal the details of the oscillatory flow transition. On the other hand, to evaluate the possibility of using the same thermocouple arrangement to detect the first flow transition, Fig.15 shows the temperatures at four monitor points located at the melt/solid interface periphery (r = R) of the cold end. It can be seen that the first transition point predicted through the free surface temperature bifurcations is identical to that of the local azimuthal velocity ($t = 303.5$ s, see Fig.4). Fig.15 also shows the relative deviations of the temperatures at the four monitor points from the expected linear temperature decrease for the axisymmetric flow respectively. Fig. 15 indicates that the asymmetric temperature field grows rapidly during the time period of $t = 303.5 \sim 340$ s. At $t = 340$ s, the maximum temperature difference becomes about 0.01 K, which may possibly be detected through thermocouples of high sensitivity.

In the previous section, the second critical Marangoni number ($t = 1655.2$ s, $Ma_{c2} = 81.7, f = 0.54$ Hz) is predicted through the indicator velocity, which is sensitive to the occurrence of the oscillation of 2+1 mode. Fig.16 shows that the local free surface temperature starts oscillations at $t = 1850$ s ($Ma = 90.6, f = 0.565$ Hz) suggesting there is a large time lag from the incipience of the indicator velocity oscillation. However, in the JAXA's experiment, the onset of oscillatory Marangoni flow was detected through measuring melt free surface temperatures. Due to the limited sensitivity (0.1 K) of the measuring instruments, only the free surface temperature oscillations with low frequency and large amplitudes can be detected experimentally. Fig.17 shows the time evolution of the local free surface temperature. It can be seen that the amplitude of the free surface temperature oscillations corresponding to the 2+1 type mode predicted numerically is much smaller than the sensitivity of JAXA's measuring instruments. Judged from Fig.17, the experimentally detected free surface temperature oscillation ($Ma_{c2} = 113, f = 0.02$ Hz) may correspond to the incipience of the coexistence of 2+1 and 2T oscillation modes ($t = 2120$ s, $Ma = 102.7, f = 0.039$ Hz), and the corresponding low oscillation frequency of the free surface temperature may correspond to frequency of the 2T oscillation. Thus the JAXA's experiment may not have detected the exact critical condition, and very sensitive detecting system must be developed to determine the critical Marangoni numbers.

6. Conclusion

In the present study, a long-run numerical simulation was conducted on a realistic model of half-zone liquid bridge of molten tin, which is identical to the JAXA's experimental apparatus, and the critical Marangoni numbers are predicted. However, the definition of the incipience of the three-dimensional disturbance is always accompanied with some uncertainties due to the transient imposed temperature difference. Small heating velocity is beneficial to the accurate prediction of the critical Marangoni numbers. Moreover, the second critical Marangoni number predicted through free surface temperature oscillation is much larger than the one through the indicator velocity oscillation. The experimentally predicted second critical Marangoni number and critical frequency through free surface temperature may be much different from those numerically predicted due to the sensitivity of the experimental detection technique. The exact incipience of the oscillatory Marangoni flow is not easy to be observed through the free surface temperature unless a very sensitive temperature measurement system can be developed.

References

[1] D. Schwabe, in: H.C. Freyhardt (ED.), Crystals, Vol. 11, Springer, Berlin, 1988, 75.

[2] J. H Han, Z. W. Sun, L. R. Dai, J. C. Xie, W. R. Hu, J. Cryst. Growth, 169, 129-135 (1996)

[3] M. Levenstam, G. Amberg, T. Carlberg, M. Andersson, J. Cryst. Growth, 158(3), 24-30 (1996)

[4] S. Nakamura, T. Hibiya, K. Kakimoto, N. Imaishi, S. Nishizawa, A. Hirata, K. Mukai, S. Yoda, T. S. Morita, J. Crystal Growth, 186, 85-94 (1998)

[5] T. Hibiya, S. Nakamura, K. Mukai, Z.G. Niu, N. Imaishi, S. Nishizawa, S. Yoda, M. Koyama, Philos. Trans. Roy. Soc. London, Ser. A 356 (1739), 899-909 (1998)

[6] T. Hibiya, S. Nakamura, Advances in Space Research, 24, 1225-1230 (1999)

[7] M. Cheng, S. Kou, J. Crystal Growth, 218, 132-135 (2000)

[8] M. Sumiji, S. Nakamura, K. Onuma, T. Hibiya, Jpn. J. Applied Physics, Part 1, 39, 3688-3693 (2000)

[9] T. Azami, S. Nakamura, T. Hibiya, S. Nakamura, J. Crystal Growth, 223, 116-124 (2001)

[10] M. Sumiji, S. Nakamura, T. Azami, T. Hibiya, J. Crystal Growth, 223, 503-511 (2001)

[11] T. Azami, S. Nakamura, T. Hibiya, J. Crystal Growth, 231, 82-88 (2001)

[12] M. Sumiji, S. Nakamura, T. Hibiya, J. Crystal Growth, 235, 55-59 (2002)

[13] T. Azami, S. Nakamura, T. Hibiya, J. Jpn. Soc. Microgravity Appl. (in Japanese), 18, 16-25 (2001)

[14] T. Hibiya, S. Nakamura, T. Azami, M. Sumiji, N. Imaishi, K. Mukai, K. Onuma, S. Yoda, Acta Astronautica, 48, 71-78 (2001)

[15] Y. K. Yang, S. Kou, J. Crystal Growth, 222, 135-143 (2001)

[16] G.P. Neitzel, K.T. Chang, D.F. Jancowski, H.D. Mittelmann, Physics of Fluids, A5, 108-114 (1992)

[17] H.C. Kuhlmann, H.J. Rath, J. Fluid Mech., 247, 247-274 (1993)

[18] M. Wanschura, V. Shevtsova, H.C. Kuhlmann, H.J. Rath, Physics of Fluids, 5, 912-925 (1995)

[19] G. Chen, A. Lizee, B. Roux, J. Crystal Growth, 180, 238-647 (1998)

[20] Q.S. Chen, W.R. Hu, Int. J. Heat Mass Transfer, 41, 825-837 (1998)

[21] Q.S. Chen, W.R. Hu, V. Prasad, J. Crystal Growth, 203, 261-268 (1999)

[22] M. Levenstam, G. Amberg, W. Christian, Physics of Fluids, 13(4), 807-816 (2001)

[23] R. Rupp, G. Mueller, G. Neumann, J. Crystal Growth, 97, 34-41 (1989)

[24] M. Levenstam, G. Amberg, J. Fluid Mechanics, 297, 357–372 (1995)

[25] J. Leypoldt, H.C. Kuhlmann, H.J. Rath, J. Fluid Mech, 414, 285-314 (2000)

[26] M. Lappa, R. Savino, R. Monti, Int. J. Heat Mass Transfer, 44, 1983-2003 (2001)

[27] N. Imaishi, S. Yasushiro, T. Sato, S. Yoda, SPIE Proc. Vol. 3792 (Material Research in low gravity II), 344-352 (1999)

[28] N. Imaishi, S. Yasushiro, T. Sato, S. Yoda, Proc. of the 4th JSME-KSME Thermal Engineering Conference (Kobe), vol.3, 277-282 (2000)

[29] S. Yasushiro, T. Sato, N. Imaishi, S. Yoda, Space Forum, 6, 39-47 (2000)

[30] N. Imaishi, S. Yasuhiro, Y. Akiyama, S. Yoda, J. Crystal Growth, 230, 164-171 (2001)

[31] K. Takagi, M. Ohtaka, H. Natsui, T. Arai, S. Yoda, Z. Yuan, K. Mukai, S. Yasuhiro, N. Imaishi, J. Crystal Growth, 233, 399-407 (2001)

[32] S. Yasuhiro, K. Li, N. Imaishi Y. Akiyama, H. Natsui, S. Matsumoto, S. Yoda, J. Crystal Growth, 266, 152-159 (2004)

[33] S. Yasushiro, N. Imaishi, Y. Akiyama, S. Fujino, S. Yoda, J. Crystal Growth, 262, 631-644 (2004)

[34] T. Suzuki, H. Kawamura, J. Mech. Eng. Japan (in Japanese), 60-578(B), 58 (1994)

[35] H. Ozoe, K. Toh, J. Crystal Growth, 130, 645-656 (1993).

[36] S. Fujino, K. Miura, Kokyuroku of Research Institute of Mathematical Sciences (Kyoto University) (in Japanese), No.1265, 162-172 (2002)

Table 1 Thermophysical properties and geometric parameters.

	Molten Tin	Iron
Pr	0.009	-
Density ρ [kg/m^3]	6793	7700
Thermal conductivity k [W/mK]	35.44	20.0
Specific heat C_p [J/kgK]	242	460
Viscosity μ [kg/ms]	1.318×10^{-3}	-
Temperature gradient of surface tension σ_T [N/mK]	-1.3×10^{-4}	-
Gravitational acceleration g_0 [N/m]	9.8	-
Volumetric expansion coefficient β [l/K]	1.3×10^{-4}.	-
Radius R [m]	3.0×10^{-3}	
Length of the liquid bridge L [m]	3.66×10^{-3}	
Length of rods L_r [m]	6.0×10^{-3}	
Offset of the thermocouple junction from melt/rod interface d [m]	0.5×10^{-3}	

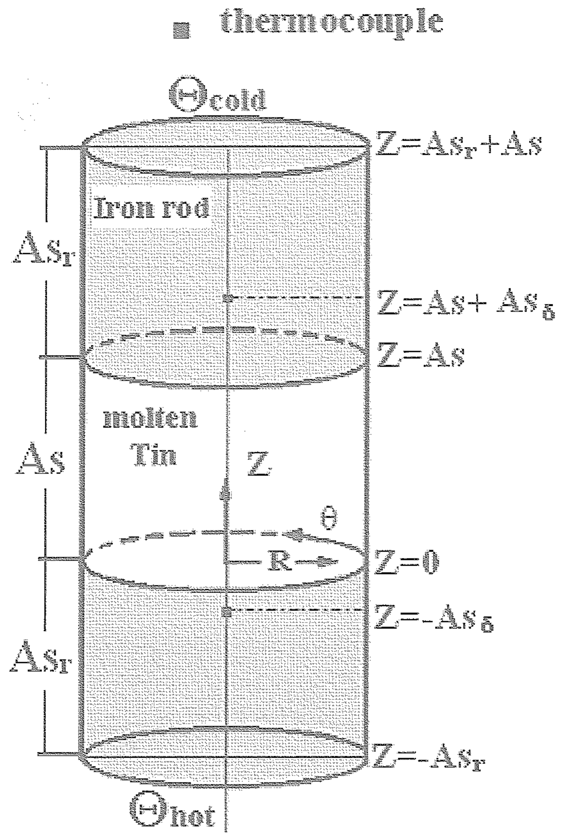

Fig.1. Schematics of the realistic liquid bridge model including the supporting iron rods.

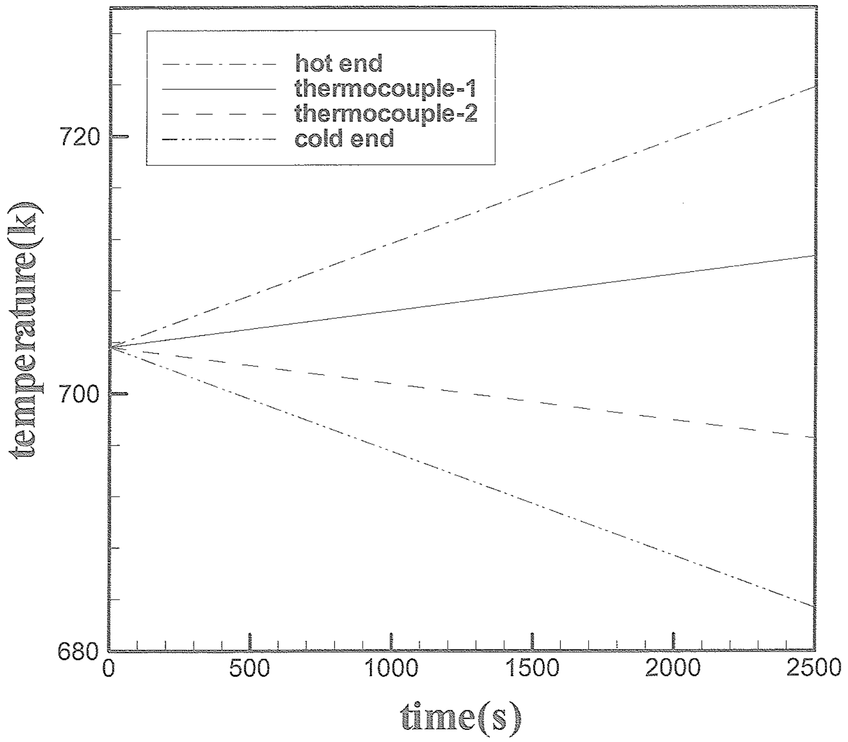

Fig.2. Time evolutions of the simplified linear thermocouple temperatures and the converted imposed temperatures at the hot and cold end.

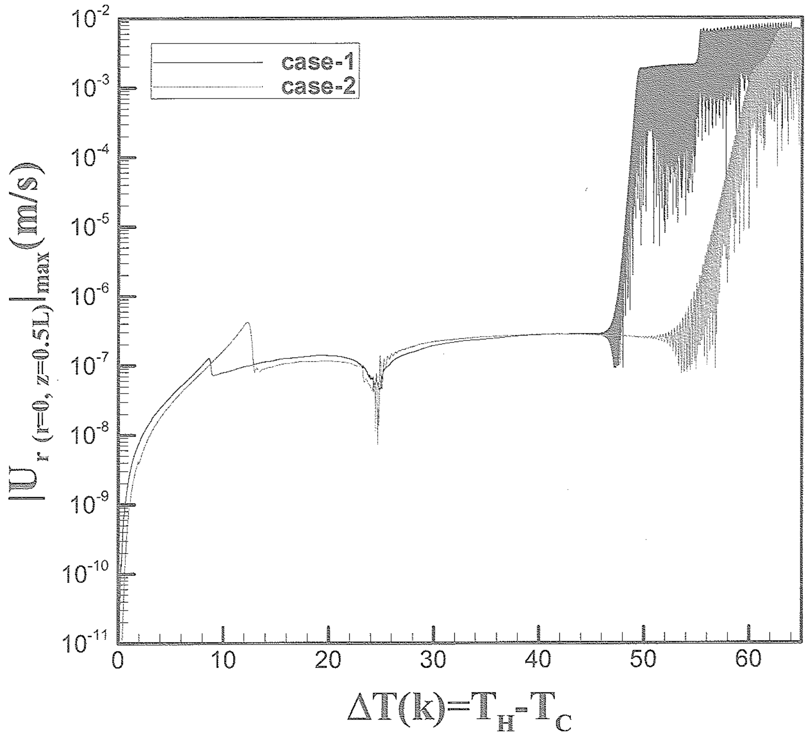

Fig.3 Evolution of the maximum absolute values of the radial velocity at the axis ($|U_{r(r=0,=0.5L)}|_{max}$) against the temperature difference between the hot and cold ends ($\Delta T = T_H - T_C$).

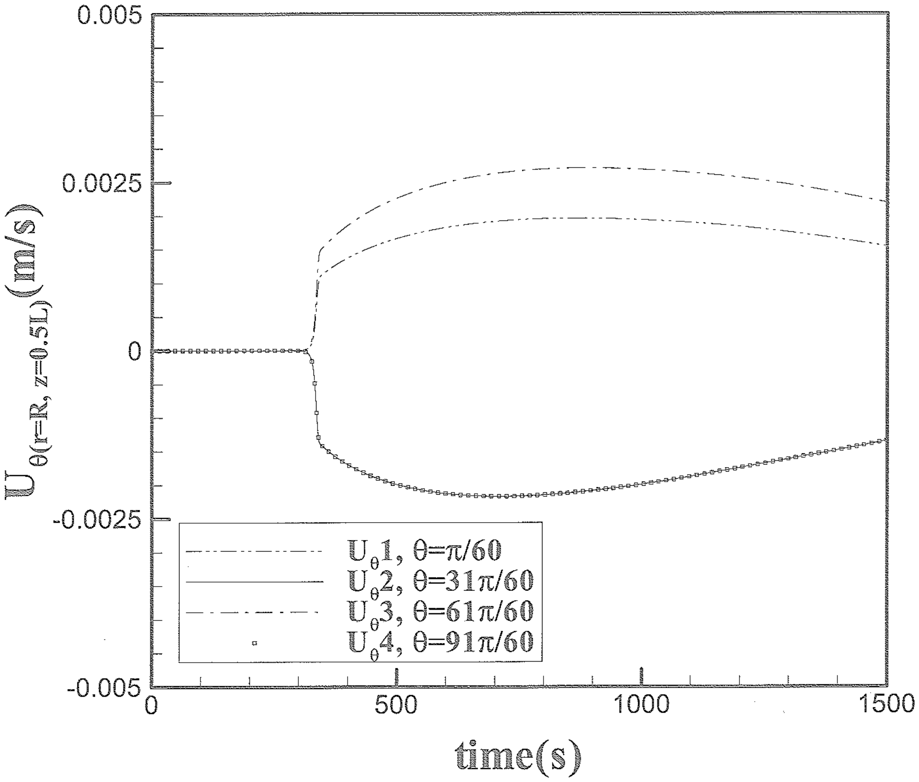

Fig.4. Time evolutions of the azimuthal velocity of the four monitor points at the melt free surface around the first critical point.

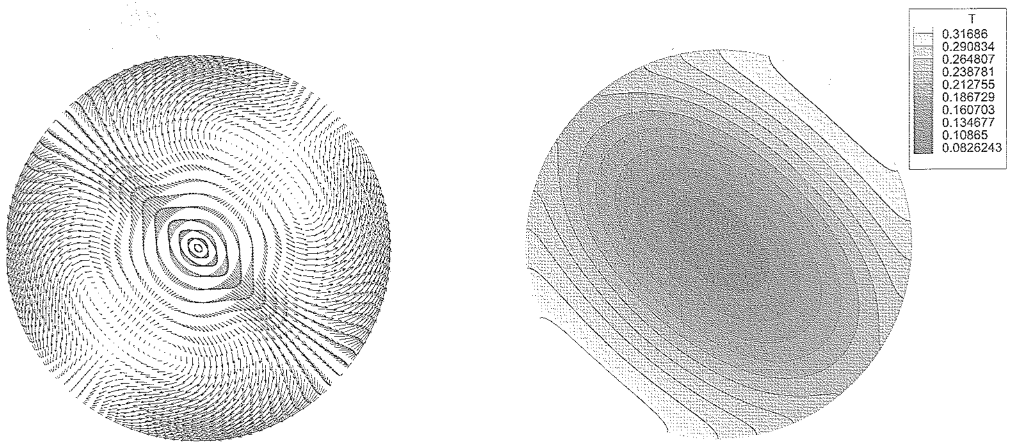

Fig. 5 Temperature and flow field cross sections (z = 0.5L) of the three-dimensional steady Marangoni flow of *m* = 2.

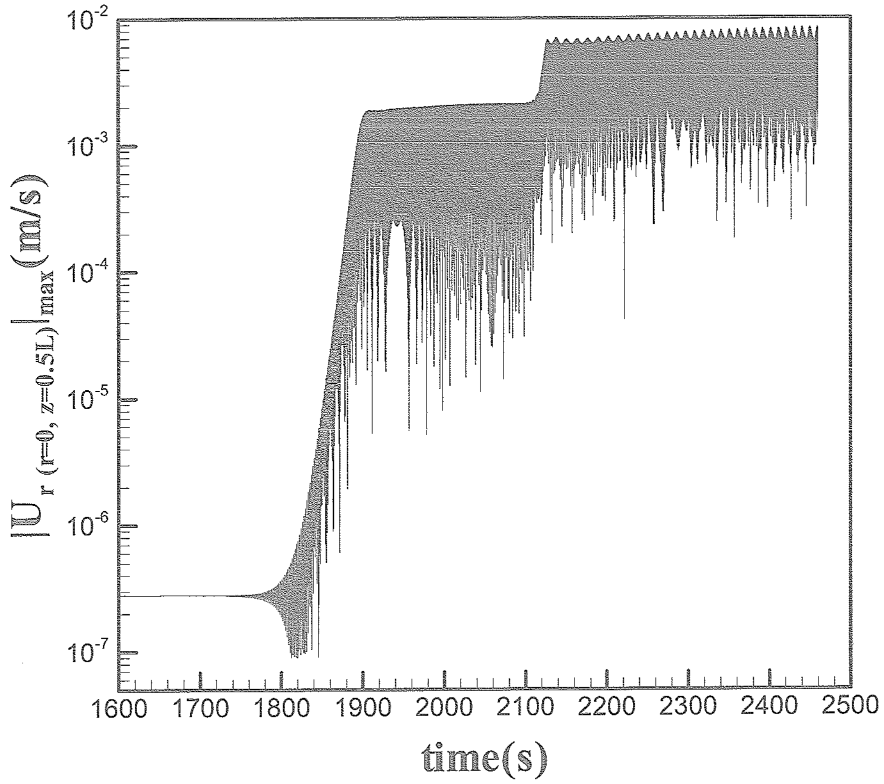

Fig.6. Time evolution of the maximum absolute value of the radial velocity at the axis ($\left|U_{r(r=0,=0.5L)}\right|_{max}$).

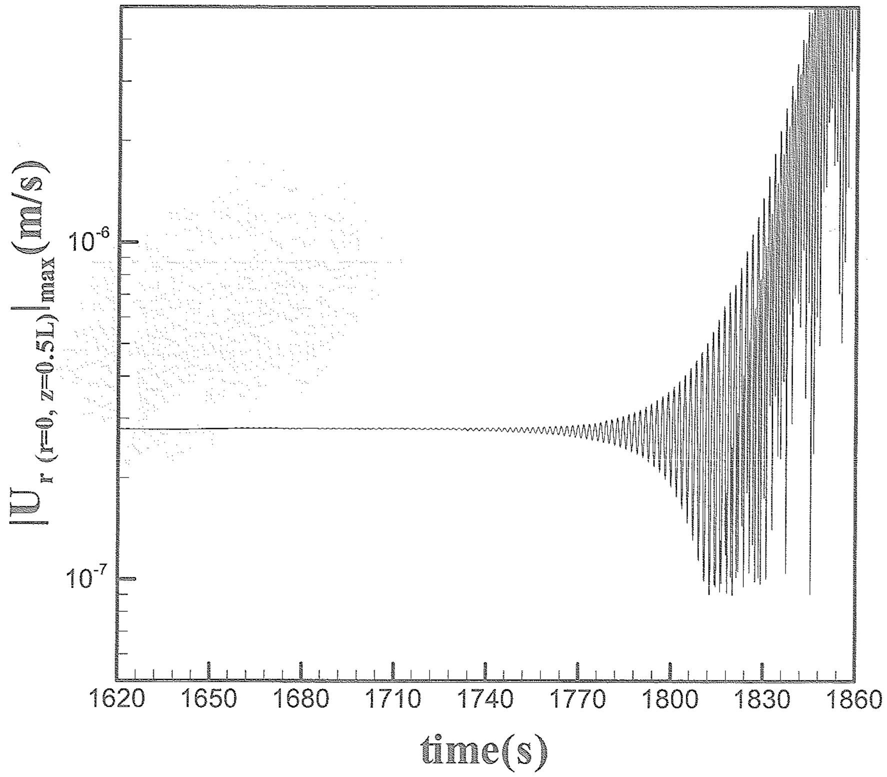

Fig.7. Time evolution of the maximum absolute value of the radial velocity at the axis ($|U_{r(r=0,=0.5L)}|_{max}$) around the second critical point.

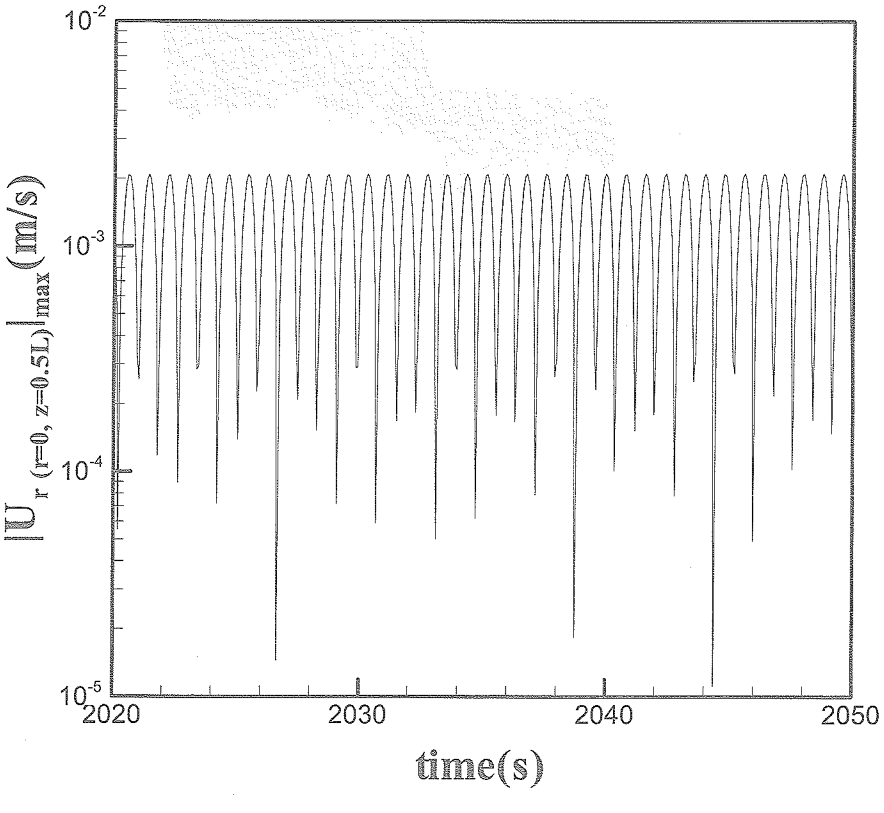

Fig.8. Time evolution of the maximum absolute value of the radial velocity at the axis ($|U_{r(r=0,=0.5L)}|_{max}$) for 2+1 oscillation.

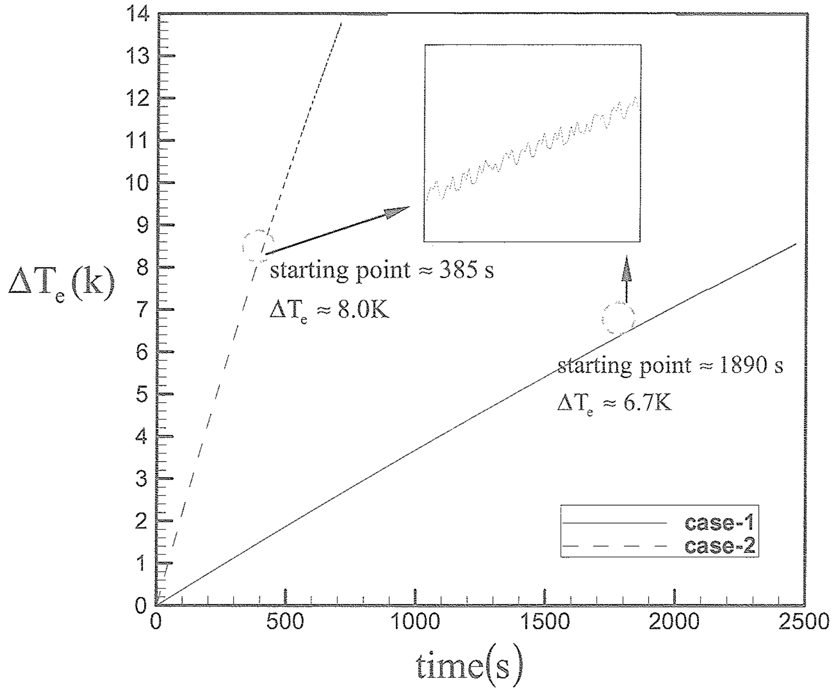

Fig.9. Time evolution of the effective temperature difference.

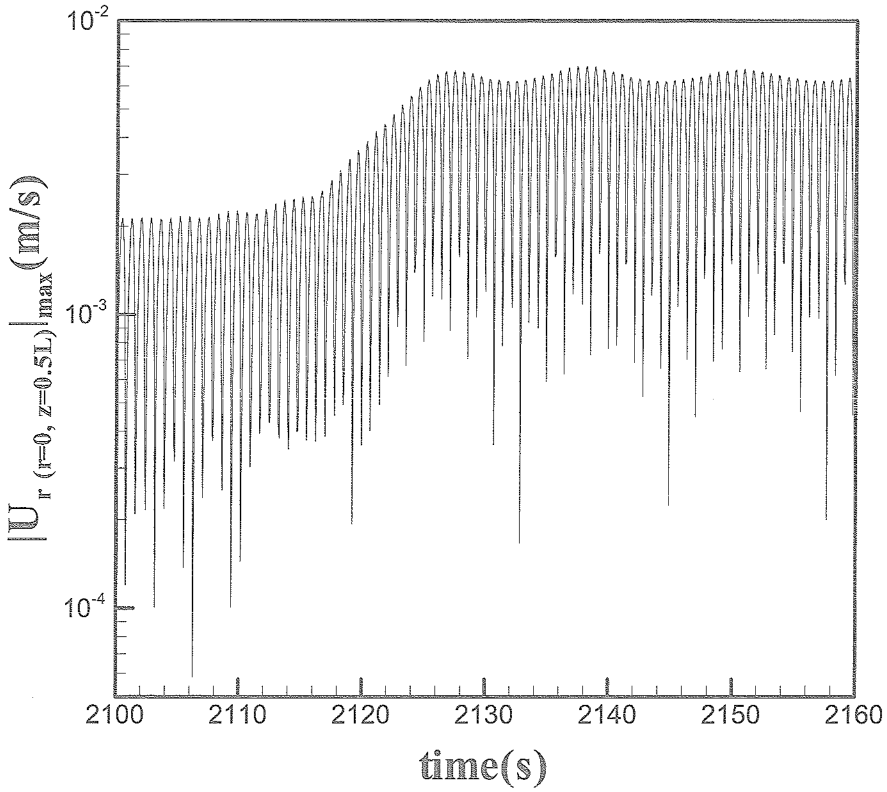

Fig.10. Time evolution of the maximum absolute value of the radial velocity at the axis ($\left|U_{r(r=0,=0.5L)}\right|_{max}$) for the transition from 2+1 oscillation to the coexistence of 2+1 and 2T oscillation.

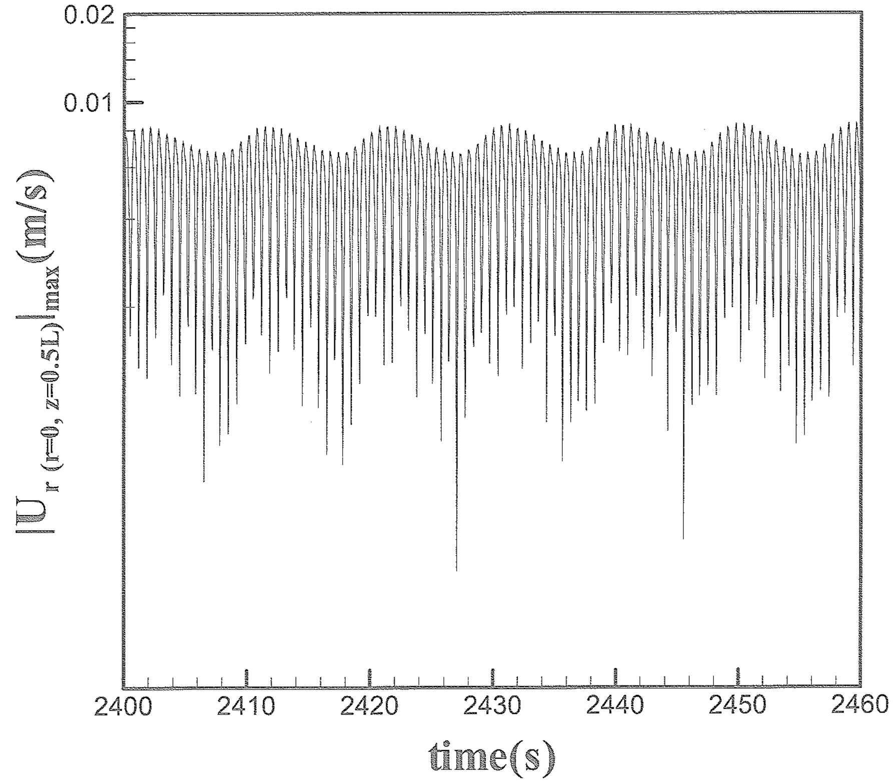

Fig.11. Time evolution of the maximum absolute value of the radial velocity at the axis ($\left|U_{r(r=0,=0.5L)}\right|_{max}$) for the coexistence of 2+1 and 2T oscillation.

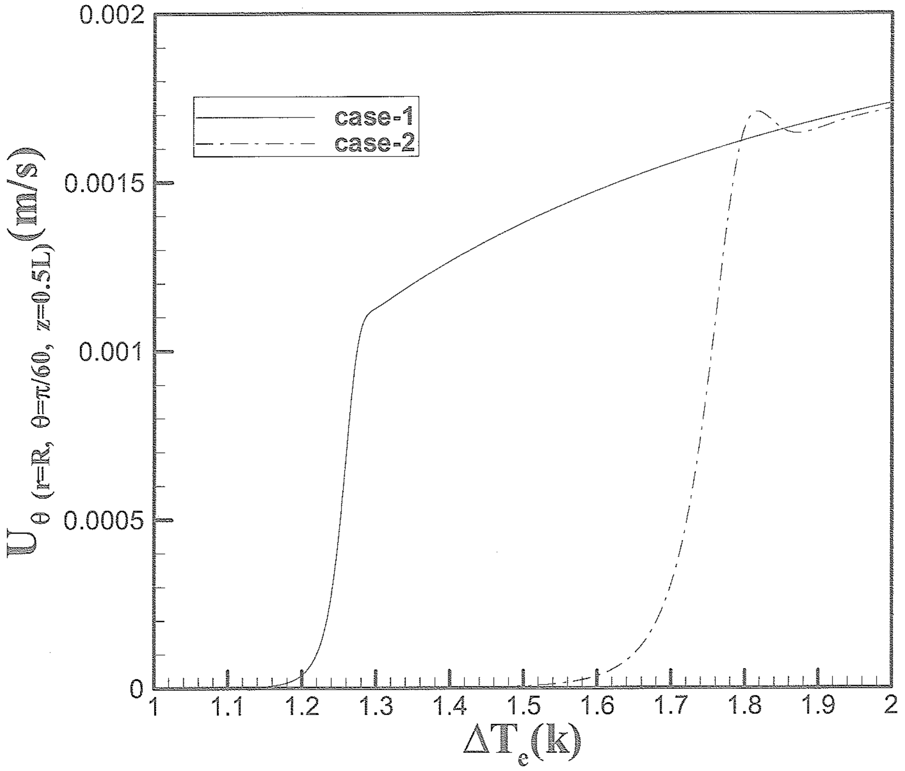

Fig.12. Evolutions of the azimuthal velocity of the monitor point at the melt free surface against the effective temperature difference around the first critical point.

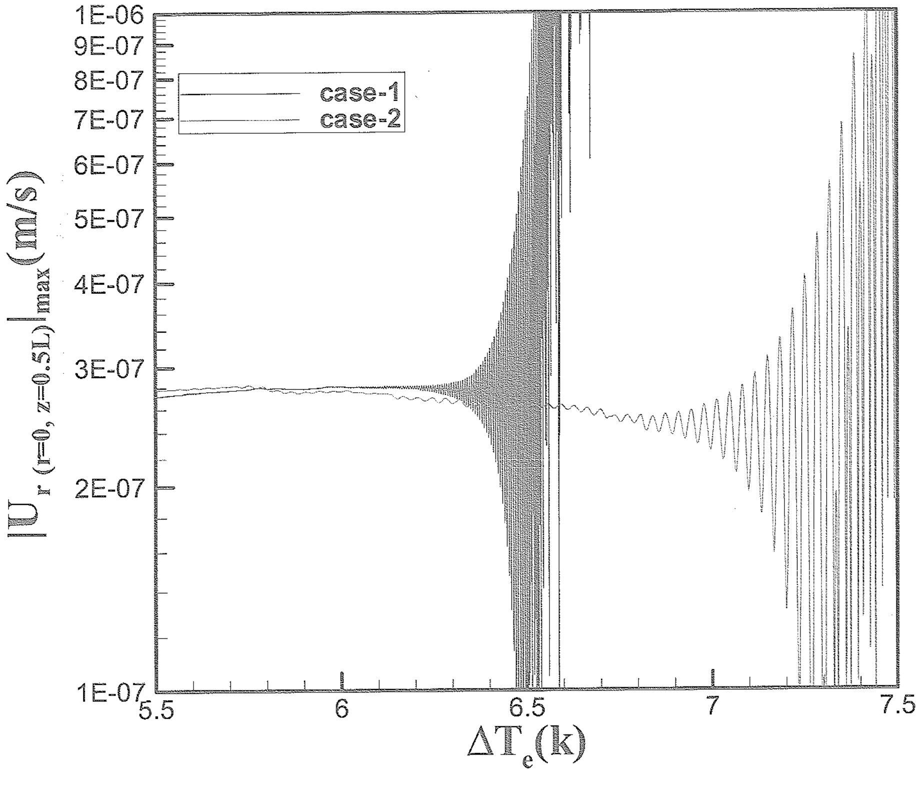

Fig.13. Evolutions of the maximum absolute value of the radial velocity at the axis ($|U_{r(r=0,z=0.5L)}|_{max}$) against the effective temperature difference around the second critical point.

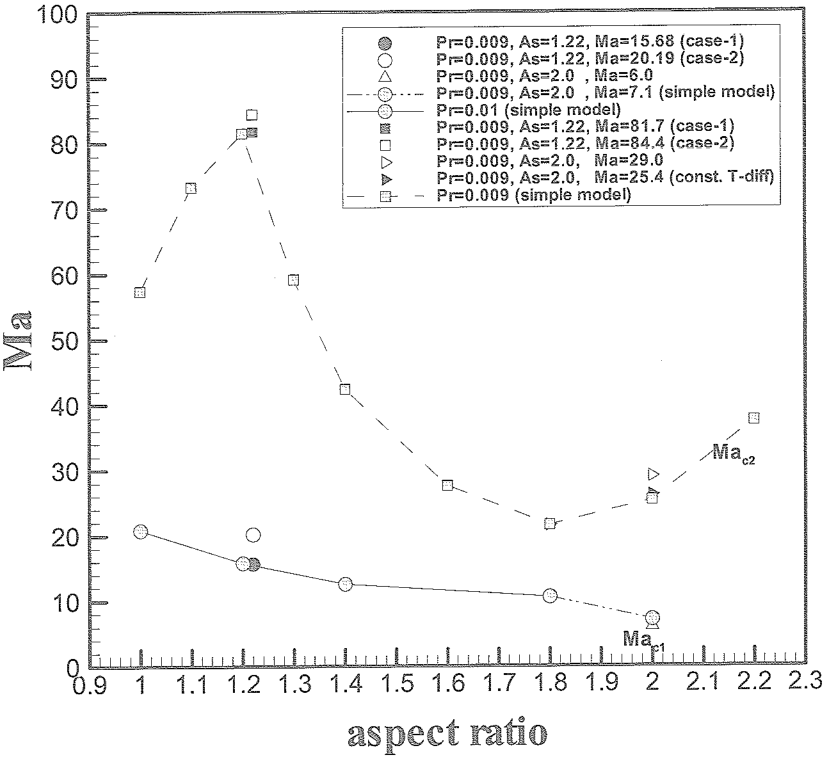

Fig.14. The critical Marangoni numbers of the liquid bridges of low Pr number fluids as the function of aspect ratio.

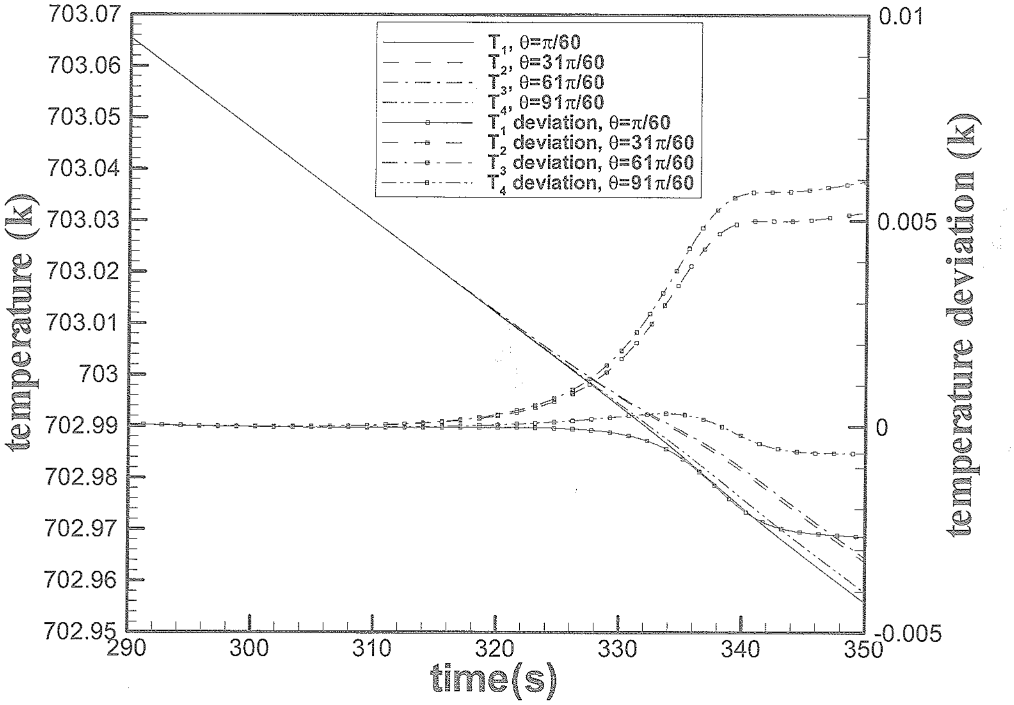

Fig.15. Time evolution of four monitor point temperature at the periphery of the melt/rod interface periphery on the cold side accompanied by the first flow transition.and their temperature deviations from the predicted temperature change for the axisymmetric flow system.

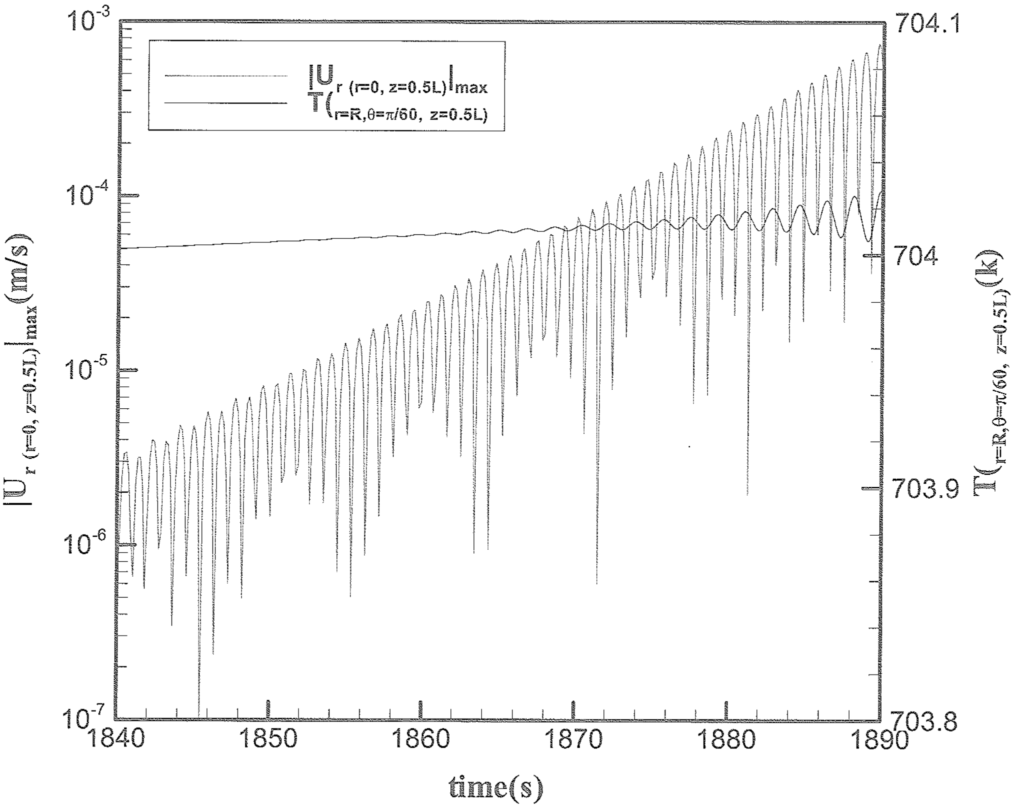

Fig.16. Time evolution of the free surface temperature of the monitor point at the melt free surface and the corresponding maximum absolute value of the radial velocity at the axis ($\left|U_{r(r=0,=0.5L)}\right|_{\max}$) around incipience of free surface temperature oscillation.

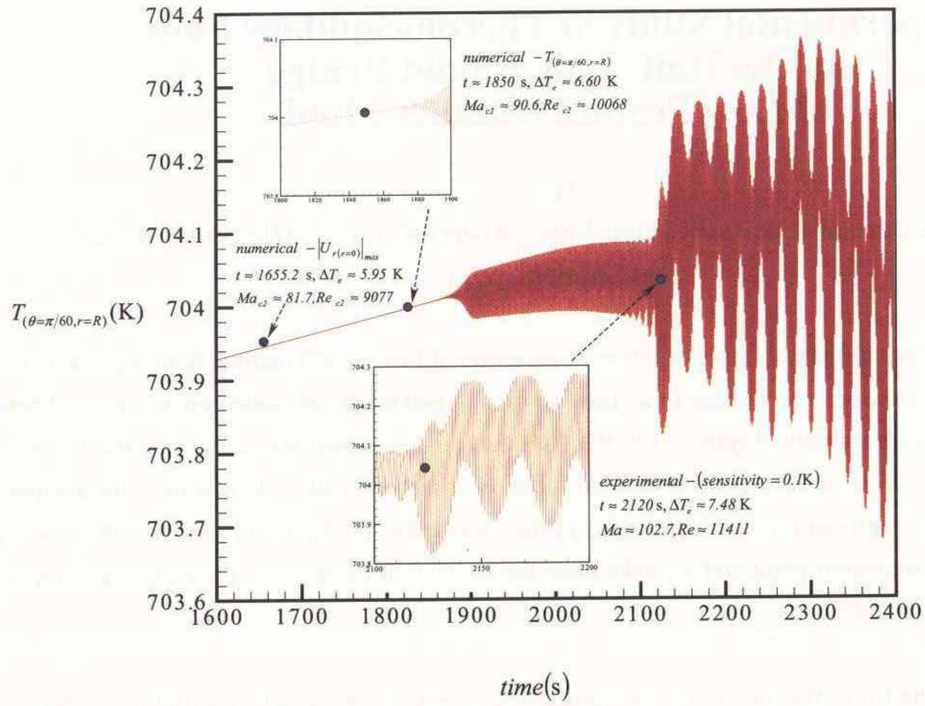

Fig.17. Time evolution of the free surface temperature of the monitor point at the melt free surface.

Experimental Study of Thermocapillary Flow in The Half-Zone Liquid Bridge of Low Prandtl Number Fluid

By

Satoshi Matsumoto[1], Hitoshi Hayashida[1], Atsuki Komiya[1], Hidesada Natsui[2],
and Shinichi Yoda[1]

Abstract: The experimental study on thermocapillary convection of low Prandtl number fluid was carried out to understand transition behavior to oscillatory flow. The half-zone liquid bridge of molten tin was formed between hot and cold disks in high vacuum chamber (10^{-5} Pa). The three radiation thermometers were used to measure the free surface temperature at a different azimuthal location at the same time. In addition, the temperature distribution at interface between liquid bridge and cold disk was measured by using very fine thermocouples. In order to detect the transition point and to make clear the oscillation mode more precisely, the temperature measurement system was developed.

It could be detected that the steady thermocapillary convection changes to oscillatory under certain condition. The observed phenomena of transition processes after the oscillatory onset were revealed by comparing to numerical result done by Imaishi *et al.*. The effect of aspect ratio (L/r) on critical Marangoni number was investigated. The critical Marangoni number decreases with increasing the aspect number. This behavior agrees with numerical simulation done by Imaishi *et al.* qualitatively except for region of smaller aspect ration.

Since the echo signal from the tracer had the very small bad SN ratio, in order to raise the SN ratio, signal processing technique was examined. Consequently, the noise which originates in the shoe by the subtraction processing technique was removable. And the SN ratio could be improved by the addition processing by repetition measurement, and the SN ratio improved about 3 times by calculation supposing actual measurement. The A/D converter and the system controller were manufactured in the 3D-UV measurement unit.

1. INTRODUCTION

It is well known that thermocapillary convection changes its flow motion by increasing the control parameters such as temperature difference. In the case of liquid bridge of low Prandtl number fluid, it is numerically predicted that an axisymmetric steady flow transit to asymmetric 3D steady flow. After that, convection becomes oscillatory under certain condition. Namely, the thermocapillary convection of low Prandtl number fluid go through two transition points to become an oscillatory flow. We need to understand the transition mechanism because the oscillatory flow has an undesirable effect on the crystal growth of semiconductors by the floating zone methods, which lead to striations of the dopant in the crystal. The previous studies, in which a

---

[1] Japan Space Exploration Agency, 2-1-1, Sengen, Tsukuba, Ibaraki 305-8505, Japan
[2] Advanced Engineering Services Co. Ltd., 1-6-1, Takezono, Tsukuba, Ibaraki 305-0032, Japan

half zone liquid bridge have been often used as a model configuration of the floating zone, have shown that flow and temperature fields were governed by dimensionless parameter of Marangoni (*Ma*) or Reynolds (*Re*) number defined as follows:

$$Ma \equiv \frac{|\sigma_T| \Delta T L}{\mu \kappa} \qquad (1\text{-}1),$$

$$Re \equiv \frac{Ma}{Pr} \qquad (1\text{-}2),$$

σ_T is a temperature gradient of surface tension, ΔT is a temperature difference between hot and cold disks, L is a characteristic length of the fluid, μ is dynamic viscosity, α is thermal diffusivity, and Pr is Prandtl number of the fluid. In this study, a radius (a) of the liquid bridge is used as a characteristic length.

In higher Pr number fluids, it was experimentally proved that a transition from axisymmetric steady to 3D oscillatory flow occurs at a critical Marangoni number (Ma_c). On the other hand, it was numerically predicted that thermocapillary flow in a low Pr number had two transition points [1], [2]: That is, transition from axisymmetric to 3D steady will occur at a first bifurcation point (Ma_{c1}), and transition from 3D steady to oscillatory at a second one (Ma_{c2}). The prediction needs to be experimentally proved.

A detail experiment around the bifurcation point, in which even the Ma_{c2} is predicted to be in the order of 10^1 for a $Pr = 0.01$ liquid bridge [3], is required to prove the transition behavior of Marangoni convection. However, many studies have been conducted at a Marangoni number that is far from the Ma_{c2} because those have mainly focused on a contribution to produce a high quality single crystal from a molten metal.

Nakamura et al. [4], [5] measured a surface temperature fluctuation with a thermocouple in a molten silicon column of 10mm in diameter and 10mm in length, and found that a frequency of the fluctuation was 0.1Hz at a temperature difference of 100K. However, the imposed temperature difference was far from the second bifurcation point. Han et al. [6] experimentally investigated thermocapillary convection in a liquid bridge of mercury. Free surface fluctuations were measured by a non-contacted diagnostic system, and they found the Ma_{c2}, detecting it to be 900 with a frequency around 5Hz. Quite recently, Yang and Kou [7] reported the onset point of temperature fluctuation and its frequency (Ma_{c2}=194 and 1.1Hz) of a molten tin column by the contacted diagnostic, *i.e.* J-type thermocouple. However, disturbances on the flow and temperature field are caused by a thermocouple which contacts with a fluid and a thermocouple often acts as a cold spot which makes it a complicated temperature gradient along a free surface. It should be noted here that there is no successful experiment to verify the transition behavior of thermocapillary flow by a non-contact diagnostic even nearby the Ma_{c2}.

The goal of present study is to understand the transition phenomena of thermocapillary flow by means of an experimental approach and comparative study with the numerical works in this research group.

The experimental efforts began to select a fluid material for a low Pr number liquid bridge in 1998 [8]. The selected material was molten tin of which Pr number is identical with that of molten silicon (Pr =0.01). Therefore, we can directly compare our experimental result with available experimental and numerical results of molten silicon because the identical Pr number means to show the same fluid dynamic behavior. Moreover, molten tin as a test fluid has an experimental advantage in a detection of Ma_{c2} compared to molten silicon. Since the melting point of tin is much lower than that of silicon, there is no need to use an infrared image furnace for melting a tin sample, which was used for a molten silicon experiment [4] and [5], and an electric heater is applicable to melt it. Thus, it is expected that the surface temperature of a molten tin column can be measured by a non-contact diagnostic with relatively low noise level. The high purity iron was selected as solid material to sustain a liquid bridge because of the reason that moderate wettability and low reactivity against molten tin is required for the solid material [8].

On the other hand, the selected test fluid has a thermodynamic disadvantage which the oxygen partial pressure is extremely low at the equilibrium between molten tin and tin oxides (SnO and SnO_2) near the temperatures for the low Pr experiment (about 570-770K), resulting in suppressing the thermocapillary flow by the formation of an oxide film over a surface of the melt. However, in 1999, we have successfully overcome the difficult problem of oxidation over the tin surface [9]. Consideration concerning the surface science of tin led us to design of a unique experiment apparatus where a clean surface of molten tin can be obtained by the Ar^+ ion etching method and sustained under the high vacuum condition (about 10^{-6} Pa) during an experiment. The performances of the experiment apparatus were already confirmed. In 1999, a non-contact measurement technique of the surface temperature has been also developed to detect small amplitude of temperature fluctuation at around the Ma_{c2} [9]. It was also confirmed that the radiation thermometer which is equipped with the PbS photo detector and combined with the attachments to obtain a high signal-to-noise ratio such as CaF_2 optical pass filter and an isotropic graphite panel had the sufficient temperature resolution to detect the Ma_{c2} with high accuracy. It was concluded that those unique considerations and devices undoubtedly lead us to a success of detecting the transition to oscillatory flow of the low Pr fluid without any flow disturbances.

Compared with the conventional transparent fluid used for a high Pr number experiment, a low Pr number fluid has another experimental difficulty: It is impossible to observe an internal flow field for opaqueness of a low Pr fluid. In order to overcome this problem, a novel visualization technique using an ultrasonic transducer with a high heat resistance has been experimentally studied for an internal flow field measurement since 1999 [9]. The visualization technique also requires a development of a unique balloon-like tracer. A critical condition on the Ma_{c1} and a detail structure of oscillatory flow will be clarified by this measurement technique.

The experimental results with molten tin obtained in 2000 are significant for the thermocapillary convection of a low Pr fluid. As predicted in the last issue [9], we have succeeded in detection of the transition to oscillatory flow by the surface temperature measurement without any flow disturbances. The flow transition was verified by comparison of the experimentally obtained Ma_{c2} and frequency of surface temperature fluctuation with the numerical results, and by a surface flow visualization experiment directly [10]. The effect of the liquid bridge geometry on the Ma_{c2} and oscillation frequency was further investigated and discussed [11]. The following results are described in this study:

(1) Experimental verification of surface temperature measurement (in-house activity)
(2) Detection of transition phenomena to oscillatory flow (in-house activity)
(3) Effect of aspect ratio on the critical condition and flow structure (in-house activity)

(4) Numerical simulation for the specific case (collaboration with Kyushu University)

(5) in-situ measurment of surface tension of the molten tin

(6) Development of measuring technique of internal flow field (entrusted to Toshiba Co.)

(7) Development of visualization tracer (collaboration with Kagoshima Prefectural Institute of Industrial Technology and partly entrusted to NTT Advanced Technology Co.)

2. TRANSITION PHENOMENA TO OSCILLATORY THERMOCAPILLARY FLOW OF MOLTEN TIN

2.1 Experimental Setup

The experimental apparatus is shown in Figs 2-1, 2-2, 2-3 [8,9,10]. It consists of a liquid bridge formation part, a measurement region, a sample supplying system and a sample cleaner. The liquid bridge was formed by sandwiching between a pair of pure iron disk (purity: 99.5%). All experiments were done in the ultra high vacuum conditions, which were under 10^{-5}Pa, to keep clean sample surface and less heat loss of molten tin liquid bridge. To impose the temperature difference, the lower disk was cooled by helium gas and the upper disk was heated by an electric resistant heater. The electric heaters were not controlled by PID (Proportional, Integral and Derivative) control to circumvent the temperature hunting phenomena. The temperature difference was gradually increased from around 0K to above the onset. An imposed ΔT was measured with the thermocouples embedded at near the end face of the disks.

Solid tin (purity: 99.999%) is melted in a quartz tube as illustrated in Fig. 2-2. The melt is supplied onto the lower disk *via* the capillary portion (1mm in inner diameter) of the quartz tube where bulk oxide in the crude fluid can be removed. For further purification, Ar^+ ion etching method was applied and the ion gun designed for surface cleaning was installed in the chamber. Surface temperature of the liquid bridge was measured with a radiation thermometer, in which PbS photo detector was installed, mounted on outside of the chamber.

The lower disk was optimized to measure the temperature field of liquid bridge as shown in Fig.2-3. The measurement of temperature field was necessary to understand the oscillatory thermocapillary convection. Because of the motion of temperature field was coincided with the one of oscillatory flow. It has been inserted some ϕ 0.3 mm K-type thermocouples (TC) sheathed a stainless steel in these 0.35 mm-holes. The top of thermocouples was adjusted the same position as lower disk plane.

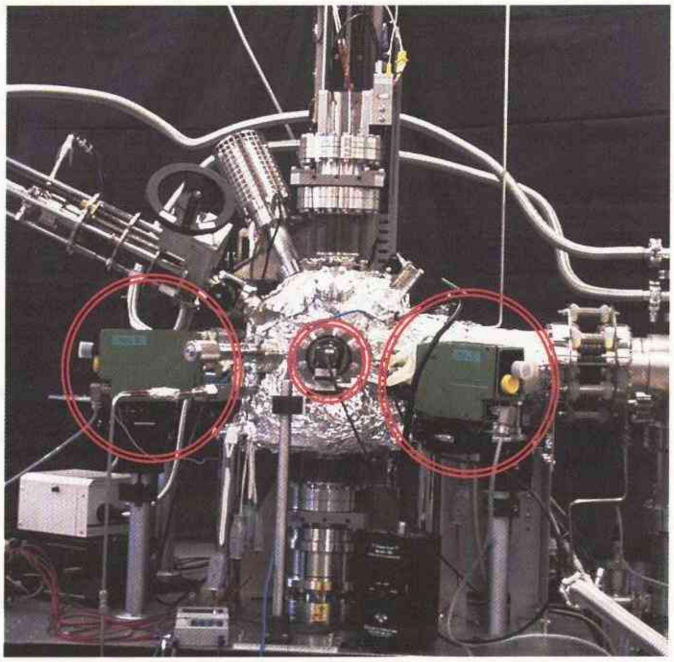

Fig. 2-1 Experimental equipment

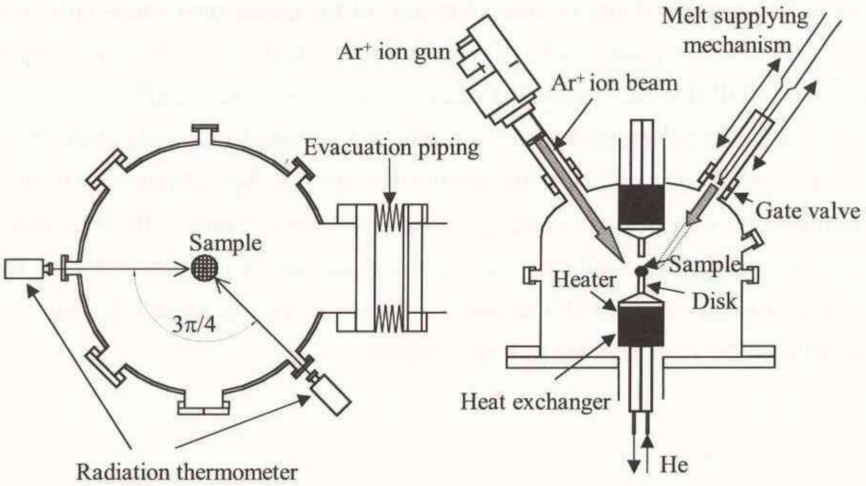

Top View

Side View

Fig. 2-2 Schematic diagram of experimental equipment

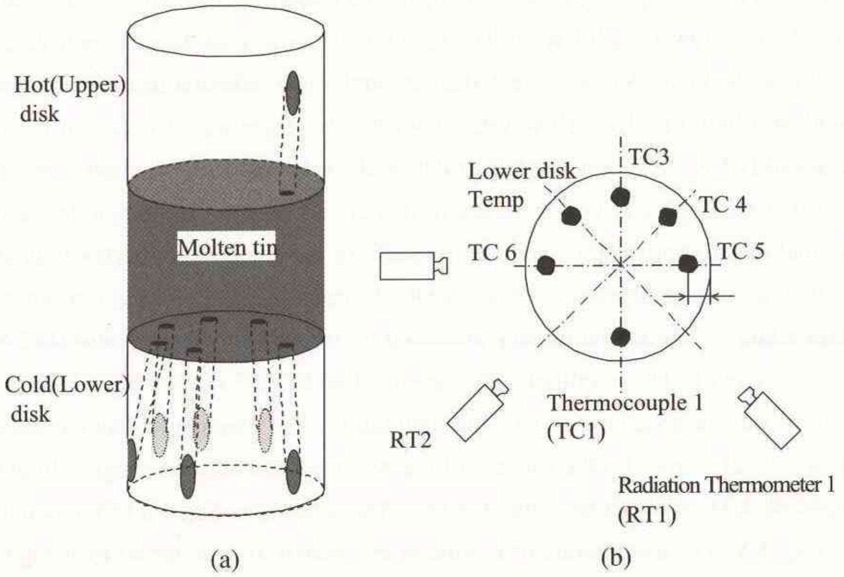

Fig. 2-3 Temperature measurement points
(a) Schematic diagram of tin liquid bridge and disks
(b) Lower disk surface and positions of radiation thermometers

2.2 Improvement of Experimental Techniques

(1) Purification of liquid bridge

The purity of formed liquid bridge is very important because an oxide on a free surface can change the surface tension. Therefore the purification of supplied molten tin should be done. As mentioned above, the experimental equipment already has a sample cleaner system, such as Ar^+ ion gun, high vacuum chamber, and sample supplying capillary tube. In addition of these, a stainless steel mesh filter was installed in the capillary tube last year. It can stain off the crude fluid, which is mainly oxide, from supplying molten tin. The capillary tube for sample supplying system is shown in Fig.2-4. Molten tin flows from left fat to right thin parts. In the case of no filter, a white powder-like sludge adhered on the inwall of slim part of capillary tube. On the other hand, the mesh filter worked very efficiently, because no sludge can be found below the filter in Fig. 2-4. Consequently, the liquid bridge could be refined.

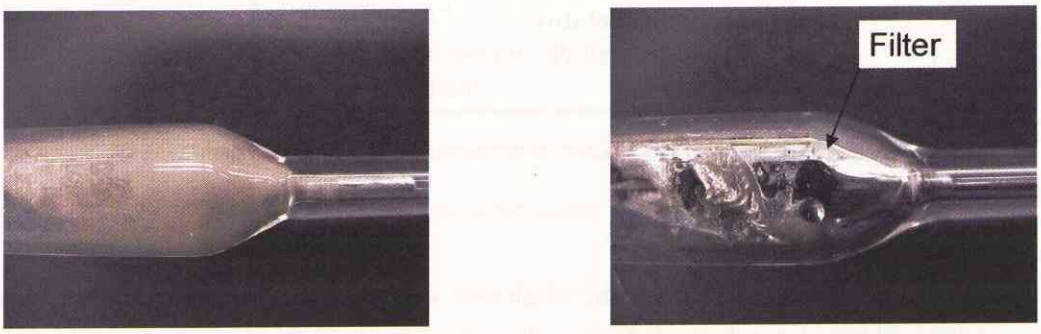

(i) without filter (ii) with 0.1 mm mesh filter

Fig. 2-4 Improvement of sample supplying tube

2.3 Improvement of temperature measurement system

In case of low Prandtl thermocapillary flow, the temperature change or fluctuations at transition points is very small (eg. 0.01 K for the first transition, 0.1 K for the second transition). Therefore, the sensitivity of temperature measurement system must be high. As mentioned, thermocouples and radiation thermometers are used to detect the temperature field of a liquid bridge. However, a temperature resolution of radiation thermometer used in this experiment is about 0.3 K. It is not enough to detect fluctuations. So, we used several thermocouples. Output signal from thermocouples is very tenuous in this case. E-type thermocouples that could produce relatively large thermal electromotive force were employed. In this experiment higher temperature resolution is important rather than absolute temperature. Such weak electromotive force of thermocouples was amplified. The voltage corresponding to thermocouple was produced by the DC signal generator (DC-SG). The signal from thermocouple was input to DC amplifier with the signal of DC-SG differentially in order to remove DC component. This signal was increased to 5×10^4 times amplitude. The frequency of temperature fluctuation was estimated in order of several Hertz. So the low-pass filter was used to reduce the higher frequency noise. The signals were digitized by A/D converter and stored in PC. The schematic diagram of temperature measurement system is shown in Fig. 2-5. The temperature resolution of less than 0.01 K achieved by using this measurement system.

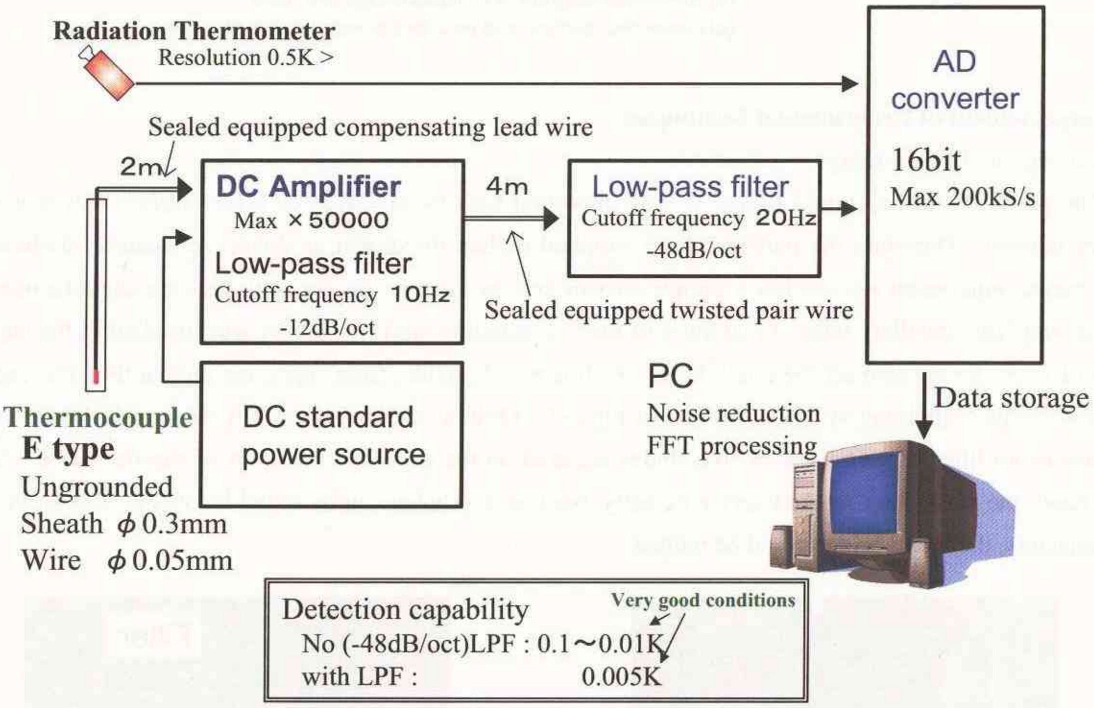

Fig. 2-5 Schematic diagram of temperature measurement system

2.4 Observation of first transition

Fig. 2-6 shows time variations of temperature which were measured by three thermocouples located in cold disk. Temperature suddenly jumped around 1510 s. Since there could not be any oscillatory behavior after the temperature jump, this seems to be the first transition point which have been predicted by numerical simulation. In this case, aspect ratio of liquid bridge was 1.8, a temperature difference, ΔT, was 1.7 K, and Marangoni number was 11. From the relation between thermocouple position and temperature change, the mode structure seems to be unity and the cold spot located in the center of liquid bridge near cold disk moved to peripheral region as shown in Fig. 2-7.

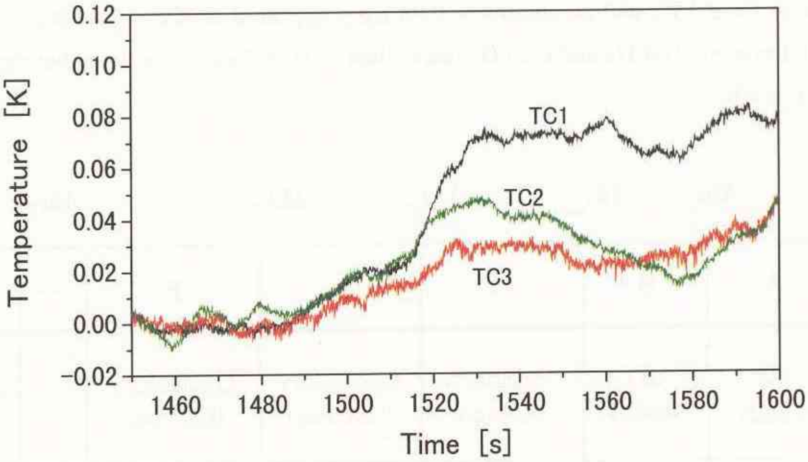

Fig. 2-6 Time variation of temperature at first transition point

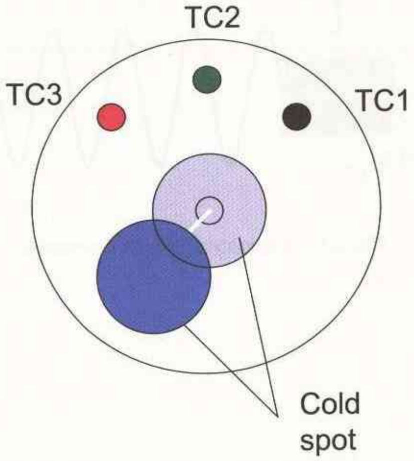

Fig. 2-7 Schematic of mode structure and movement of cold spot near cold disk

2.5 Transition process of oscillatory flow

It was estimated by numerical simulation that several transitions occur after the onset of oscillatory flow. We divided each region as shown in Fig. 2-8. The onset of oscillation is called the second critical Maragoni number Ma_{c2} or $Ma_{c2\text{-}1}$. The transitions after $Ma_{c2\text{-}1}$ were named $Ma_{c2\text{-}2}$ and $Ma_{c2\text{-}3}$ sequentially. In previous experiment, $Ma_{c2\text{-}1}$ could not detect because its signals was very small. Improvement of temperature measurement method provides us precise observation of just onset point.

An oscillatory transition was detected with larger temperature difference after an occurrence of first transition. The temperature fluctuation measured by thermocouple is shown in Fig. 2-9. At first, relatively higher frequency fluctuation with a frequency $f = 1.2$ Hz appeared at $Ma_c = 43$ (see Fig. 2-9 (i)). The amplitude of this fluctuation was about 0.1 Kp-p (Peak to Peak). It was considered that this transition was the second critical point since the frequency was same order of numerical result which was 2.5 Hz. In this case, Mac2-2 could not detected. In Fig. 2-9 (ii), (iii), the lower and middle frequency fluctuations were depicted in case of As=1.2. The lower frequency with f = 0.02 Hz and an amplitude 0.4 Kp-p appeared at Ma = 82 ($Ma_{c2\text{-}2}$). The middle frequency with f = 0.3 Hz and an amplitude 0.08 Kp-p appeared at Ma = 125 ($Ma_{c2\text{-}3}$). The frequencies by numerical simulation were 0.04 Hz and 0.25 Hz respectively. Therefore, we believe that the transition process was detected very precisely.

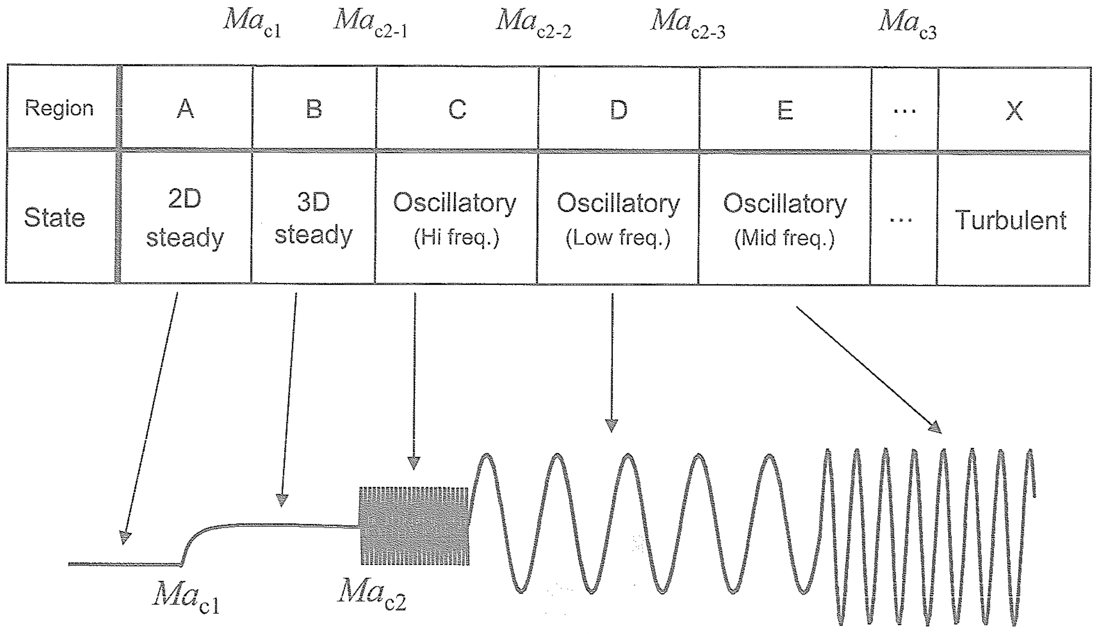

Region	A	B	C	D	E	…	X
State	2D steady	3D steady	Oscillatory (Hi freq.)	Oscillatory (Low freq.)	Oscillatory (Mid freq.)	…	Turbulent

Fig. 2-8 Estimated transition process

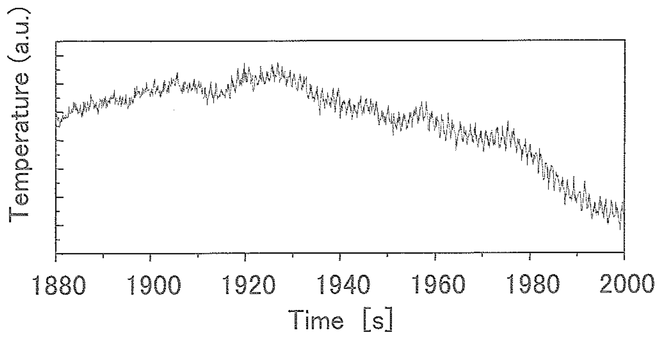

f~ 1.2 [Hz] (Exp.)
2.5 [Hz] (Simulation)

(i) Higher freq.

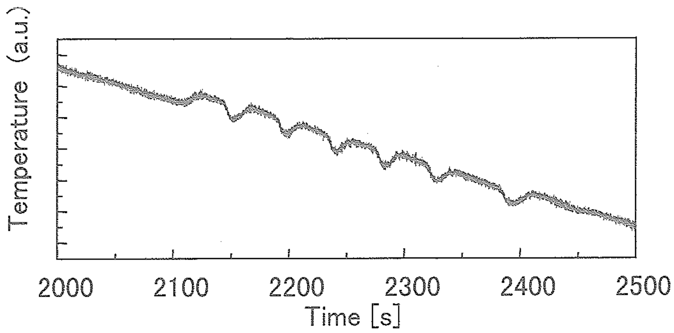

f~ 0.02 [Hz] (Exp.)
0.04 [Hz] (Simulation)

(ii) Lower freq.

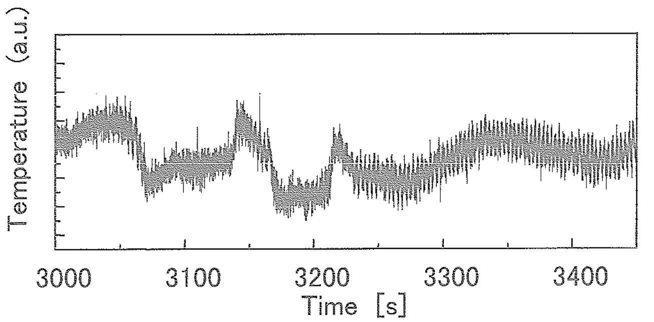

f~ 0.30 [Hz] (Exp.)
0.25 [Hz] (Simulation)

(iii) Middle freq.

Fig. 2-9 Detected temperature fluctuation

2.6 Effects of aspect ratio

(1) Experimental conditions

The disk diameters from 3.0mm to 7.0mm were used in order to covering liquid column with aspect ratio (*As*: height/radius) from 0.8 up to 2.2. This range almost corresponds to calculated range of numerical simulation by Imaishi *et al.* [13]. Heights of the liquid column were adjusted in from 1.5 mm to 4.5 mm at all the experimental cases, minimizing the dynamic bond number *Bd* (*Bd*<1).

$$Bd \equiv \frac{\rho\, g\, \beta\, L^2}{\sigma_T} = \frac{Ra}{Ma}$$

where ρ, is density, g gravitational acceleration, β volumetric expansion coefficient, σ_T temperature gradient of surface tension, L the height of the liquid column and Ra is Rayleigh number. However the static bond number B_o is larger than unity, volume ratio or diameter ratio (D/D_{max}), surface shape is almost straight.

$$B_0 = \frac{\rho\ g\ L^2}{\sigma}$$

In every case, temperature difference (ΔT) was imposed at certain changing rate. In some cases, ΔT was reduced after transition in order to measure surface temperature behavior when damping. Since the control of changing rate of ΔT (dΔT/dt) is very difficult, there were some widths on them. Influence of ramping rate of temperature difference, dΔT/dt on transition was discussed in previous report. The dΔT/dt ranging from 0.4 to 2.1 K/min has no influence in the critical Marangoni number. Therefore we controlled the dΔT/dt around 0.5 K/min.

(2) Ma_c as a function of aspect ratio

In order to make clear the influence of aspect ratio on Ma_{c2}, the onset of oscillatory thermocapillary flow using liquid columns with As from about 0.8 to 2.2 are investigated. In the case of experimental work in this case, Ma_{c2} is determined by the temperature difference at the onset of low frequency oscillation. It seems reasonable because the Ma_{c2} at the second transition point was slightly 10 % higher than the first point.

The Ma_{c2} as a function of As, which was experimentally and numerically obtained by Imaishi *et al.* [13], are shown in Fig. 2-10. The estimated oscillation mode is also described in this figure. The experimental Ma_{c2} in the range of As higher than about 1.2 well corresponds to numerical one. The experimental Ma_{c2} increases with decreasing of As monotonically. In contrast, the numerical Ma_{c2} has a peak at $As = 1.2$ and the one slightly decreases when As in the range of $1.0 = As = 1.2$ decreases. The experimental results showed that the Ma_{c2} ($As = 1.3$), which was obtained using the liquid column with relative large radius and the one lied on relative low Marangoni number, was obtained by the experimental conditions at small dΔT/dt. We will make clear the reason why the experimental critical Marangoni number in the smaller aspect region differs from the numerical result in near future.

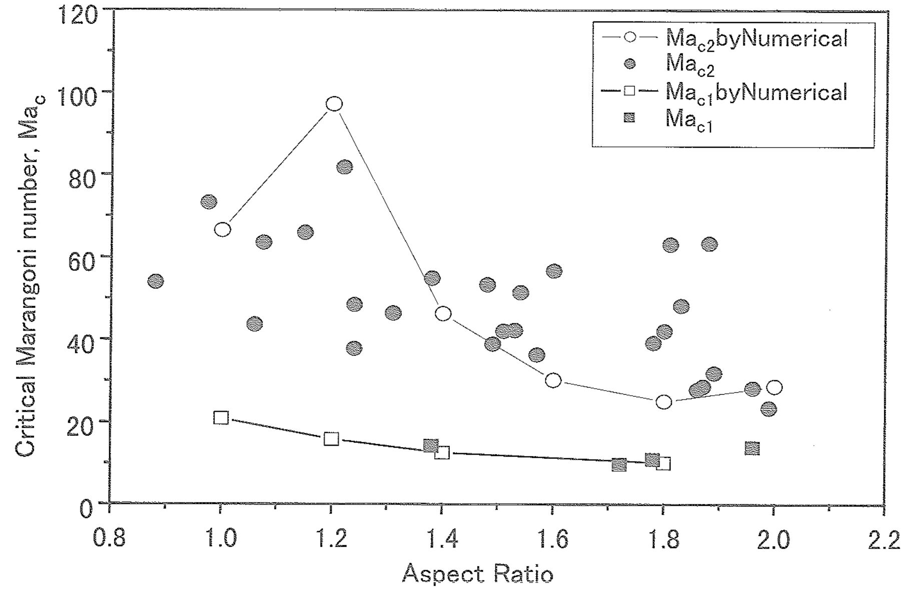

Fig.2-10 Dependence of Marangoni number on aspect ratio

3. DEVELOPMENT OF 3D-UV AND TRACER PARTICLE

3.1 Development of 3D-UV

In 1999, a test for evaluating delectability of $LiNbO_3$ (LN) transducer was performed at room temperature using a drilled glass target, which simulated balloon tracers in molten tin. It was predicted that a detectable minimum diameter of tracer was 100-200 μm [9].

In 2000, a test for evaluating sensitivity of transducer at high temperature conditions same as actual thermocapillary experiment was performed in molten tin. High spatial resolution was obtained in the direction of wave propagation. Numerical simulation was performed in order to check visualization performance of ongoing sensor-design. It was confirmed that tracers in molten tin liquid bridge could be visualized [17].

In 2001, the transducer with 3 × 3 LN element was made and checked its sensitivity. The sensor was verified the stability after heat treatment up to 500 °C which is same as actual thermocapillary experiment. The frequency band of oscillator was selected to get the clear echo signal. The optimal frequency was 6 to 14 MHz wide-band. [18].

In 2002, the Fe-Ni/SB plating practical tracer was manufactured and coexistence nature with melted tin was checked in actual thermocapillary condition. By C-scan probe measurement, the ultrasonic echo from the particle in tin [19].

3.1.1 Study of the signal processing technique

The Fe and Ni plated Shirasu-ballons (Fe-Ni/SB) which is the tracer particle used by this 3D-UV system is very small. Therefore, the reflective echo signal measured is a very low level. Moreover, a shoe is attached in the transducer in order to protect an LN element to the molten tin. While the echo measured with a shoe declines, the sound noise by the inside reflection of a shoe is added. For realization of 3D-UV system, it becomes very important to acquire the echo signal from the tracer by sufficient the signal to noise (SN) ratio. Then, the signal processing technique for extracting the echo signal was studied.

An example of the echo from the imitation tracer in molten tin in the 1999 fiscal year (hollow stainless steel ball) is shown in Fig.3-1. The imitation tracer was moved in molten tin and the echo was measured. Fig.3-1 showed time series data and average value. In this result, the echo is hidden by the noise and distinction of it is clearly impossible.

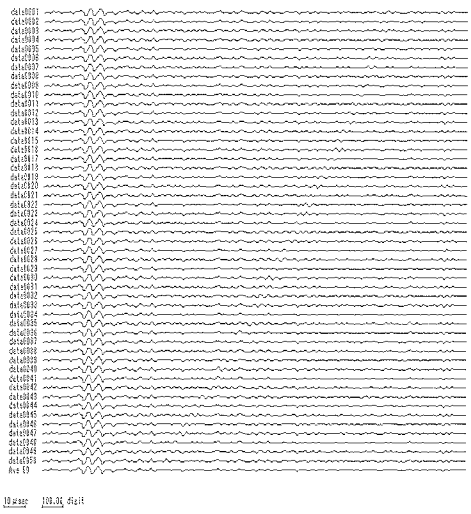

Fig.3-1 The echo from the tracer obtained by the test using molten tin

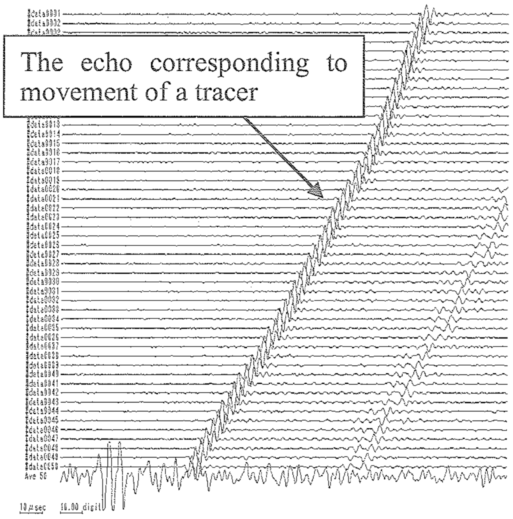

The echo corresponding to movement of a tracer

Fig.3-2 The result of subtraction processing

Therefore, it is necessary to raise SN ratio by signal processing, and to extract the echo. The result which removed the noise from the shoe by signal processing is shown in Fig.3-2. Subtraction processing of the noise was carried out from the echo, and the SN ratio was raised. The average value of the echo of much measurement was made into the noise resulting from the shoe.

Next, the improvement effect in the SN ratio by other techniques was examined. The speed of the ultrasonic wave used for 3D-UV is very high-speed compared with the move speed of the tracer. Then, if much measurement with a short repetition cycle is performed and addition processing is carried out, improvement in the SN ratio will be attained. In repetition measurement, a difference arises in the echo waveform measured by movement of the tracer for every measurement. Then, the numerical simulation considered the influence of echo signal change. In calculation, the tracer echo waveform was created using the sin wave of two cycles, and the imitation noise was created from the random number. And addition processing of the 100 data which mixed and made the echo and the noise was carried out. Moreover, it was assumed that analog-to-digital (A/D) conversion was carried out 1/10 cycle of the cycle T of the ultrasonic wave. When the echo is the SN ratio equal 0, the result calculated as that in which the echo waveform carried out time change is shown in Fig. 3-3. In Fig. 3-3, if time change of the echo becomes large, the improvement effect in the SN ratio of addition processing will decrease. Thereby, the scope of the improvement effect in the SN ratio by addition processing became clear. The case where it applied to an actual examination was considered. If the repetition cycles of transmission and reception of the ultrasonic wave were assumed to be 100 μsec, the total measurement time will be set to 0.01 sec. And if the maximum speed of SB tracer was assumed to be 50 mm/sec, time change of the echo signal will be set to about 0.4 μsec. Since the frequency of the ultrasonic wave to be used is 5MHz, time change of this echo signal is equivalent to 2T. Improvement in about 3 of the SN ratio is expectable from Fig. 3-3 with addition processing. Moreover, if the repetition cycle of transmission and reception of the ultrasonic wave is shortened, it will become possible to raise the SN ratio further.

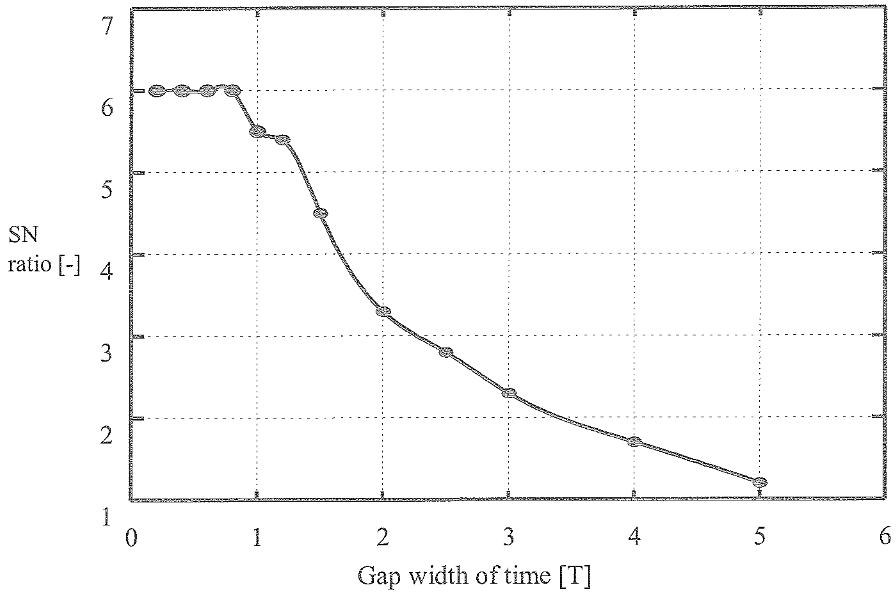

Fig.3-3 Relation between the improvement value in the SN ratio by addition processing, and the time fluctuation value of data

Furthermore, in order to strengthen the ultrasonic echo, the tracer of large size of 300-500 μm was developed. The echo intensity of the large size target that performed signal processing is shown in Fig. 3-4.

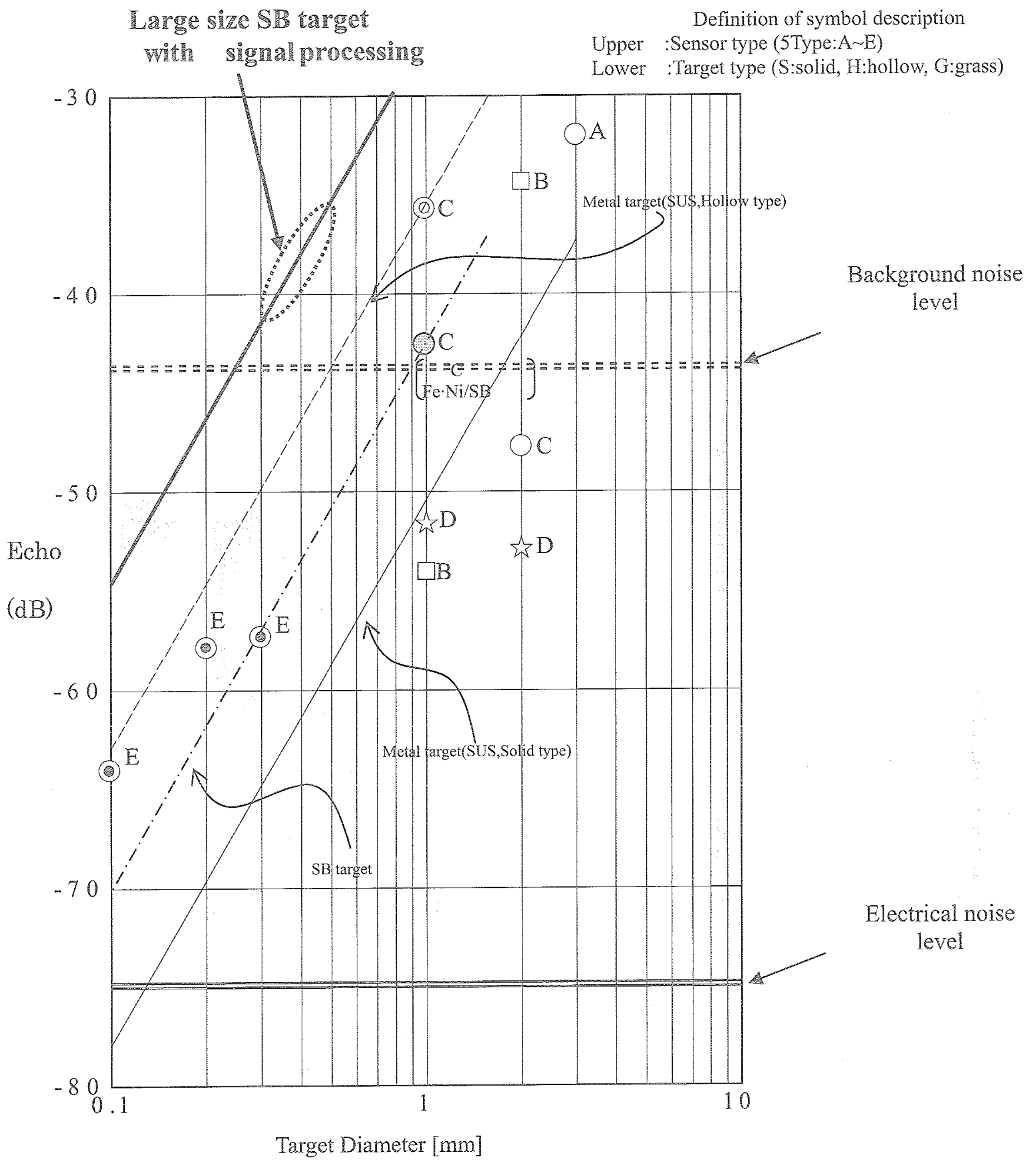

Normalized echo intensity := (echo level)/A/T
A (Sensor sensitivity) :Echo level of sensor head
T :1-R^2 (Transmittance of sound pressure at surface between medium and sensor head)
R(Reflectance of sensor head) :Echo level of surface between medium and sensor head /Echo level of sensor head

Fig.3-4 Prediction of echo intensity of SB

3.1.2 Development for 3D-UV Measuring Unit

Ongoing design of 3D-UV measuring unit is briefly described in this section. The conceptual diagram of a 3D-UV measurement unit is shown in Fig. 3-5. The 3×3 element transducer with a frequency of 10MHz, transmitting and receiving amplifier units are already make ending. This fiscal year made the A/D converter and the system controller.

The signal processing unit made in the Fig. 3-6 is shown. The A/D converter considers as eight channels corresponding to the multi-element transducer, a sampling bit is 12 bits, a sampling frequency is 100MHz, and a loading memory per channel is 64 M bytes. The system controller has the function to perform continuation extraction of measurement data, and transmission to the external personal computer of extraction data, and data transmission speed is 1 Gbit/sec (effective value: about 0.5 Gbit/sec) in a theoretical value. Equalization processing is processed at high speed by FPGA (Field Programmable Gate Array) on A/D converter boards. Data is transmitted and saved at PC. After subtraction processing, the image of the tracer corresponding to the flow pattern is created by synthetic aperture processing.

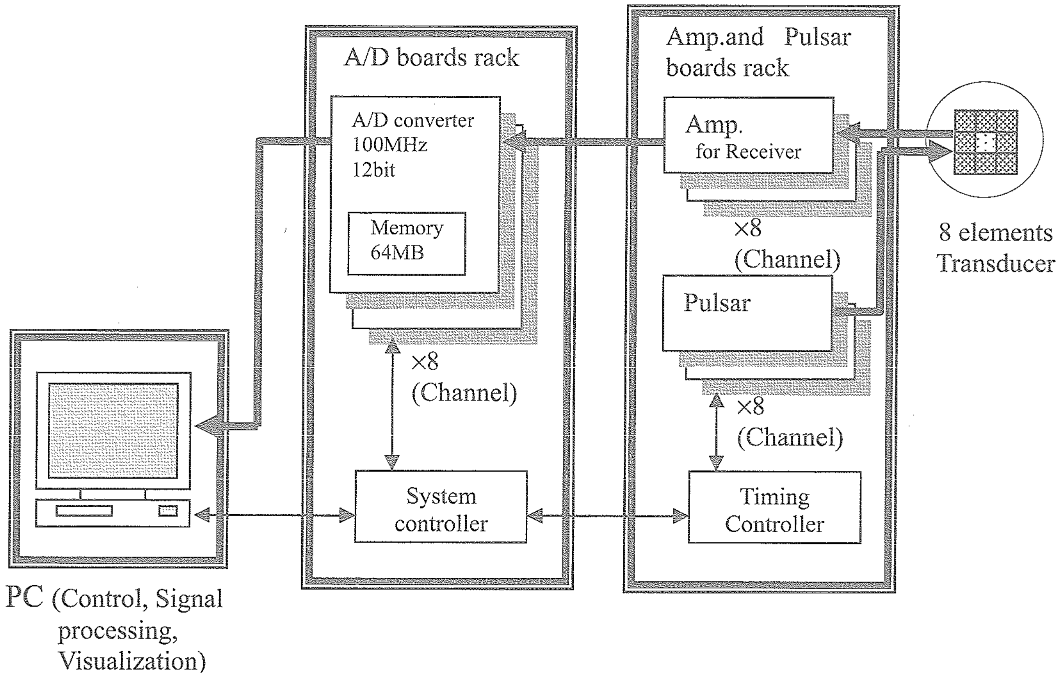

Fig.3-5 Signal processing unit diagram

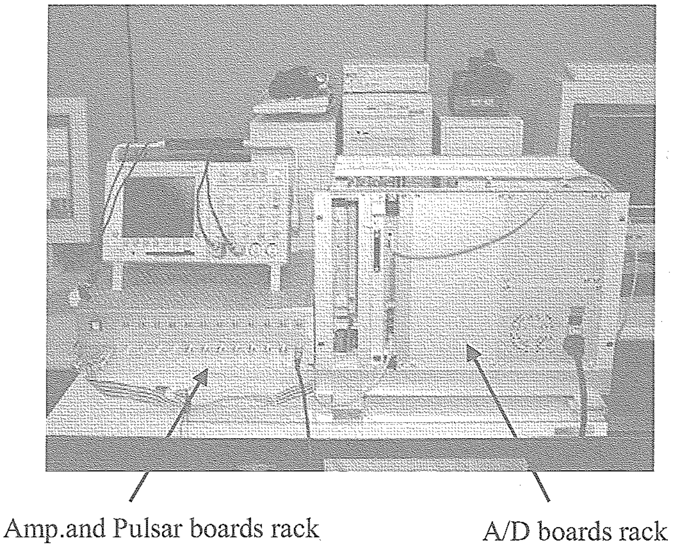

Fig.3-6 Photo. of signal processing unit

4. CONCLUSION

(1) The experimental study on thermocapillary convection of low Prandtl number fluid was carried out to understand transition behavior to oscillatory flow. The half-zone liquid bridge of molten tin was formed between hot and cold disks in high vacuum chamber (10^{-5} Pa). The three radiation thermometers were used to measure the free surface temperature at a different azimuthal location at the same time. In addition, the temperature distribution at interface between liquid bridge and cold disk was measured by using very fine thermocouples. In order to detect the transition point and to make clear the oscillation mode more precisely, the temperature measurement system was developed..

(2) It could be detected that the steady thermocapillary convection changes to oscillatory under certain condition. The observed phenomena of transition processes after the oscillatory onset were revealed by comparing to numerical result done by Imaishi *et al.*. The effect of aspect ratio (L/r) on critical Marangoni number was investigated. The critical Marangoni number decreases with increasing the aspect number. This behavior agrees with numerical simulation done by Imaishi *et al.* qualitatively except for region of smaller aspect ration.

(3) Since the echo signal from the tracer had the very small bad SN ratio, in order to raise the SN ratio, signal processing technique was examined. Consequently, the noise which originates in the shoe by the subtraction processing technique was removable. And the SN ratio could be improved by the addition processing by repetition measurement, and the SN ratio improved about 3 times by calculation supposing actual measurement. The A/D converter and the system controller were manufactured in the 3D-UV measurement unit.

References

[1] H. Kuhlmann, in: Hydrodynamic Instabilities in Thermocapillary Flows, Microgravity Science Technology VII/2 (1994) 75.

[2] N. Imaishi, S. Yasuhiro, T. Sato, and S. Yoda, in: Proc. 44th SPIE Annual Meeting and Exhibition, Materials Research in Low Gravity II, Denver, **3792** (1999) 344.

[3] N. Imaishi, S. Yasuhiro, and S. Yoda, in: Marangoni Convection Modeling Research Annual Report (NASDA-TMR-000006E), National Space Development Agency of Japan (2000) 157.

[4] S. Nakamura, T. Hibiya, K. Kakimoto, N. Imaishi, S. Nishizawa, A. Hirata, K. Mukai, S. Yoda, and T. Morita, J. Crystal Growth, **186** (1998) 85.

[5] T. Hibiya, S. Nakamura, N. Imaishi, K. Mukai, K. Onuma, P. Dold, A. Cröll, K-W. Benz, and S. Yoda, in: Proc. Joint 1st Pan-Pacific Basin Workshop and 4th Japan-China Workshop on Microgravity Sciences, Tokyo (1998) 8.

[6] J. Han, Z. Sun, L. Dai, J. Xie, and W. Hu, J. Crystal Growth, **169** (1996) 129.

[7] Y.K. Yang and S. Kou, J. Crystal Growth, **222** (2001) 135.

[8] R. Imai, K. Takagi, M. Ohtaka, F. Ohtsubo, H. Natsui, and S. Yoda, in: Marangoni Convection Modeling Research Annual Report (NASDA-TMR-990007E), National Space Development Agency of Japan (1999) 71.

[9] K. Takagi, M. Ohtaka, H. Natsui, T. Arai, and S. Yoda, in: Marangoni Convection Modeling Research Annual Report (NASDA-TMR-000006E), National Space Development Agency of Japan (2000) 115.

[10] K. Takagi, M. Otaka, H. Natsui, T. Arai, S. Yoda, Z. Yuan, K. Mukai, S. Yasuhiro, and N. Imaishi, J. Crystal Growth, **233** (2001) 399

[11] M. Ohtaka, K. Takagi, H. Natsui, T. Arai, and S. Yoda, in: Proc. 2nd Pan-Pacific Basin Workshop on Microgravity Sciences, Pasadena (2001) IF-1159.

[12] K. Takagi, M. Otaka, H. Natsui, T. Arai, and S. Yoda, J. Jpn. Soc. Microgravity Appl. (in Japanese), **18** (2001) 11.

[13] N. Imaishi, S. Yasuhiro, Y. Akiyama and S. Yoda, J. Crystal Growth, **230** (2001) 164

[14] Z.Yuan, K.Mukai, K.Takagi and M.Ohtaka, J.Jpn. Inst. Metals (in Japanese), **65** (2001) 21.

[15] A. Passerone, E.Ricci and R.Sangiorgi, J. Material Sci., **25** (1990) 4266

[16] R.Sangiorgi, C.Senillou and J.C.Joud, Surface Sci., **202** (1988) 509

[17] M. Ohtaka, K. Takagi, H. Natsui, T. Arai, and S. Yoda, in: Marangoni Convection Modeling Research Annual Report (NASDA-TMR-010015E), National Space Development Agency of Japan (2001) 145.

[18] M. Matsumoto, M. Ohtaka, H. Natsui, T. Arai, and S. Yoda, in: Marangoni Convection Modeling Research Annual Report (NASDA-TMR-020026E), National Space Development Agency of Japan (2002) 157.

[19] M. Matsumoto, H. Hayashida, A. Komiya, H. Natsui, T. Arai, and S. Yoda, in: Marangoni Convection Modeling Research Annual Report (NASDA-TMR-030004E), National Space Development Agency of Japan (2003) 159.

JAXA Research and Development Report
(JAXA-RR-04-027E)

Date of Issue : March 31, 2005

Edited and Published by :
Japan Aerospace Exploration Agency
7-44-1 Jindaiji-higashimachi, Chofu-shi,
Tokyo 182-8522 Japan

Printed by :
FUJIPLANS Co., Ltd.
3-8-2 Toukai, Ota-ku, Tokyo 143-0001 Japan

Printed on Recycled Paper

Japan Aerospace Exploration Agency